2020

LASER ABLATION IN LIQUID FOR THE CONTROLLED PRODUCTION OF PHOTOLUMINESCENT GRAPHENE QUANTUM DOTS AND UPCONVERTING NANOPARTICLES

Rosemary Lynn Calabro

University of Kentucky, rlcalabro@alumni.iu.edu

Author ORCID Identifier:

 https://orcid.org/0000-0001-9394-5385

Digital Object Identifier: https://doi.org/10.13023/etd.2020.218

Right click to open a feedback form in a new tab to let us know how this document benefits you.

LASER ABLATION IN LIQUID FOR THE CONTROLLED PRODUCTION OF
PHOTOLUMINESCENT GRAPHENE QUANTUM DOTS AND UPCONVERTING
NANOPARTICLES

_____

DISSERTATION
_____

A dissertation submitted in partial fulfillment of the
requirements for the degree of Doctor of Philosophy in the
College of Arts and Sciences
at the University of Kentucky

By

Rosemary Lynn Calabro

Lexington, Kentucky

Director: Dr. Doo Young Kim, Professor of Chemistry

Lexington, Kentucky

2020

ABSTRACT OF DISSERTATION

LASER ABLATION IN LIQUID FOR THE CONTROLLED PRODUCTION OF
PHOTOLUMINESCENT GRAPHENE QUANTUM DOTS AND UPCONVERTING
NANOPARTICLES

Photoluminescent (PL) nanomaterials play an important role in areas including displays, sensing, solar, photocatalysis, and bio applications. Traditional methods to prepare PL materials suffer many drawbacks such as harsh chemical precursors, complicated synthetic steps, and production of many byproducts. Laser ablation in liquid (LAL) has emerged as a promising alternative to prepare materials that is single-step, fast, uses fewer precursors, produces fewer side products, and has simple purification steps. During LAL, a solid target is irradiated with a pulsed laser source. The laser pulses cause plasma plumes of the target material to form which are cooled, condensed, and can react with the surrounding liquid. This dissertation explores LAL as an alternative method to produce two important classes of PL nanomaterials: graphene quantum dots (GQDs) and upconverting nanoparticles (UCNPs). GQDs are a class of carbon PL materials that are lightweight, biocompatible and can be produced from cheap and abundant carbon sources. Their PL properties depend on both radiative recombination of intrinsic states through their carbon backbone as well as defect like states from surface functionalization. LAL of carbon nano-onions in water was used to produce GQDs. These GQDs were systematically compared to those produced by a traditional chemical oxidation method and showed blue shifted emission, higher fractions of hydroxyl-groups, and smaller sizes. Nitrogen doping with controlled chemical composition allowed further tuning of the PL and was achieved by including dopant molecules in the liquid during LAL. Lifetime measurements showed three emissive pathways and provided greater understanding of the roles of intrinsic and defect like emissive states. UCNPs composed of $NaYF_4$:Yb^{3+}/Er^{3+} are interesting for many bio applications but are challenging to prepare with both high upconversion efficiency and water solubility. Control of the UCNP phase is important for high efficiency. LAL was used to address these issues by irradiating a target of desired phase in an aqueous solution containing capping agents which allowed for formation of water soluble UCNPs of the desired phase. Tuning of laser parameters allowed control of the size, composition, and PL of the UCNPs. This work showcases LAL as a method to efficiently produce PL nanomaterials with controlled properties.

Rosemary Lynn Calabro

05/07/2020

Date

LASER ABLATION IN LIQUID FOR THE CONTROLLED PRODUCTION OF
PHOTOLUMINESCENT GRAPHENE QUANTUM DOTS AND
UPCONVERTING NANOPARTICLES

By
Rosemary Lynn Calabro

Dr. Doo Young Kim
Director of Dissertation

Dr. Yinan Wei
Director of Graduate Studies

05/07/2020
Date

I especially want to offer my gratitude to my undergraduate research advisor, Dr. Lyudmilla Bronstein at Indiana University. Without the opportunities she gave me I would not be where I am today. She not only inspired my love for materials chemistry research, but she showed confidence in me when I was having a hard time finding a purpose and believing in myself.

I also wish to thank many of my friends and family for the supportive roles they played during my graduate studies. My husband, Vince Calabro, has been supportive of my goals to pursue a PhD since before I was even applying to graduate school. He has provided nothing but encouragement and understanding during this whole process. My parents Mary and Steve Easterday have always encouraged learning and a pursuit of higher education. I especially would not have been able to survive this process without my sister Frannie, or my friends Kayla and Madison who despite living far away have always been available to talk and offer moral support. And of course, I have to thank my sweet dog, Francium, for being a much-needed distraction and for providing a source of comfort during some of the more stressful periods of time.

TABLE OF CONTENTS

LIST OF TABLES

LIST OF FIGURES

xiii

CHAPTER 1. INTRODUCTION

1.1   Photoluminescence

Photoluminescence (PL) refers to the process that occurs when a material emits light after reaching an excited state through the absorbance of light.[1] This process is useful for a broad range of applications including but not limited to imaging[2-3], sensing[4-6], displays[7-8], photovoltaics[9-10], and catalysis[11-13]. Practical implementation of PL materials relies on both a fundamental understanding of their PL properties, as well as an ability to fine tune the absorbed and emitted wavelengths. Figure 1.1 shows a Jablonski diagram which illustrates the various photophysical processes a molecule or material can undergo. The first step is absorbance, which typically occurs in the ultraviolet or visible region of the electromagnetic spectra. This process is fast, occurring on a time scale of about 10^{-15} s.[14] When absorbance occurs, an electron is excited from the ground S_0 electronic state to a higher electronic state such as the S_1 or S_2 state. The absorbance process can be described by Beer's law (Equation 1.1) where A is absorbance, c is molar concentration, b is the pathlength of light, and ε is the molar absorptivity (typically units of L mole^{-1} cm^{-1})[15].

$$A = \varepsilon cb \hspace{4cm} \text{(Equation 1.1)}$$

The molar absorptivity is both unique to a particular molecule or material and is dependent on the oscillator strength of the transition at a particular wavelength. Once the electron has been promoted to an excited electronic state it must return to its ground state which can occur by both non-radiative and radiative processes. With vibrational relaxation the electron relaxes from a higher vibrational state to a lower energy vibrational state within the same electronic state. This process is fast, occurring on a time scale of about 10^{-14}–10^{-11} s.[16] Internal conversion can also occur and involves the non-radiative flow of energy from the excited state to a rovibrational level of another electronic state of the same electron

1

spin multiplicity. This is illustrated in Figure 1.1 showing the energy flowing from the S_2 state to the S_1 state. Internal conversion is also fast and occurs on a time scale similar to vibrational relaxation.[17] Intersystem crossing also involves the non-radiative flow of energy from the excited state to a rovibrational level of another electronic state, but in this case the two electronic states have a different spin multiplicity. This is illustrated in Figure 1.1 as the energy flows from the singlet S_1 state to the triplet T_1 state. Intersystem crossing is much slower and occurs on a time scale of about 10^{-8}–10^{-3} s.[14, 18] Finally, PL can occur. With PL, the electron relaxes from an excited electronic state back to the ground electronic state while also emitting a photon. PL is the general term that describes transitions occurring from any spin multiplicity. A more specific type of PL is fluorescence, which is the process that occurs when emission arises from a singlet-to-singlet transition. This is the most common type of PL and typically occurs on a time scale of 10^{-9}–10^{-7} s.[16] Another common PL process, phosphorescence, involves emission arising from a triplet to singlet transition. The phosphorescence process is spin forbidden and consequently has a longer time scale than fluorescence of about 10^{-4}–10^{-1} s.[19] The time scales of the individual processes have several consequences. First, the fast time scale of vibrational relaxation means it typically happens before PL can occur. This means that most molecules and materials lose energy before emission and a Stokes shift (red shift) in the emitted wavelength relative to the absorbed wavelength occurs.[14] Second, since both vibrational relaxation and internal conversion are significantly faster than fluorescence, most fluorescent molecules relax to the ground excited state (the lowest vibrational level of the S_1 state) before emission. This observation is described by Kasha's rule and a consequence is that the PL wavelength is the same regardless of the excitation wavelength used.[20] A corollary to Kasha's rule is Vavilov's rule which states the PL quantum yield (PLQY) is also independent of the excitation wavelength used.[14, 20] While these rules certainly hold true for many fluorescent molecules, there are many exceptions including graphene

quantum dots (GQDs) and upconverting nanoparticles (UCNPs) which will later be discussed in further detail.
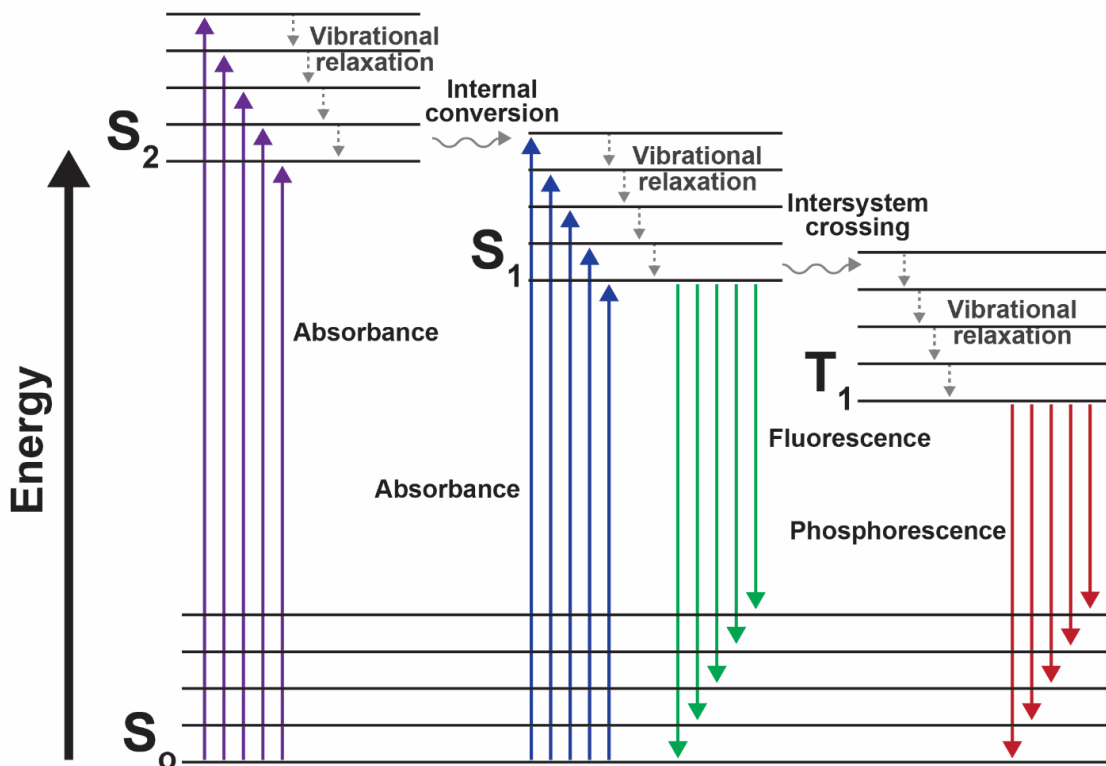
Figure 1.1 Jablonski diagram illustrating the radiative and non-radiative processes that occur when light is absorbed by matter.

Once the molecule is in the exited state, the various radiative and non-radiative processes follow first order decay behaviors where the rate depends on the rate constant of the particular process and the population of the excited state, $[S_1]$. Table 1.1 lists the various processes that depopulate the S_1 state and their associated rates where k_e is the rate of emission, k_{ic} is the rate of internal conversion, k_{isc} is the rate of intersystem crossing and k_c is the rate of any photochemical reactions that can occur.[16]

Table 1.1 Photoluminescence kinetic processes and their rates

Kinetic Process		Rate
Excitation/Absorbance	$S_0 + h\nu_a \rightarrow S_1$	I_a
Emission/Fluorescence	$S_1 \rightarrow h\nu_e + S_0$	$k_e[S_1] = I_e$
Internal conversion	$S_1 \rightarrow S_0$	$k_{ic}[S_1]$
Intersystem Crossing	$S_1 \rightarrow T_1$	$k_{isc}[S_1]$
Photochemistry	$S_1 \rightarrow products$	$k_c[S_1]$

The rates of all the non-radiative processes can be combined according to equation 1.2

$$k_{nr} = k_{ic} + k_{isc} + k_c \qquad \text{(Equation 1.2)}$$

In the case of a sharp pulsed excitation, $I_a = 0$ and the depopulation of S_1 is described according to equation 1.3.

$$\frac{d[S_1]}{dt} = -(k_e + k_{nr})[S_1] \qquad \text{(Equation 1.3)}$$

Since the lifetime, τ, of a state is defined as the time it takes to deplete the initial state by $\frac{1}{e}$, equation 3 can be solved to produce the following:

$$\tau = \frac{1}{k_e + knr} \qquad \text{(Equation 1.4)}$$

This equation shows that the lifetime of a state is dependent on both the rate of emission and the rate of non-radiative deactivation. Finally, if one considers the steady

state, where the population of S$_1$ does not change, the rate equation can be described by equation 1.5.

$$\frac{d[S_1]}{dt} = I_a - k_e[S_1] - k_{nr}[S_1] = 0$$ (Equation 1.5)

PLQY, Φ, can then be defined by equation 1.6.

$$\Phi = \frac{I_e}{I_a} = \frac{k_e}{k_e + k_{nr}}$$ (Equation 1.6)

In practice, PL lifetime can be measured by time correlated single photon counting (TCSPC). This method uses a pulsed, laser excitation source, with a repetition rate that is slow enough to allow complete decay between excitations. PLQY can be measured by either an absolute method, using an integrating sphere, or by a relative method using a standard with a known PLQY. An understanding of the PL wavelengths, lifetime, and PLQY allows for better design and implementation of PL materials into the desired applications.

In the case of nanomaterials, the PL properties are influenced by several factors. One important phenomenon is the quantum confinement effect (Figure 1.2). In a semiconducting material, when the material switches from bulk to nanoscale in size and approaches or becomes smaller than the Bohr-exciton radius of the material, the energy levels become discrete, and the separation between the valence and conduction band is termed the bandgap.[21] The energy gap can be described similarly to a particle in a box, where smaller particles have a larger energy gap and bluer PL and as the size of the nanoparticle increases, the band gap decreases and the PL is shifted towards the red.[22] This phenomenon allows for tuning on the PL simply by tuning the particle size. The surface environment is also an important factor when considering the PL properties. The presence of electron-donating groups or electron-withdrawing groups can shift energy levels and

affect PL wavelengths.[16] Nanomaterials have a higher surface-to-volume ratio than their bulk counterparts which can make them more susceptible to quenching by solvent molecules.[23] This quenching can be prevented by surface passivation through capping by either ligands or inorganic shells.[24-26] Surface states originating from functional groups, defects, or emissive capping agents can result in multiple emissive pathways.[27-29] Lastly, ensemble PL broadening can occur due to inhomogeneity within a sample.[30-31]
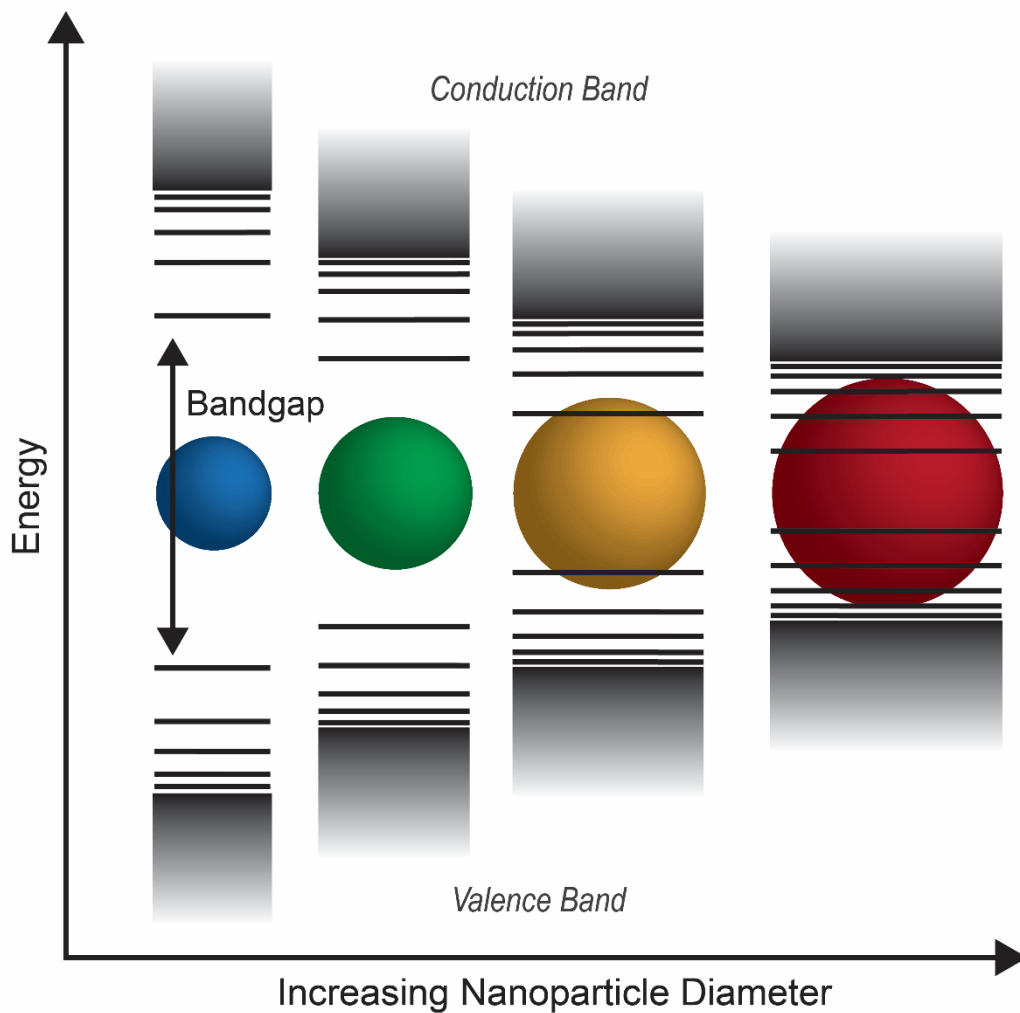
Figure 1.2 Quantum confinement effect and its influence on bandgap of nanoparticles

1.2   Graphene quantum dots

Graphene quantum dots have emerged as a promising class of photoluminescent nanomaterials due to their versatile applications and interesting optical properties. GQDs can be synthesized from cheap and abundant carbon sources in a large scale, avoid the use of heavy metals, and are light weight as well as biocompatible. [32-33] They also have a high charge carrier mobility, large surface area to mass ratio, and their properties can be tuned by controlling the functional groups present on the surface.[34-35] One of the main attractive features of GQDs it their PL properties. They typically have strong absorbance bands in the ultraviolet and visible regions and exhibit PL ranging from deep ultraviolet (UV) to near-infrared (NIR).[36-38] Figure 1.3 shows a scheme of a GQD with oxygen and nitrogen functional groups. A typical GQD has regions of sp^2 hybridized carbon as well as surface defects and functional groups. The chemical surface environment is highly dependent on the methods used to produce the GQDs. Defects that disrupt the sp^2 domains such as substitutional dopants, vacancies, or regions of sp^3 carbon can also exist and the functional groups can be tuned based on the desired applications and GQD properties.
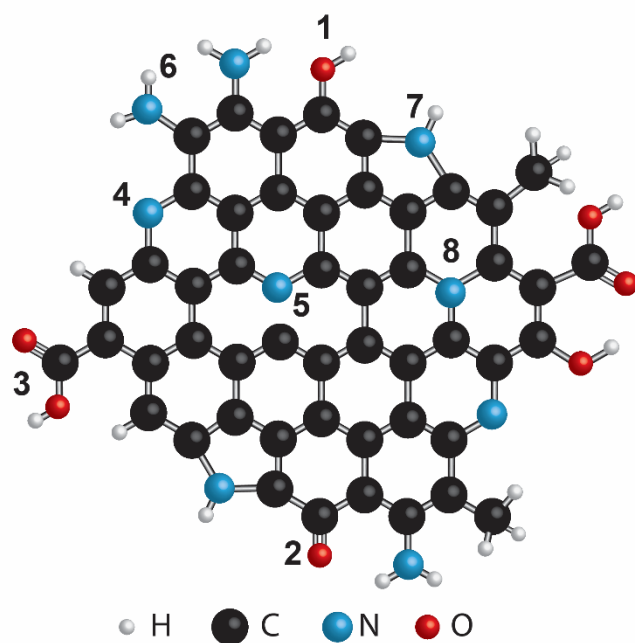
1. Hydroxyl   4. Pyridinic (edge)   7. Pyrrolic

2. Carbonyl   5. Pyridinic (center)   8. Graphitic N

3. Carboxylic   6. Amine

Figure 1.3 Schematic representation of a graphene quantum dot with oxygen and nitrogen functional groups. Adapted with permission from reference 39 with permission from the American Chemical Society.

1.2.1 Synthetic approaches

GQDs have been synthesized by a variety of methods but can be categorized into two distinct approaches: top down and bottom up. With the top down method, a large graphitic precursor is somehow cut into smaller nanoscaled fragments. Typical precursors include graphene sheets, graphene flakes, carbon black, carbon nanotubes, graphene oxide, and carbon nanoonions.[32, 40-41] The top-down approach offers the advantage of maintaining large graphitic domains in the final product. This approach also has potential for large scalability.[32] The cutting process can be accomplished through a variety of approaches.

The chemical oxidation method (also termed the modified Hummer's method) uses concentrated acids such as nitric and sulfuric acid to cut the precursor into fragments. The nitric acid oxidizes the bulk carbon precursor while the sulfuric acid acts as an intercalating agent that separates the graphene sheets.[42-43] One major drawback to this method is the use of harsh acids which can form side products, requires a neutralization step, and produces large quantities of hazardous waste. The chemical oxidation method also requires dialysis as a purification step which is time consuming and can contribute to low yields of the final product. Other top down approaches include hydrothermal cutting[44-45], electrochemical cutting[46], and nanolithography[47]. However, these strategies also suffer low production yields, limited control over the product sizes, and non-uniform size distributions. The bottom up approach, on the other hand, uses small molecular precursors to build larger particles. This can be done through several methods including stepwise organic synthesis[40], solvothermal synthesis, microwave pyrolysis[48], electrochemical methods[49-50], and chemical vapor deposition[51-52]. The products produced by the bottom up method are often more disordered and have smaller graphitic domains, and they are often termed carbon nanodots (CNDs) to distinguish them from GQDs. One major advantage to the bottom up approach is the direct inclusion of heteroatoms such as nitrogen during synthesis, unlike the top down approach which typically requires a further step to modify the functional groups that are present.[53] The stepwise organic synthesis approach allows optimal control over the size and structure, and while CNDs produced through this method have provided valuable information into the PL properties, it is time consuming, requires expensive precursors, and is not practical for large scale up.[32, 47] The solvothermal method has been widely studied and uses a steel reactor in a Teflon container to heat precursors under high temperature and pressures. This strategy is fairly simple and can allow for heteroatom doping by including precursors that contain nitrogen or other desired dopants. However, size control is challenging, and production of fluorescent byproducts is a main concern. A recent work by Essner et al. systematically studied the various products from a

9

solvothermal synthesis method and found that small molecular side products were the main source of PL rather than the CNDs.[54] The extensive variety of approaches to synthesize GQDs and CNDs results in a broad range of sizes and chemical states, and their properties are highly dependent on the methods used to produce them. This makes comparisons of samples prepared by different researchers and by different methods challenging and important to consider.

1.2.2 Emission properties

The PL properties of GQDs are quite different from molecular fluorophores. First, one commonly observed feature is excitation dependent emission which is in violation of Kasha's rule.[55-56] Another characteristic feature is a large Stokes shift[57], and often GQDs will have a mix of PL peaks that are excitation independent and excitation dependent. The emission peaks also tend to be quite broad.[58] One major contribution to the optical properties is an intrinsic bandgap due to the presence of sp^2 hybridized nanodomains.[36] This allows for size dependent absorbance and emission through the quantum confinement effect. The size of the sp^2 domains controls the bandgap with larger domains having a red shifted emission and smaller sp^2 domains having blue shifted emission. One important point to note is that the size of the GQD does not necessarily reflect the size of the sp^2 domain. Disorder within a carbon dot can lead to smaller sp^2 domains within the particle and a mixture of different sp^2 domain sizes can contribute to the excitation dependent emission.[59]

However, size effects are not the only factors that influence the PL of GQDs. Both top-down and bottom-up synthetic strategies tend to introduce defects and functional groups on the GQD surface. Surface defect states including sp^3 bonded carbon or surface functional groups result in localized electronic states that can have their own PL properties.[36, 53, 60] These are termed extrinsic emissions or molecule-like emissions. The

type of functional group has a strong influence on the PL wavelengths and lifetimes observed. For instance, more oxidized groups such as carboxylic groups tend to have redder emission with longer PL lifetimes while reduced groups such as hydroxyl groups tend to have bluer emission with faster PL lifetimes.[14] Nitrogen doping has been shown to improve the PLQY and reports have shown both blue shifted and red shifted emission depending on the chemical state. Additionally, surface passivation can also improve the PL properties by protecting the functional groups from solvent quenching effects. In most GQDs, the PL is a mixture of both intrinsic and extrinsic emission with the intrinsic states generally having faster lifetimes and weaker PL and the extrinsic states having slower lifetimes and brighter PL.[36, 61]

Some theoretical studies offer valuable information on understanding the large Stokes shift and broadening. Density functional theory (DFT) has been applied to several types of GQDs including pristine and ones that also contain heteroatoms.[41, 60, 62] One study showed that the strongest absorbance transitions arise from $S_4 \leftarrow S_1$ and $S_3 \leftarrow S_1$ transitions while the $S_2 \leftarrow S_1$ and $S_1 \leftarrow S_0$ transitions have much weaker oscillator strengths.[63] However, the emission from $S_2 \rightarrow S_0$ and $S_1 \rightarrow S_0$ transitions was much stronger than $S_4 \rightarrow S_1$ and $S_3 \rightarrow S_1$ transitions. This implies that internal conversion is much faster than PL which contributes to the large observed Stokes shift. Other studies investigated the effects that functional groups have on the optical properties. Functional groups can influence the PL by introducing molecule like components as well as through distortions of the geometry of the sp^2 domains thus introducing mid-gap states.[41] Edge functionalization can also impact the positions of the highest occupied molecular orbital (HOMO), and lowest unoccupied molecular orbital (LUMO) which affects the HOMO-LUMO gap. Generally, electron donating groups tended to increase the HOMO energy while electron withdrawing groups tended to lower the LUMO energy.[64] The impact of nitrogen functional groups was shown to be dependent on the chemical state, with graphitic nitrogen inducing a red shift, while other types of nitrogen did not have influence on the band gap.[62]

The broad PL peaks can be explained by ensemble broadening due to inhomogeneity in the individual particles.[57] Several single-molecule fluorescence studies have shown how the PL of individual particles deviates from the ensemble.[31, 65-66] One study showed that within a single sample a mix of particles showing single or multiple intensity levels of fluorescence were present. The samples were determined to have multiple energy levels due to multiple chromophoric units.[31] Another study showed through single molecule spectra measurements that individual particles can have excitation dependent emission, supporting the theory of a presence of multiple photoactive species within an individual particle. Other studies have shown that GQDs can have a triplet state.[57, 67] Generally, the PL behavior of GQDs is highly dependent on the sample preparation method, size, and functional groups present. However, these versatile and unique optical properties allow them to be viable in such a wide range of applications

1.2.3   Applications

The PL properties of GQDs make them excellent candidates for applications in displays and light emitting diodes (LED). For instance, in one report the synthesis of highly crystalline GQDs and separation based on size resulted in excitation independent PL that was dominated by the quantum confinement effect. This resulted in GQDs with PL that ranged from orange-red to blue based on size.[68] This color tunability is highly desirable for display applications. The electroluminescence of GQDs was studied by doping GQDs in various host materials and showed promise for LED applications with advantages over inorganic quantum dots because they were lightweight, non-toxic, and inexpensive to prepare.[69-70] GQDs have also been used in phosphor based LEDs to convert the high energy emission of a UV or blue LED to white light. Figure 1.4a shows an example of GQDs that have been made into a uniform film and then used to coat a blue emitting InGaN LED. Since the GQDs could strongly absorb in the blue region and had many different PL

wavelengths covering much of the visible spectrum, they converted the blue PL from the InGaN LED to white light.[8]
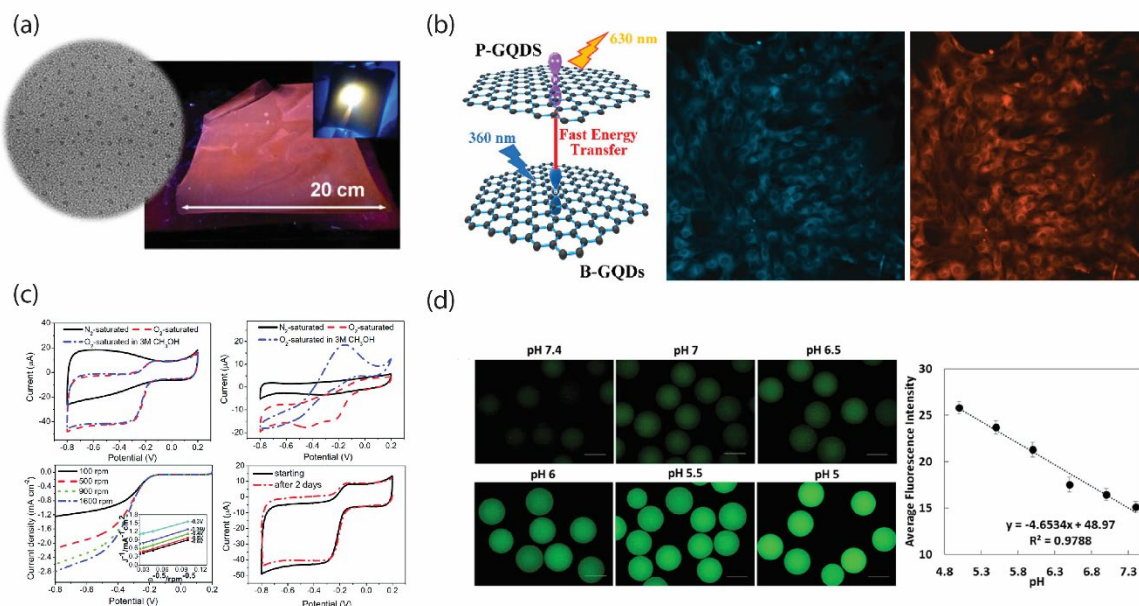
Figure 1.4 Examples of GQDs being used for applications in phosphor based LEDs (a)[8], cell imaging (b)[71], electrocatalysis (c)[49] and pH sensing (d).[72] Reprinted from references 8, 71, 49, and 72 with permission from the American Chemical Society.

The low cytotoxicity and high biocompatibility of GQDs make them promising for bioimaging applications.[33, 48, 71, 73] Figure 1.4b shows an example of cells that were incubated with B-doped and P-doped GQDs.[71] The cells with only B-doped GQDs emitted strong blue PL with 360 nm excitation. Cells with both B- and P-doped GQDs had a fast energy transfer from the B-doped to the P-doped GQDs which resulted in orange PL. Cell viability studies showed minimal cell death even with high GQD concentrations.[71] Another study assessed N-doped GQDs with adjustable amount of surface charge.[73] The results showed how the surface of the GQDs environment had influence on their uptake into the cells and demonstrated that N-GQDs can be used for both in vivo and in vitro applications. The tunability of the GQD surface environment with simple synthetic adjustments can allow them to be designed for imaging of targeted areas such as tumor cells.[74]

GQDs can also act as excellent photocatalysts for several reactions with important energy and environmental applications.[13] For example, N-doped GQDs have been used to catalyze the oxygen reduction reaction, an important reaction for fuel cell applications (Figure 1.4c). They are both cheaper than traditional platinum-based catalysts and are also resilient to methanol poisoning. The GQDs showed selectivity towards the 4-electron process with low overpotentials. [49] GQDs are also promising for CO_2 reduction and tuning of the GQD functional groups can control the selectivity to favor formation of either multi-carbon products or single carbon products.[75] GQDs have also been used as sensitizers for photocatalytic water splitting for H_2 generation.[13]

GQDs can act as fluorescence based sensors for a wide variety of systems either by PL quenching, enhancement, or wavelength shifts.[6, 47] Figure 1.4d. shows how microgels containing GQDs showed an increase in PL intensity as the pH of the system decreased.[72] Aerogels functionalized with GQDs showed both a decrease in PL intensity and a shift to a longer wavelength in the presence of NO_2 and also showed high selectivity toward NO_2 detection when compared to other common gasses that exist in the atmosphere.[76] Fluorescence quenching of GQDs has been shown as a promising method for chemical sensing of metal ions such as Hg^{2+}, Cu^{2+}, Cd^{2+}, Fe^{3+}, and Pb^{2+}, [47, 58 77] and for biosensing of molecules such as nucleic acids.[58] or curcumin.[78] In addition to the applications described previously, GQDs are also promising as surfactants,[79] for photodynamic therapy,[80] for drug delivery,[33] and in solar applications.[81]

1.3   Upconverting nanoparticles

1.3.1   Upconversion mechanisms

Upconversion is a nonlinear PL process that involves the absorption of multiple low energy photons and emission of a higher energy photon. This process can occur through several mechanisms including excited state absorption (ETA), energy transfer

upconversion (ETU), photon avalanche, cooperative energy pooling (CEP), and triplet-triplet annihilation (TTA) as presented in Figure 1.5. ESA is the simplest type of upconversion and involves a single activator ion (absorbing species).[82] During ESA, two successive photons are absorbed, and the activator is excited from the ground state to an intermediate state and then is excited again to the emitting state. (This is different from two photon absorption which requires absorption of two simultaneous photons.[83]) One advantage of ESA is that it is the only upconversion process that occurs with low dopant concentrations; however, it suffers the challenge of competing with non-radiative processes that depopulate the intermediate state.[23] It also often requires multiple excitation sources due to differences in energy gaps in the intermediate ← ground and the emitting ← intermediate transitions. ETU, on the other hand is, easier to achieve than the excited state absorption. During ETU a photosensitizer absorbs low-energy photons and through a Förster resonance energy transfer (FRET) donor-acceptor interaction transfers its energy to a nearby activator. This process continues multiple times until the activator eventually emits a high-energy photon.[84] The ETU process depends on the lifetimes of both the donor and acceptor, the distance between the donor and acceptor and their spectral overlap.[23] The most common ETU systems involves trivalent lanthanides embedded in a crystal because they have long lived excited states with many overlapping transitions and the concentrations of photoactive species can be tuned to optimize the upconversion efficiency. Photon avalanche, on the other hand, relies on achieving excited state population above a certain threshold.[85] First, weak non-resonant absorption occurs to promote the system from the ground state to an intermediate state. This is followed by a strong resonant excited state absorption which promotes the ion to an even higher energy level. Cross-relaxation can then happen as the excited ion interacts with a neighboring ground-state species, resulting in both ions occupying the intermediate state. This process continues and causes a substantial population of the intermediate[86], which is readily excited to the higher, photoluminescent state, allowing for high intensity emission.[87] The ability of

the intermediate state to achieve high levels of population makes the photon avalanche mechanism promising for the development of new lasing material.[88]

Upconversion systems based on the CET transfer mechanism involve two donor sensitizers that are coupled to an acceptor.[86, 89] The donors absorb low energy photons and then transfer their energy to the acceptor. Similar to two photon absorption, the intermediate state is a virtual state[90], however the two donors can act as a photon storage system which relaxes the temporal and spatial constraints of two photon absorption and allows higher upconversion efficiency.[89] Typical CET systems involve organic molecules for both the donors and acceptor.[89-90] Systems based on this mechanism are useful for applications that could be damaged by the high intensity excitations needed for two photon absorption. TTA based systems also typically use organic molecules, however in their case the photosensitizer intersystem crosses to enter a longer-lived triplet state. This is followed by triplet-triplet energy transfer (TTET) from the photosensitizer to an annihilator molecule. Two excited annihilator molecules then combine to promote one to a higher energy state while the other returns to the ground state (termed the TTA step), followed by upconversion PL from the excited state annihilator.[91-93] TTA has the advantage that it does not require the use of a coherent light source, and is promising for applications including solar,[92-93] drug delivery, and phototriggering.[91, 94] While all of the various upconversion mechanisms have their own advantages and potential applications, the remainder of this work is concerned with lanthanide based systems that undergo the ETU mechanism.
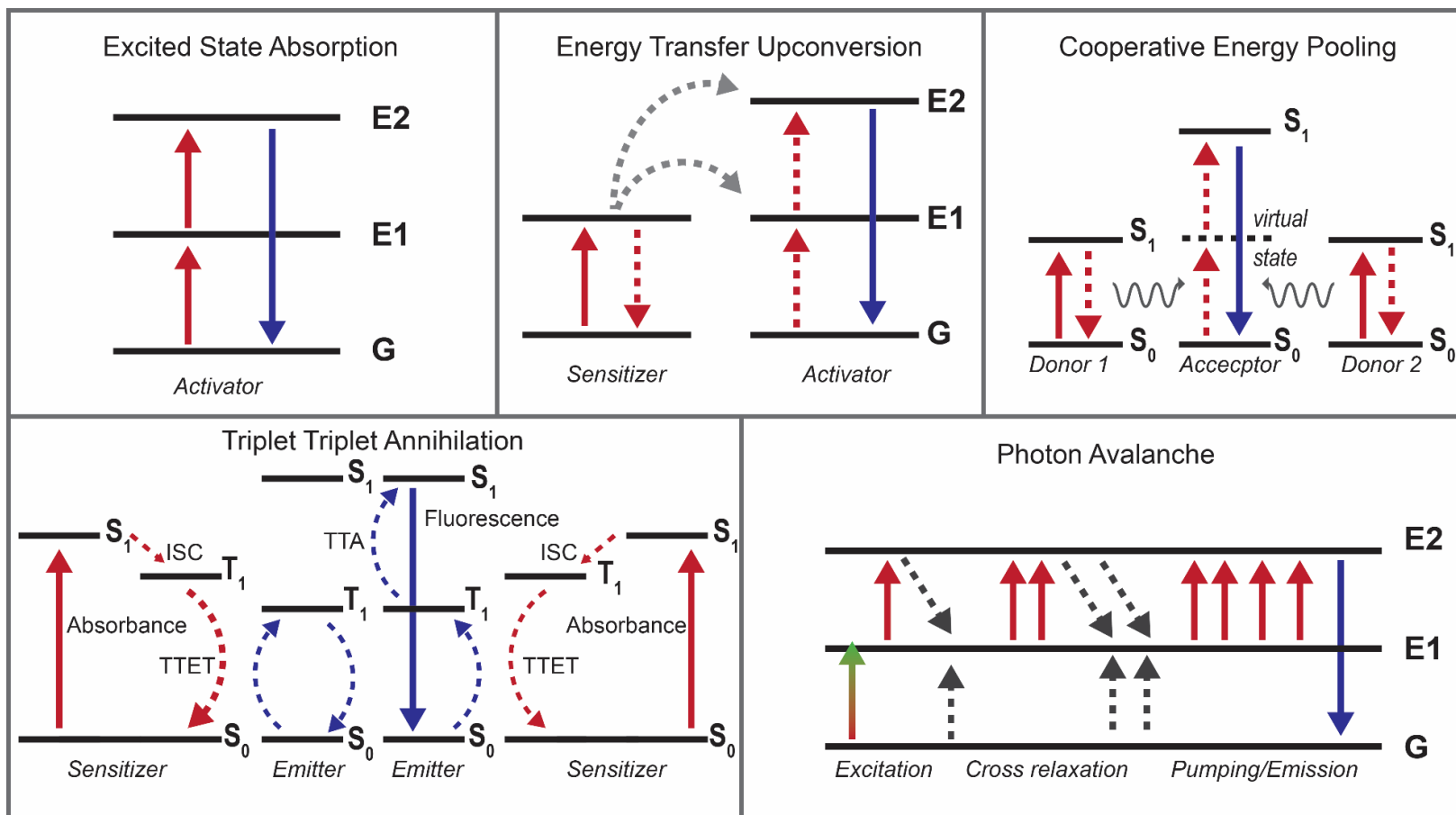
Figure 1.5 Energy level diagrams of the various upconversion mechanisms

1.3.2 The NaYF4:Yb/Er system

One of the most commonly studied ETU systems consists of a $NaYF_4$ host lattice that is doped with various lanthanide ions, often Yb^{3+}, Er^{3+}, and Tm^{3+}. Lanthanides typically exist in the trivalent (Ln^{3+}) oxidation state and have many luminescent electronic transitions, typically ranging from the visible to infrared region as shown in Figure 1.6. Many lanthanide ions, such as Nd^{3+}, Dy^{3+}, Ho^{3+}, Er^{3+}, and Tm^{3+}, have long lived excited electronic states which allows multiple energy transfers to occur before emitting, which makes them desirable activators for ETU.[95] Yb^{3+}, on the other hand, has a single, strong transition that occurs at 980 nm. This transition has good energy matching with many of the upconverting ions including Er^{3+} and Tm^{3+}, which makes an ideal NIR absorbing sensitizer.[95] Upconverting nanoparticles (UCNPs) composed of $NaYF_4$ and Yb^{3+} and Er^{3+} ($NaYF_4$:Yb/Er) have strong emissions in the green and red and UCNPs doped with Tm^{3+} as the activator ($NaYF_4$:Yb/Tm) have strong UV and blue emissions. The PL from these systems is due to atomic f-transitions. Therefore, the emission wavelengths are not affected by the surrounding environment or the UCNP size.[82, 96] This allows the UCNPs to be designed with a size and surface environment that is ideal for the desired application, without affecting the PL wavelengths. $NaYF_4$ is an ideal host because it is optically transparent in the wavelength regions of interest,[97] and Yb^{3+} has a similar ionic radius to the Ln^{3+} series, allowing substitutional doping by the Ln^{3+} ions with minimal distortions of the crystal structure.[98] $NaYF_4$ also has a low phonon energy, which helps minimize non-radiative relaxations of the photoactive species,[82, 99] and it is more stable that chlorides or bromides.[100] Several important factors affect the upconversion efficiency: The phase of the material, the doping ratios, and the size of the upconverter.
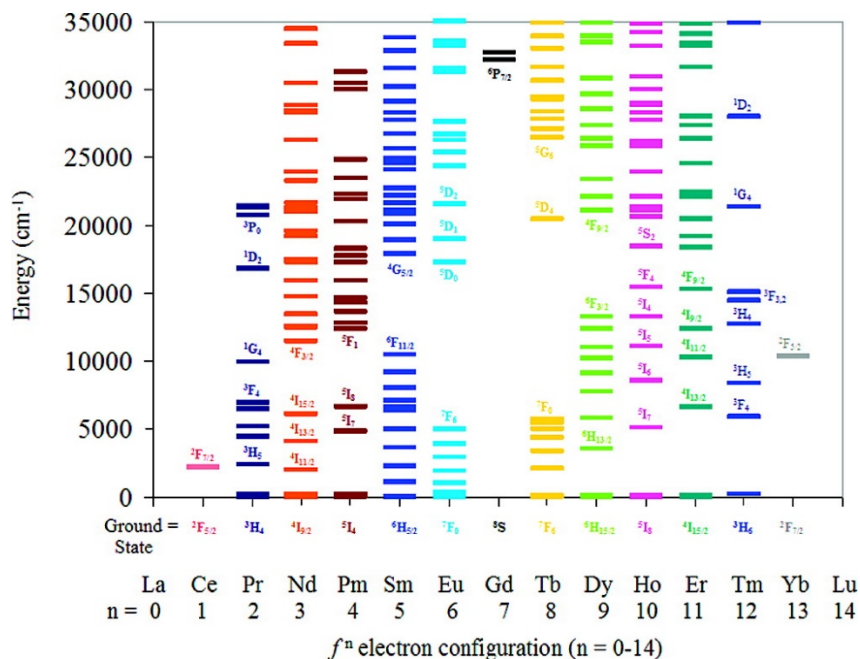
Figure 1.6 Electronic energy levels for the Ln^{3+} series. Reprinted from reference 97 with permission from the American Chemical Society.
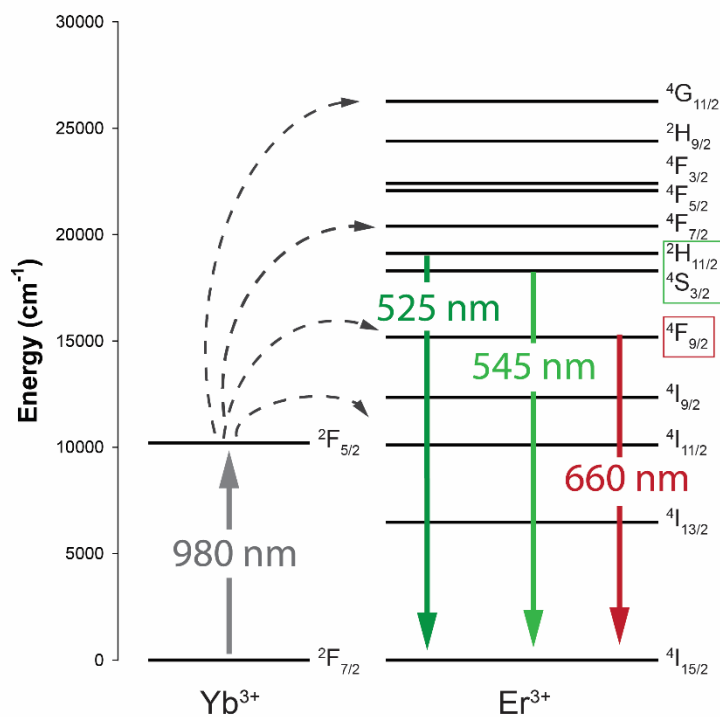
Figure 1.7 Upconversion absorbance and emission transitions for the $NaYF_4$:Yb/Er system

NaYF$_4$ can exist in both a cubic- (α-) and a hexagonal- (β-) phase. In general, the β-phase allows for a higher upconversion efficiency due to the lower site symmetry and shorter distance between lanthanide neighbors.[101-102] Upconversion efficiency of the α-phase can be improved by surface passivation or addition of plasmonic shells,[103-104] however, the β-phase generally is still the preferred phase for most applications. The β-phase is more challenging to synthesize and often requires high temperatures to achieve the desired crystallinity.[100] One strategy that has been used to improve the crystallinity is annealing of the UCNPs following synthesis,[105-106] however, this strategy also often leads to particle agglomeration.[107-108] Figure 1.7 presents the energy levels and main absorbance and emission transitions for a NaYF$_4$:Yb/Er upconversion system. First, Yb^{3+} absorbs 980 nm light and undergoes a transition from the $^2F_{7/2}$ ground state to the $^2F_{5/2}$ excited state. Once Yb^{3+} is in the excited state, it either returns to the ground state, undergoes energy migration to another nearby Yb^{3+} ion, or transfers its energy to Er^{3+} through a FRET based dipole-dipole coupling.[109-110] This energy transfer to Er^{3+} must occur multiple times prior to emission for upconversion to be observed. Typically, the absorbing Yb^{3+} is not a nearest neighbor to Er^{3+}, and energy migration from the absorbing Yb^{3+} to one neighboring Er^{3+} occurs prior to the energy transfer process.[109] For this reason, typical UCNPs have a much higher ratio of the photosensitizer Yb^{3+} than the activator Er^{3+} or Tm^{3+} because this allows for many nearby photosensitizers to be available to transfer energy to the activator. A typical NaYF$_4$:Yb/Er UCNP has 20% Yb^{3+} and 2% Er^{3+},[82, 92] and a NaYF$_4$:Yb/Tm UCNP typically contains 20-30% Yb^{3+} and 0.2% Tm^{3+}.[100] The strongest emission bands for Er^{3+} originate from the $^2H_{11/2}$ (525 nm), $^4S_{3/2}$ (545), and $^4F_{9/2}$ (660 nm) energy levels. It is widely accepted that the green emissions are mostly a 2-photon process, however the red emission process is not as well understood.[109] Some groups have proposed that the $^4F_{9/2}$ energy level is populated through a multiphonon relaxation process from the green $^2H_{11/2}$ and $^4S_{3/2}$ energy levels, however Berry et al. reported studies that suggest that the red emissive state

is populated through back energy transfer to Yb^{3+} from much higher ^4G or ^2K states. This mechanism would require a 3-photon process for red emission.[109, 111]

The emission processes are in competition with several quenching mechanisms that can contribute to a lower upconversion efficiency. This is most notably observed when the particles are nanoscaled in sized as they experience quenching effects much higher than their bulk counterpart. One possible source of non-radiative deactivation is multiphonon relaxation where the excited lanthanide ion loses its energy by exciting lattice vibrations.[112] Another possibility is energy migration or cross relaxation of Er^{3+}. However, due to the low oscillator strengths of these electronic transitions, the dipole-dipole coupling is weak and only occurs on a range of about 1 Å to 1 nm so it is only observed at high doping concentrations of Er^{3+}.[110] A much more probable energy loss process involves coupling of the excited state lanthanides to high energy vibrations of surrounding solvent molecules. Since the vibrations tend to have much stronger oscillator strengths these dipole-dipole couplings they can occur on a longer range of 1-10 nm. The C-H stretch around 3000 cm^{-1} the is present in many organic solvents has close energy matching with several Er^{3+} transitions[110], and overtones of the O-H stretch observed in water has a strong oscillator strength and broad overlap with the 980 nm transition of Yb^{3+} and can quench its $^2F_{5/2}$ state.[113] Since these quenching interactions are long range and UCNPs have a higher surface-to-volume ratio relative to the bulk, even core Yb^{3+}/Er^{3+} ions can be susceptible to solvent quenching depending on the UCNP size. For this reason, surface passivation through inert shells has been explored to protect the photoactive ions from solvent effects.[96, 103, 110, 113]

1.3.3 Applications

The spectral properties of UCNPs make them highly desirable for a wide variety of applications, especially biological. The 980 nm excitation wavelength used in the

NaYF$_4$:Yb/Er and NaYF$_4$:Yb/Tm based systems falls within the 650-1350 nm widow of optical transparency for biological tissues[99, 114-115] allowing better penetration depths than ultraviolet and visible wavelengths used for traditional fluorophores and quantum dots. Additionally, the long excitation wavelength used to excite UCNPs causes less damage to cells than shorter-wavelengths required to excite traditional fluorophores.[116-118] Unlike two-photon absorption, which requires a pulsed femtosecond-based laser to achieve simultaneous absorption of multiple photons[82], UCNPs can be excited with a continuous wave laser which is much simpler to operate and uses a lower power. This is because the UCNPs follow the energy transfer upconversion mechanism which does not require simultaneous absorption of two photons. The NIR excitation also allows for low autofluorescence[116, 119] and UCNPs show no photoblinking or photobleaching unlike metal-based quantum dots.[120] Since the emission bands are based on atomic transitions of the activator ions, the UCNP PL wavelengths are not affected by size effects or by the surrounding environment, which allows them to be designed in the ideal size range for the desired application. This also allows tuning of the surface environment without changing the emission wavelengths. Figure 1.8 shows four literature examples of UCNPs being used for photodynamic therapy (a), optical force sensing (b), security printing (c) and multimodal imaging (d).
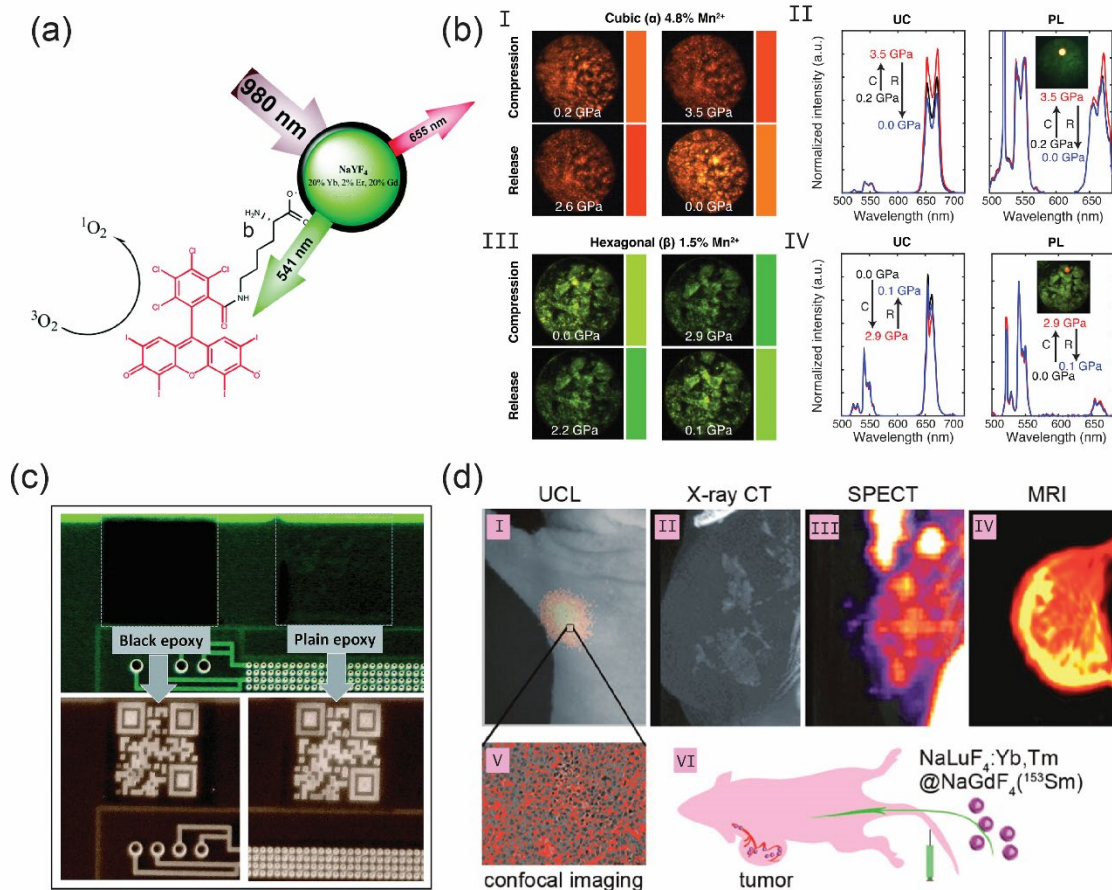
Figure 1.8 UCNPs used for PDT (a)[121], optical force sensing (b)[122], for security printing of QR codes (c)[123] and for multi-modal imaging applications (d)[124]. Adapted from references 121 and 123 with permission from the Royal Society of Chemistry and references 122 and 124 with permission from the American Chemical Society.

One widely studied application of UCNPs is targeted drug delivery. Attachment of drug molecules to UCNPs via photoreactive linker molecules allows for localized release of the drug. The UNCP is excited with a focused excitation source and its emitted visible-wavelength photons cause the linker to release the drug only in the areas where the UCNPs were exposed to the excitation source.[125-126] One subset of targeted drug delivery is photodynamic therapy (PDT). During PDT, a photosensitizer is used to generate either reactive oxygen species (ROS) or singlet oxygen.[127] Both ROS and singlet oxygen can react with and destroy neighboring cells, tissues, and other molecules. Unlike other drug

therapies that are not localized, PDT can be applied to a targeted area. While PDT is currently used in practice, it most commonly used in skin cancer treatment because the excitations can only penetrate small distances since most sensitizers are excited with visible or ultraviolet wavelengths.[121] However, researchers have successfully coupled photosensitizers to UCNPs and through a FRET energy transfer process, they use the upconversion PL to excite the photosensitizer which then generates singlet oxygen. The distance between the UCNP and photosensitizer and the size of UCNP has considerable influence on the FRET efficiency.[121, 128] These results are promising towards expanding PDT applications to areas that require longer penetration depths for excitation.

UCNPs have also been used for sensing applications. For instance, doping with Mn^{2+} causes the UCNP ratios of green and red emission to be sensitive to micro-Newton forces with a wide dynamic range (Figure 1.8b).[122] UCNPs can also be tethered to and used to excite fluorescence based sensors for sensing of metal ions.[4] This is important for detecting the presence of harmful metals such as Hg^{2+} or for detecting imbalances in ions such as Ca^{2+} since both can cause serious health issues. Upconverting particles can also be printed and used for security applications.[123, 129-131] For instance, UCNPs can be used to print quick response (QR) codes that are invisible without an excitation source[123]. A further level of security can be achieved by using UCNPs that have NIR to NIR emissions and adding a covering to the printed QR code with a black epoxy. Any visible emissions are then prevented from being transmitted and the NIR emissions require a camera to be observed.[123] Other security approaches have combined UCNPs with another fluorescent molecule, such as a carbon dot, to print dual-mode barcodes. By having multiple emitting species with different excitation and emission wavelengths, the bar codes are more challenging to counterfeit.[131] Finally, the low autofluorescence and sharp emission bands make UCNPs an ideal candidate for imaging applications. Both in vivo and in vitro high contrast imaging has been demonstrated using UCNPs[114, 132], and targeted imaging can be achieved by encapsulating them with antibodies.[132] UCNPs can also be used for

multimodal applications. For instance, the inclusion of Gd^{3+} allows the UCNPs to be used for magnetic resonance imaging applications[99, 121], and Figure 1.8d presents an UCNP that allowed for imaging in four modes.[124]

1.3.4   Synthesis strategies

A variety of strategies have been employed to produce UCNPs, however by far the most popular method used is thermal decomposition because this strategy allows the most control over particle crystallinity and morphology, allowing synthesis of monodisperse UCNPs. Both one-pot synthesis and hot-injection approaches have been widely studied.[92, 100, 116, 133] Both methods use high boiling point solvents such as octadecene or other long hydrocarbons and surfactants such as oleic acid, oleyl amine, and trioctylphosphine to control the UCNP size and growth. Typical lanthanide precursors include lanthanide acetates, trifluoroacetates, chlorides, or nitrates. In a typical one-pot strategy, the lanthanide precursors are heated with solvent and surfactant under argon or vacuum to free the trivalent metals from their ligands. The reaction solution is cooled, and both the sodium and fluoride sources are added. The reaction is then heated to 100 °C to remove water and any other volatile solvents and then is heated to the desired reaction temperature (typically above 300 °C[134]) to allow for UCNP formation.[116, 135] With the hot injection approach, separate solutions of solvent and surfactant and lanthanide precursors are heated to remove water. Then, the solvent solution is heated to the desired reaction temperature, followed by the rapid injection of the lanthanide solution. This allows a supersaturation of the precursors which facilitates homogeneous nucleation which is followed by UCNP growth.[133] With both methods, the accepted mechanisms suggest that initially, α-phase particles are formed followed by a transformation to the desired β-phase.[136] The final crystallinity of the UCNPs is highly dependent on the reaction temperatures, and concentrations of precursors.[100] The surfactant prevents aggregation of the UCNPs and also

controls the rate of nucleation and growth, the particle size, and the particle shape.[100, 133-134] While the thermal decomposition method allows control over both the size and phase of the final UCNPs, it suffers many drawbacks. Long hydrocarbons are used for the solvent because they have high boiling points that meet the requirement of high reaction temperatures. Additionally, the most common capping agent is an oleate ligand. These features result in production of a final product that is hydrophobic in nature. Further processing steps then need to be implemented to make the UCNPs biocompatible.[96, 137-138] Another major issue is the fact that despite allowing the best control, thermal decomposition still has reproducibility issues[100, 115]. Other reports have shown the production of mixed α- and β- phase particles[92, 136] and bimodal distributions of particle sizes.[100] The requirement of vacuum or inert environment and sensitivity of reactions to heating and cooling rates requires sophisticated equipment and multiple reaction steps. Finally, the thermal decomposition method often results in the production of many harmful byproducts, including fluorinated compounds.[100]

Other, simpler synthetic strategies have been implemented to try to address some of these limitations. Hydrothermal and solvothermal synthesis of UCNPs has also been widely studied.[86, 100, 107] With this method, an autoclave, typically consisting of a Teflon container that is enclosed in a metal vessel, is used to create a high-pressure environment which allows nucleation and growth of the UCNPs to occur at a temperature that is much higher than the boiling point of the solvent. This allows for solvents such as water, acetic acid or ethanol to be used[99] rather than the long hydrocarbons required in the thermal decomposition method. This method can also yield interesting shapes such as disks[139] and rods[140-141], however many of these products tend to be on the micron scale which is much larger than the nanoscale size preferred for biological applications. Molecules such as cetyltrimethylammonium bromide (CTAB), ethylenediaminetetraacetic acid (EDTA), citric acid (CA) or poly(ethylene glycol) (PEG) have been used to control the size, shape and solubility[99, 107, 142], however the high pressures and temperatures used risk damaging

the ligands. The hydro/solvothermal method typically results in fewer toxic byproducts than thermal decomposition but requires longer reaction times to achieve the desired β-phase. The coprecipitation method has also been used to prepare UCNPs. It offers the advantage of using lower temperatures and shorter reaction times. In a typical procedure, solutions containing the trivalent yttrium and lanthanides (often with nitrate or chloride counterions) were mixed with another solution containing the Na and F source (such as NaF or NH$_3$F and NaCl). Solvents such as water, ethylene glycol, or ethanol are commonly chosen. Both room temperature reactions[108, 143] and reactions involving heating ranging from 60 °C to 160 °C[100, 144-145] have been reported. By adding a chelating agent, such as polyvinylpyrrolidone (PVP) or EDTA, the size can be controlled and nanoscale crystals can be formed.[143-144] While the coprecipitation method is much simpler, uses lower temperatures, and produces fewer byproducts than the thermal decomposition method, it has several disadvantages. Both size control and UCNP agglomeration is a major challenge. Often, the UCNPs have poor upconversion PL efficiency. This is mainly due to the fact that UCNPs formed from the coprecipitation method are typically in the α-phase and require a second annealing step to convert to the β-phase.[100, 108] This annealing step can cause agglomeration of the UCNPs as well as carbonization of any capping agents present[138], and it often results in only partial conversion of the UCNPs from α- to β-phase.[108]

1.3.5   Surface Modification

The solubility of UCNPs is an important area of consideration for feasible implementation into applications. For biological applications it is crucial that the UCNPs are stable in aqueous media and buffers, and pH is also an important factor to consider depending on the targeted application.[92, 96, 99] Water is also the preferred solvent for many potential industrial applications, such as inkjet printing.[129] However, most UCNPs are

soluble in organic hydrophobic solvents such as hexane and toluene since the most common strategies to synthesize UCNPs with high degrees of crystallinity and upconversion efficiency result in oleate capping agents on the UCNP surface. Therefore, further modifications to the UCNPs need to be done to make them stable in aqueous environments. Several strategies have been implemented to modify the surface of UCNPs such as: chemically modifying the oleate ligand, bilayer coatings using amphiphilic polymers, oil in water emulsions, addition of an inorganic shell, or ligand exchange.[96, 137]

The typical strategy when reacting with the oleate ligand involves an oxidation of the C=C bond to form carboxy or epoxy groups to make the UCNPs water soluble.[137] However, this strategy presents many limitations such as challenging separation from reagents used during oxidation[146], poor colloidal stability, and a limited number of available functional groups that can be produced. Therefore, this strategy is not implemented frequently in practice.[137, 146] Another method implemented to modify the surface environment of UCNPs involves addition of a shell. In addition to changing the solubility of the UCNPs, the shell also passivates the surface thus protecting it from solvent quenchers and improving the upconversion efficiency. Several oxide-based shells that have been implemented include silica and titania coatings.[96] Fluorescent dyes or drug molecules can be doped into the shell, thus also having it serve as a delivery system. Metal shells such as silver or gold have also been used.[137] Since both of these noble metals have interesting plasmonic properties they can be used as plasmonic enhancers of the upconversion. For instance, Sudheendra e al. showed that the upconversion of α-phase NaYF$_4$:Yb/Er@Au and NaYF$_4$:Yb/Tm@Au and UCNPs had similar upconversion efficiencies to their uncoated β-phase counterpart due to plasmonic enhancement of the activator emissions.[104] While addition of shells can improve the solubility and luminescence properties of UCNPs, several factors must be considered. First, the addition of a shell has a tendency to significantly increase polydispersity of the sample[137], which is not desirable for many applications. Also, shells can induce strain and change the optical properties and

mechanosensitivity of the UCNPs.[103] For instance, Lay et al. showed that shells with compressive strain showed improved mechanosensitivity and a larger shift in the red-to-green ratio when under force when compared to UCNPs with no strain from their shells.[103] Clearly, the impact of the shells on the luminesce, colloidal stability, and polydispersity needs to be carefully considered when using this strategy to improve aqueous solubility.

The other main strategy to modify the surface coating is addition of new ligands, either in the form of a bilayer using amphiphilic polymers or by ligand exchange methods. In general, amphiphilic molecules with a long hydrocarbon chain can form a bilayer with the oleate ligands through van-der-Waals interactions with the oleate alkyl chain.[96, 137] Phospholipids have shown great promise for this strategy for biological applications, however they are quite expensive and difficult to synthesize and purify.[137] Other polymers such as poly (ethylene glycol) (PEG) or poly (acrylic acid) (PAA) can be modified with hydrocarbons to be used as an amphiphilic polymer to modify the UCNP surface.[96, 137] One drawback to this strategy, however, is the increased hydrodynamic diameter of the UCNPs which can result in an undesirable size depending on the application. The ligand exchange method has also widely been used and can be based on two strategies: 1) direct exchange of the old ligand with a new one or 2) stripping of the oleate with $NOBF_4$ followed by addition of a new ligand.[137] The direct replacement approach offers major disadvantages of particle aggregation, the requirement of excess ligands, and long reaction times for ligand exchange to complete. It also requires that the new ligand has a functional group that coordinates easily to the UCNPs.[137] The two step process has shown promise for a variety of capping agents, but adds an additional step which adds extra time and purifications that can lower the product final yield.[96, 115, 137] Wilhelm et al. reported a systematic comparison of UCNPs modified with several commonly used surface coatings.[115] They synthesized UCNPs on a large scale which allowed direct comparison on how the different coatings influenced their luminescent properties and colloidal stability. They showed that the addition of amphiphilic polymers, including 1,2-distearoyl-sn-

glycero-3-phosphoethanolamine-N-[amino(polyethylene glycol)-2000] (ammonium salt) (DPSE-mPEG(2000), poly(isobutylene-*alt*-maleic anhydride) (PMA), and PMA modified with 4-(aminomethyl)pyridine (Py-PMA), and α-methoxy-ω-amino poly(ethylene glycol) (PEG-PMA) all resulted in a brighter green than red luminescence. Samples were also modified by a ligand exchange of the oleate with a BF_4^- followed by replacement with a water-soluble ligand such as citrate, PAA, and PEO-10-OH-terminated phosphonic acid (PEG-PA). They found that samples modified by the ligand exchange method have a lower I_G/I_R ratio compared to those modified with amphiphilic polymers. However, all of the surface UCNPs modified showed colloidal stability. This work highlighted how the type of surface coating can be chosen based on desired application and can tune the I_G/I_R. However, it also pointed out the drawback of generally lower luminesce intensities for hydrophilic UCNPs compared to the precursor oleate capped UCNPs due to quenching from surface ligands and water molecules.[115] Another strategy that has been used to modify solubility is the formation of oil-in-water emulsions. A study by Meruga et al. demonstrated that stable inks could be prepared allowing for trapping of multiple UCNPs to increase brightness, and additives could be used to tune the viscosity and surface tension. These emulsions were stable up to 7 months however, their large size made them impractical for biological applications.[129] Finally, ligand free UCNPs have also been considered. A study by Bogdan et al. showed that at low pH values, hydrochloric acid could be used to strip the oleate ligand by protonation of the carboxy group. The UCNPs were colloidally stable in water based on electrostatic double layer repulsion.[146] They found that the upconversion intensity was highly dependent on the pH of the system and that stripping of the oleate ligand degreased the I_G/I_R ratio.[146] While all of the summarized strategies have shown promise to modify the surface of UCNPs to make them colloidally stable in water, they suffer the drawback of requiring additional steps, longer experimental times, use of many reagents, and extra purification which can result in loss of product, and it would be

advantageous to have a procedure that produces UCNPs that have both high upconversion efficiency, and are soluble in water without required additional surface modification.

1.3.6 Cytotoxicity considerations:

Finally, some areas of concern when using lanthanide-based NPs for biological applications are whether the UCNPs will have any cytotoxicity effects from the heavy metals within the system and considerations of how the UCNP properties will change in vivo as they interact with the biological environment. These issues have been addressed in studies done by several research groups. For instance, Buchner et al. investigated $NaYF_4$:Yb,Er,Gd@$NaYF_4$ core-shell UCNPs for PDT effects on breast cancer cells.[121] They functionalized the core-shell UCNPs with L-lysine and covalently bonded the photosensitizer Rose Bengal to the lysine molecules. They expected that when exciting the functionalized UCNPs with 980 nm light, the UCNPs would emit green photons that would excite the Rose bengal. The Rose bengal would then generate singlet oxygen and cause cell death. When investigating the cytotoxicity effects of these UCNPs they determined that for cells loaded with 15 μg/mL u\UCNPs, the functionalized UCNPs had 67% cell death when irradiated with 980 nm light for 6 minutes, however for the control samples that were kept in the dark they observed only 5% death. Laser scanning confocal fluorescence microscopy images of these cells revealed that for the samples irradiated with 980 nm light the cells had damage to the cell membranes and that the UCNPs accumulated in the nucleus of the cell, however this was not observed for the cells kept in the dark.[121] While the goal of this group's research was to demonstrate cell death through PDT effects, they also showed minimal cytotoxicity for cells loaded with lanthanide based UCNPs when they were not allowed to undergo PDT. A study by Lay et al. investigated biocompatibility and stability of ligand stripped $NaYF_4$:Yb,Er@$NaLuF_4$ UCNPs.[147] They investigated the stability of the UCNPs in various buffers and media commonly used in biological studies

and determined that S-Medium showed the best optical stability partially due to the cholesterol and citrate present in the S-Medium protecting the surface from phosphate ions that can adsorb to the surface and cause particle aggregation and quenching. They also demonstrated optical stability during pH cycling, which is important to consider for biological applications where the UCNPs will move to different pH environments such as for force sensing of the digestive tract. Then, they investigated cytotoxicity effects through brood assays of c. elegans that were fed their UCNPs for mechanical force sensing applications. They established that there was no significant variance in number of egg count between the c. elegans that were fed UCNPs and the control that were not fed any UCNPs, which indicated that the UCNPs were safe to use in c. elegans for digestive mechanical force sensing.[147] A study by Guller et al. considered the cytotoxicity effects that β-NaYF$_4$:Yb/Er UPNPs with various surface modifications had on two different types of skin cells: fibroblasts and keratinocytes.[148] They investigated the cytotoxicity using a 3-(4,5-Dimethylthiazol-2-yl)-2,5-Diphenyltetrazolium Bromide (MTT) assay which tests the mitochondrial activity of a cell. They determined that the fibroblasts showed no significant cytotoxic effects for all types of UCNPs they considered, however the keratinocytes showed a dependence both on dosage and surface coating. The bare UCNPs showed no cytotoxicity while the UCNPs coated with polyethyleneimine had the worst cytotoxicity with over 50% cell death. UCNPs coated with poly(maleic anhydride-alt-1-octadecene) and poly(D,L-lactide) had a moderate cytotoxic effect and only showed 10-25% reduction in cell viability. This work highlighted the importance of carefully considering both the type of cell used as well as the surface environment. The low cytotoxicity of the bare UCNPs and the high cell viability dependence on the surface environment also gives evidence that the cytotoxicity of UCNPs is caused by the surface coatings rather than the lanthanide ions.[148] These studies, among others, have shown that lanthanide based UCNPs are generally considered nontoxic[119, 149], however factors such as surface chemistry, size effects, dosage effects, where they accumulate in the body, and whether they decompose

and form harmful side products should be considered when designing UCNPs for biological applications.[150-151]

1.4 Laser ablation in liquid

The limitations of the methods described to prepare carbon dots and UCNPs make alternative strategies to prepare these nanomaterials highly desirable. Pulsed laser ablation in liquid (LAL), also termed liquid-phase laser ablation, has recently emerged as a promising alternative method to prepare carbon dots[56, 152-154], UCNPs[155-159], and various other nanomaterials[160-163]. In a typical setup, a bulk target is placed in water or another liquid and is placed incident of the laser. As the laser interacts with the target, it releases material which is then cooled by the surrounding liquid.[161, 164] LAL typically requires the use of fewer precursors, and results in production of fewer harmful byproducts, making it more environmentally friendly than other methods and requiring only simple purification steps. Production rates are much faster than other methods and gram-scale synthesis by LAL has been achieved.[160] LAL also allows for the formation of nanoparticles that are in the absence of a capping agent which can be advantageous for applications like catalysis where capping agents could block the active site.[161-162] The resultant product can be controlled by tuning the material parameters such as the bulk target, the solvent and any solutes present, addition of capping or stabilizing agents in the liquid, and the system temperature and pressure.[161-162, 164] The laser parameters including pulse width, repetition rate, focusing area, pulse wavelength, and pulse energy or fluence also can influence the particle size distribution, production rate, and formation mechanism.[161-162]

Two general mechanisms are considered to explain how nanomaterials are formed through LAL: thermal evaporation and explosive ejection. With thermal evaporation, laser irradiation incident on the target forms a plasma though photoionization, vaporization,

boiling, and melting.[164-165] This typically occurs with fast laser pulses that range from nanosecond to femtosecond, and the detachment of individual atoms and ions causes fragmentation of the target material. Unlike gas-phase laser ablation, the surrounding liquid confines the plasma to the target surface which extends the heating time and increases production yields.[164] The plasma reaches high temperatures and pressures on the order of 10^3 K and 10^9-10^{10} Pa, respectively. The high concentration of the plasma can cause supersaturation which allows nucleation to begin. Shockwaves that propagate into the target material and liquid are then generated which causes the plasma to quickly expand and release energy to the liquid, allowing it to reach temperatures similar to the plasma (on the order of 10^3 K). As the plasma expands, a cavitation bubble forms which quickly expands causing a quick drop in temperature and pressure. The cavitation bubble then collapses and emits a shockwave which allows release of the nanomaterials into the surrounding liquid.[166] In the case of longer laser pulse widths ranging from microsecond to millisecond, the explosive ejection mechanism dominates. The heating is slower, and detachment is dominated by vaporization and boiling. Nanodroplets that retain similar composition to the bulk target are ejected and can then react with the surrounding liquid.[165] In addition to pulse width, laser parameters such as fluence or wavelength can impact the observed mechanism. In some materials, low laser fluences can preferentially cause vaporization of elements that have low melting points, boiling points, enthalpies of fusion, and enthalpies of vaporization while those with higher values for these thermodynamic properties remain in the bulk target. Increasing the laser fluence can cause more uniform heating and detachment of the target resulting in a material that more closely resembles the bulk.[167] The laser fluence can also impact the size of the nanomaterial with higher fluences often resulting in smaller particles.[168] In cases where the target absorbs the laser wavelength strongly, it can cause heating of the target leading to heterogeneous boiling or explosive boiling.[168] Reactions with the liquid can also cause surface oxidation or other composition changes,[163, 165] and capping agents in solution can be used to control the

growth of particles.[164, 169] Finally, solution based LAL approaches can be used to either photoreduce ionic metals and induce clustering into nanoparticles[165] or to size refine and modify the surface of colloidal suspensions.[161]

2.1 Introduction and motivation

Since its first isolation in 2004[170], graphene has shown a wide range of potential applications[34, 171-173] due to its high charge carrier mobility and thermal conductivity, large surface area to mass ratio, strength, hardness, and flexibility.[34-35] However, graphene is a zero-bandgap material which limits its use in applications such as photovoltaics, transistors and light emitting diodes, which require a measurable and tunable band gap. This has inspired the development of many graphene derivatives, including graphene quantum dots (GQDs), graphene nano ribbons, graphene nanoflakes, graphene oxides, graphane, and fluorographene,[154, 174] which exhibit non-zero bandgaps because of their small particle sizes or the inclusion of non-carbon atoms, and GQDs in particular have emerged showing versatile application in photovoltaics, photocatalysis, biosensing, bioimaging, and photodynamic therapy.[13, 32, 175] GQDs are considered a zero-dimensional nanomaterial that consists of a graphitic carbon backbone that typically has a thickness ranging from a single to five graphene layers and generally not exceeding 10 nm in diameter.[33] The backbone is terminated on the edges by either hydrogen atoms or with functional groups, and depending on the reaction conditions, functional groups can also be present on the basal planes. GQDs are non-toxic and environmentally friendly, and they exhibit photoluminescence (PL) with a good photostability and broad emissions in the ultraviolet, visible and near infrared regions.[58] Several factors contribute to the absorbance and emissive properties of GQDs.

The presence of sp^2 hybridized nanodomains allows for size- dependent absorbance and emission through the quantum confinement effect, and a mixture of different sp^2 domain sizes in a sample affords excitation-dependent emission.[59] The PL from these size effects are often termed intrinsic emission. On the other hand, the presence of localized nanostructures from zigzag and armchair edges[60] and from oxygen containing functional groups on the edges and surfaces leads to so-called extrinsic emission. GQDs often exhibit a combination of both intrinsic and extrinsic emissions,[29] and these unique optical properties allow GQDs to be viable in such a wide range of applications. Therefore, it is desirable to be able to produce GQDs with strict control over these properties.

Many top-down methods, such as hydrothermal cutting, chemical oxidation, electrochemical cutting, and nanolithography, and bottom-up methods including stepwise organic synthesis, solvothermal synthesis, and chemical vapor deposition have been employed to prepared GQDs,[32-33] however these methods suffer many disadvantages, including the use of harsh chemicals, the production of harmful byproducts, tedious product purification process, and the limited control over the product sizes, compositions, and structures. Liquid-phase laser ablation (LA) is an alternative, single-step method that offers several advantages over traditional chemical syntheses in the production of nanomaterials including use of fewer chemical precursors, production of fewer harmful byproducts, fast nanomaterial production, and control over the resultant product by tuning the laser synthesis parameters, the liquid used, and by the presence of solutes in the liquid. [160, 164, 169] In general, two mechanisms are proposed for how nanomaterials are formed through liquid-phase LA: thermal evaporation vs. explosive ejection. With thermal evaporation, irradiation of the laser causes the solid target to form a high temperature and high-pressure plasma at the solid-liquid interface. This plasma adiabatically expands, interacts with, and is condensed by the surrounding medium to quickly form clusters.[165] Alternatively, explosive ejection causes surface melting of the target and the formation of nanodroplets upon the incidence of a laser. These nanodroplets are then ejected into the

liquid and react at their surfaces with the liquid medium to form nanomaterials.[176] Distinguishing between the two mechanisms can allow for better understanding for further control of the nanomaterials produced by liquid-phase LA.

Recently, liquid-phase LA has been demonstrated as a clean and efficient one-step method to fabricate GQDs both through bottom up methods using precursors such as toluene[177] or chlorobenzene[178] and through top-down synthesis with larger precursors including solutions of multiwalled carbon nanotubes (MWCNTs),[56] dispersions of graphite powders,[179] and highly oriented pyrolytic graphite (HOPG) targets in water.[180] It was demonstrated that the use of MWCNTs with ultrathin carbon walls allowed for better size control over the GQDs when compared to bulky carbon targets such as HOPG and that the choice of solvent allowed for tuning of the PL properties.[181] It has also been reported that use of HOPG as a carbon precursor produces mixed samples that consist of both GQDs and larger products such as graphene sheets or porous graphene.[180, 182] while the use of smaller precursors such as graphene oxide allowed for production of more uniform samples.[183] Other parameters, such as laser-ablation time, allowed for control over the concentration of surface functional groups[154] and influenced the size of GQDs formed through liquid-phase LA.[184] Laser power, pulse width, and the focused spot size as well as the composition of precursors also affected the size distribution and PL properties of the resultant GQDs.[177, 185-186] However, to our knowledge, there is yet to be a detailed comparison of GQDs produced from similar materials through traditional chemical methods and liquid-phase LA. We report a systematic comparison of GQDs produced by chemical oxidation (CO) and liquid-phase LA methods. It was observed that the LA-GQDs have a blue shifted absorbance and PL relative to the CO-GQDs. This change in optical properties is attributed to both a smaller particle size and thus smaller sp^2 domains, and a higher concentration of hydroxyl functional groups. It was determined that the oxygen containing functional groups were the dominant source of radiative decay, while the intrinsic states from the sp^2 domains were only weakly emitting. Liquid-phase LA has

38

successfully been presented as a reproducible method that is cleaner and faster in production and produces the GQDs with smaller size dispersion.

2.2 Experimental details

A description of the materials used, and the sample characterization can be found in the supporting information (section 2.5).

2.2.1 Carbon-nano onion preparation

Nanodiamond-derived carbon nano-onions (nCNOs) were synthesized according to a previously published procedure.[43] Briefly, the nCNOs were derived from commercially available detonation nanodiamonds (average diameter 6 nm). The nanodiamonds were thermally annealed in a graphitization furnace under helium flow at 1650°C for 1 hour.

2.2.2 GQD preparation

2.2.2.1 Preparation of CO-GQDs

Chemically oxidized GQDs were produced through a modified hummer's method. In a typical procedure, 200 mg nCNOs were mixed with 66 mL sulfuric acid and 34 mL nitric acid. The mixture was under reflux at 105 °C for 4 hours. The sample was then cooled to room temperature and neutralized with KOH, filtered, and dialyzed for two weeks using dialysis tubing (molecular weight cut off: 1 kD). Following dialysis, the GQD solution was filtered using a 450 nm syringe filter.

2.2.2.2 Preparation of LA-GQDs

Figure 2.1 depicts the experimental setup for liquid-phase LA to produce GQDs. In a typical experiment, nCNOs were pressed into a pellet at 15,000 psi and kept under the pressure for 15 minutes. This pressure was chosen because it allowed the pellet to remain intact throughout the duration of the ablation. The pellet was transferred to a vial, and 3 mL of deionized water was added. A quartz lid was used to minimize the loss of the deionized water due to evaporation. A Spectra-Physics Quanta-Ray® GCR-3 Q-switched Nd:YAG laser equipped with a harmonic generator was used to produce 532 nm light. The laser pulse width at 532 nm was 5-7 ns, and the repetition rate was 10 Hz. The laser beam was directed downward with a quartz prism, and the focal point of the laser beam was adjusted to a size of about 2 mm diameter using a focal lens. The vial containing the nCNO pellet was placed incident of the laser on a rotating stand. The ablations were carried out at 1.30 W for 7 hours to allow for a sufficient amount of sample to be produced. Following ablation, the liquid was collected and filtered with a 450 nm syringe filter prior to analysis. Experiments were also run at 0.11, 0.57, and 0.95 W to test for any power dependence on the resultant sample.
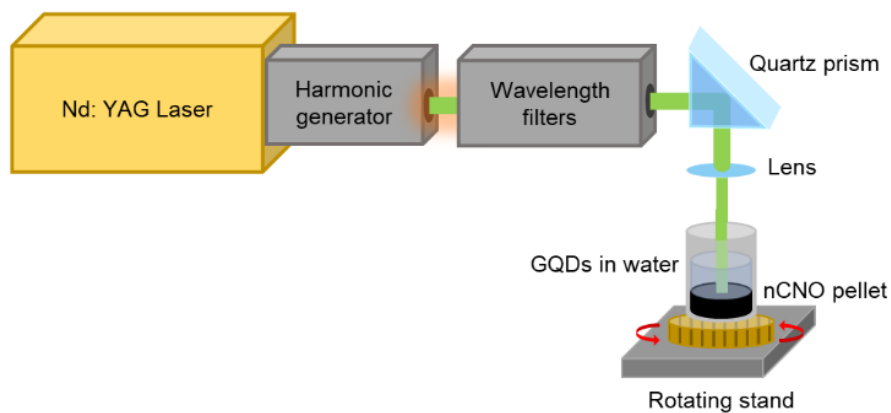
Figure 2.1 Schematic representation of a laser ablation setup

2.3   Results and discussion

2.3.1   Optical and size characterizations

Optical characterizations of the precursor nCNOs are reported in the Supporting Information (Figure S2.1a). Prior to the GQD formation, the nCNOs show continuous absorbance in the range from 200 nm to 800 nm with no defined peaks (Figure S2.1a), indicating that the precursor is a metallic, zero-bandgap material. The nCNOs show no PL when they were excited at various wavelengths (Figure S2.1b). The sharp, excitation wavelength-dependent peaks superimposed on the PL spectra are due to Raman scattering of the deionized water. Following CO or liquid-phase LA, well-defined absorbance peaks appear (Figure 2.2a), suggesting the formation of quantum confined particles. The CO-GQDs show a peak at 230 nm from the π-π* transitions of the aromatic carbon backbone, shoulders at 265 nm and around 350 nm from the n-π* transitions of the functional groups, and weak, continuously diminishing absorbance at longer wavelengths. Compared to the CO-GQDs, the LA-GQDs show a shift in the π-π* transition to a shorter wavelength at 210 nm, reduced intensities for the n-π* transitions, and nearly zero absorbance at wavelengths longer than 500 nm. The negligible absorbance of the LA- synthesized GQDs at $\geq$ 500 nm allowed for the 532 nm beam to transmit through the solution to the pellet with a minimal loss of the laser power. The shift of the π-π* transition to a shorter wavelength for the LA-GQDs gives evidence that these GQDs have smaller sp^2 domain sizes than the CO-GQDs through the quantum confinement effect which states that as the size of a nanomaterial becomes smaller its bandgap is increased. The difference in the n-π* transition intensities suggests that the functional groups or the relative ratios of these functional groups on the GQDs are different between the CO- and LA-GQDs.
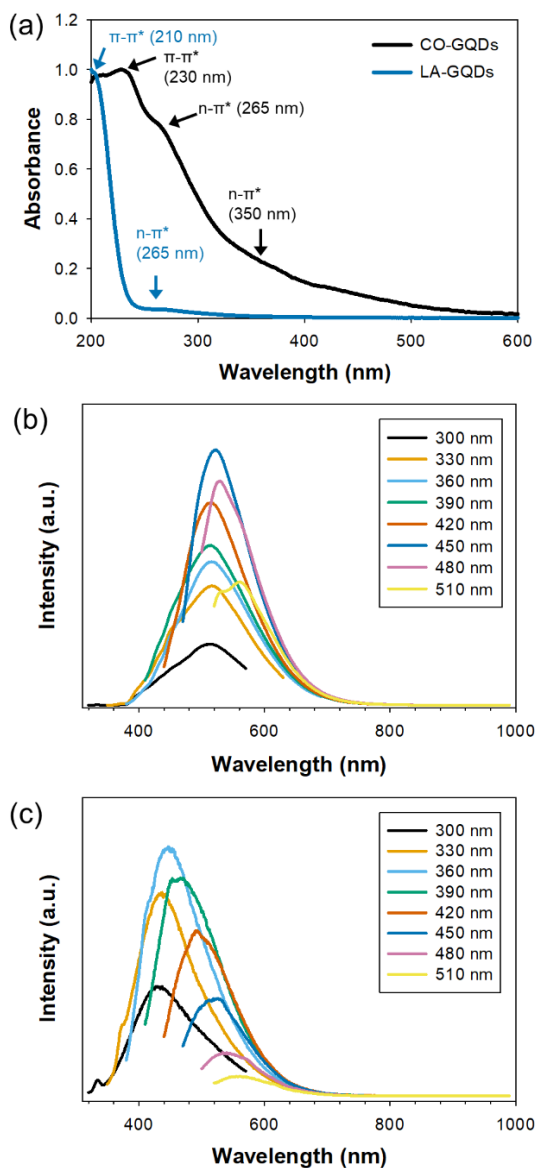
Figure 2.2 UV-Vis absorbance (a) and photoluminescence spectra of the CO-GQDs (b) and LA-GQDs (C).

Considerable PL differences are also apparent between the CO- and LA-GQDs. Although both samples exhibit excitation wavelength-dependent emissions, such dependence is much stronger for the LA-GQDs. This could give evidence of greater disorders of the LA-synthesized GQDs. The peak emission of the CO-GQDs with 300-510 nm excitations (Figure 2.2b) all occurs at around 515 nm, with 450 nm excitation giving

the strongest emission. The peak emission of the LA-GQDs is noticeably blue-shifted from that of the CO-GQDs. The LA-GQDs show peak emission occurring at 445 nm with 360 nm excitation. It may not be surprising that the maximum emission of the LA-GQDs occurs at a shorter excitation wavelength since they absorb weakly at longer wavelengths.[187] These differences in PL suggest that the LA-GQDs have a different chemical structure than the CO-GQDs. Figure S2.2(a-d) shows the PL spectra of several LA-GQD samples produced at various laser powers. For all spectra, the entire sample produced by liquid-phase LA was collected and dissolved in 3 mL of water. A clear increase in PL intensity is observed with the increase in laser power (Figure S2.2e). Such a PL enhancement is due to a greater amount of GQD production at a higher energy per surface area (laser fluence),[161] which is also demonstrated by the increased absorbance at a given wavelength with increasing laser fluence (Figure S2.2f). Although the laser power effect was investigated with higher laser power, power larger than 1.3 W caused destruction of the nCNO pellet and prevented further laser ablation. Figure S2.3 (a-c) shows the PL spectra of three LA-GQD samples produced with the same LA parameters and demonstrates the reproducibility of this method.

To further understand the differences in the PL of the CO- and LA-GQDs, we investigated the sizes of the GQDs. Figure 2.3 presents the images obtained by transmission electron microscopy (TEM) and the lattice profiles of the GQDs produced by both methods. From these images and lattice profiles, the average diameter of the CO-GQDs is measured to be 4.1(8) nm (Figure 2.3a), and the lattice spacing is 0.21 nm (Figure 2.3(b,c)), which corresponds to the [110] plane of graphite.[188] The average diameter of the LA-GQDs is slightly smaller (1.8(6) nm) (Figure 2.3d), whereas their lattice spacing is larger (0.31 nm) (Figure 2.3(e,f)). The larger lattice spacing of the LA-GQDs could be due to their higher relative concentration of the hydroxyl groups, which widen the carbon backbone gap.[189] Additionally, the smaller crystalline diameter of the LA-GQDs indicates a less ordered structure than the CO-GQDs.

Atomic force microscopic (AFM) images and their line scans (Figure 2.4) show that the CO-GQDs have an average particle height of 6.3(19) Å (Figure 2.4(a,b)) which corresponds to the stacking of two or three graphene layers, and the LA-GQDs have an average particle height of 3.5(10) Å (Figure 2.4(c,d)), indicating that the LA-synthesized particles are mostly single layered. The smaller size of the LA-GQDs explains the shift of the π-π* transition observed in the absorbance to shorter wavelengths, and the lower standard deviation indicates better size uniformity than the CO-GQDs. The smaller sizes of the LA-GQDs could also contribute to the observed blue shifted PL.
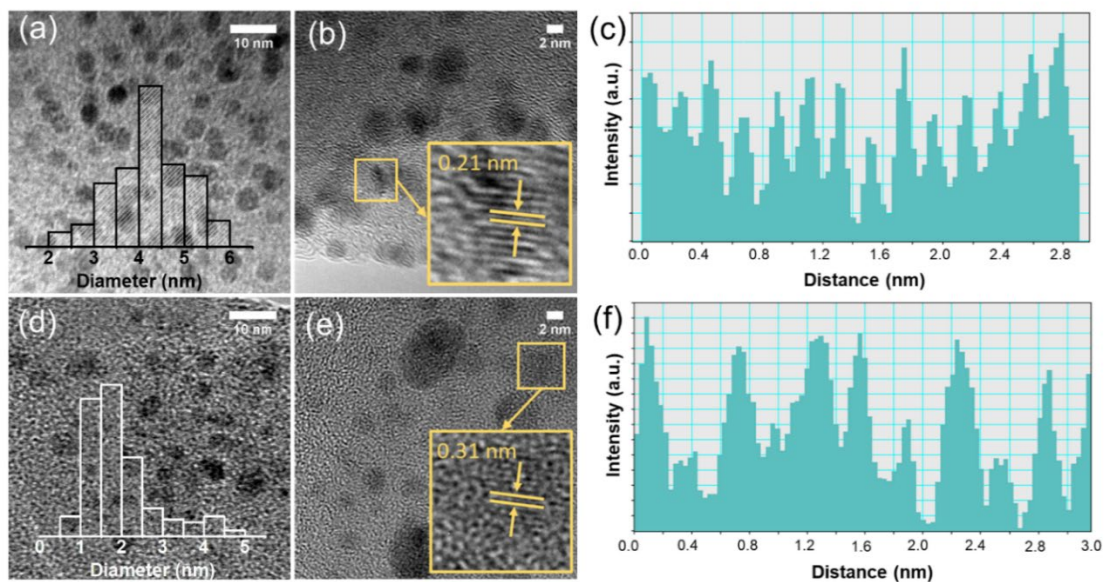
Figure 2.3 TEM images and lattice profiles of the CO-GQDs (a-c) and LA-GQDs (d-e). The inset histograms in the TEM images show the GQD diameter distributions.
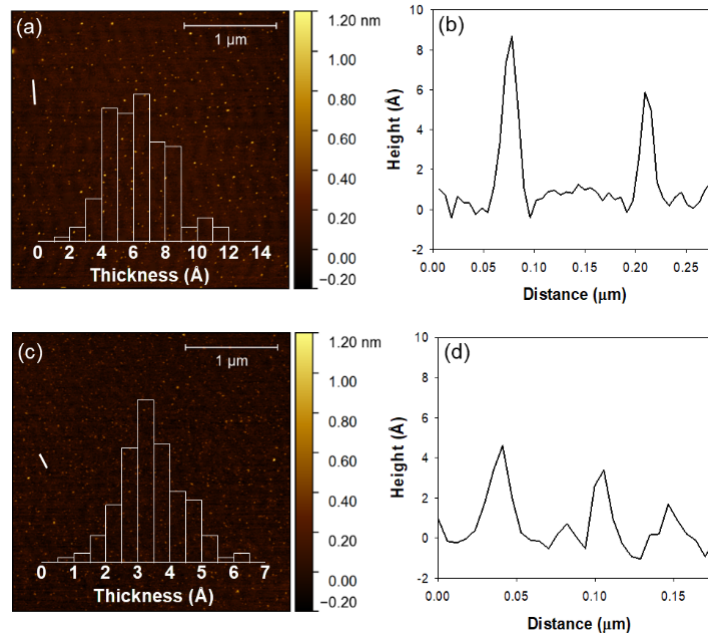
Figure 2.4 AFM images and the corresponding height profiles for the CO-GQDs (a, b) and LA-GQDs (c, d). The lines in the AFM images indicate where the line profiles were measured. The inset histograms show the particle height distributions.

2.3.2 Functional group characterization

Differences in functional groups present on the GQDs were also suspected to contribute to the different PL properties so XPS and FT-IR were used to investigate the functional groups present. Figure 2.5a shows the XPS survey spectra of both CO- and LA-GQDs. The survey spectrum of the CO-GQDs shows an O1s peak at 532.1 eV, a C1s peak at 285.3 eV, and a K2p peak at 293.4 eV. The presence of the K2p peak is due to residual potassium from the neutralization procedure that was not separated out during dialysis. From the O1s and C1s peak intensities, the CO-GQDs are found to contain 57.2% carbon and 42.8% oxygen by molar ratio. The survey spectrum of the LA-GQDs shows an O1s peak at 531.9 eV, a C1s peak at 285.3 eV, a Na1s peak at 1071.2 eV, and a Na LK1 Auger peak at 497.0 eV. The presence of the Na1s and NaLK1 peaks is due to a slight sodium contamination from the cleaning solution used to prepare the glassware for liquid-phase LA. For the LA-GQDs the carbon to oxygen ratio is 43.5% carbon and 56.5% oxygen. The

increase in the relative amount of oxygen of the LA-GQDs is due to their smaller sizes, which lead to an increased surface to volume ratio and thus an increase in the total number of surface hydroxyl groups. The survey spectra of both CO-GQDs and LA-GQDs show that in addition to the trace Na and K atoms, oxygen is the only heteroatom present on the GQDs' surfaces, which suggests that only oxygen containing functional groups will be present in both GQDs.
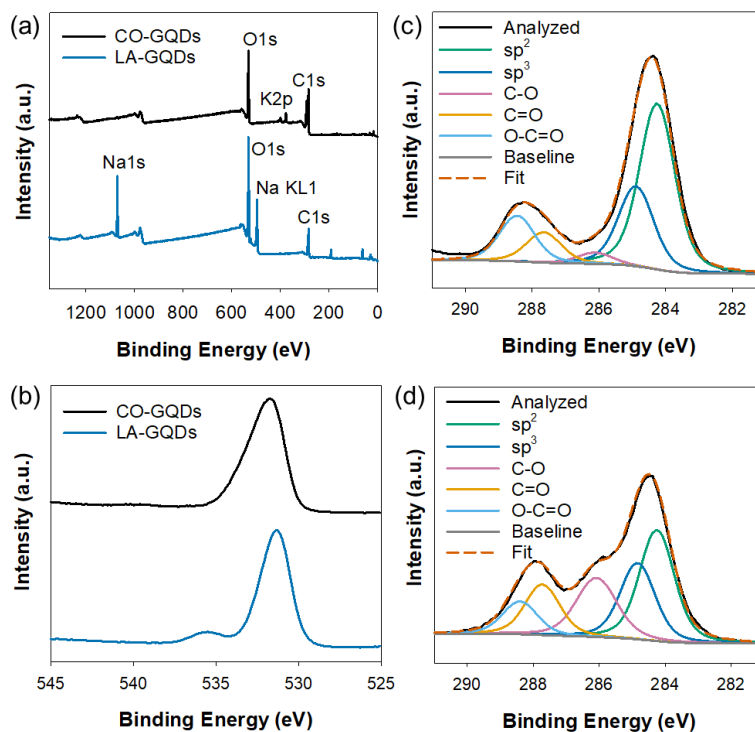
Figure 2.5 Survey XPS spectra (a) and high resolution O1s (b) and C1s (c for the CO-GQDs and d for the LA-GQDs) spectra of the CO- and LA-GQDs.

High resolution XPS scans around the O1s region (Figure 2.5b) show broad O1s peaks at 531.5 eV for both the CO- and LA-GQD samples and a minor Na KL2 Auger peak at 536.1 eV for the LA-CODs only. The broadness of the O1s transition suggests that surface oxygen atoms must be in different bonding environments (or different functional groups) in both samples. The main difference between the CO- and LA-GQDs is the shape of the O1s peak, which is clearly asymmetric at the higher energy side for the former but

symmetric for the latter. The different shapes of the O1s peak are of an indication that the CO- and LA-GQDs contain different types or ratios of the oxygen-containing functions groups. This difference is more clearly demonstrated by the high resolution C1s spectra in Figure 2.5(c, d). Although the C1s spectrum of both samples can be best deconvoluted into five peaks corresponding to sp^2, sp^3, hydroxyl C-O, carbonyl C=O, and carboxylic O-C=O carbon bonding, the relative areas of these peaks are considerably different between the CO- and LA-synthesized GQDs. Table 2.1 summarizes the C1s binding energies and percentages of each type of carbons determined from the deconvoluted peak areas of XPS C1s spectra. As expected, the binding energies of each type of C1s electrons in the two samples are similar to each other. However, although both samples contain more carbons in the backbone than the oxygen-bonded carbons in the functional groups, the CO-GQDs have a much larger fraction of the backbone carbons (73.9%) than the LA-GQDs (55.1%) (or a smaller fraction of the oxygen-bonded carbons (26.1%) than the LA-GQDs (45.0%)). In general, smaller particle sizes have higher surface to volume ratios and thus are able to accommodate more surface functional groups. The observation thus suggests that the GQDs prepared by LA are smaller than those synthesized by CO, consistent with the TEM measurements described previously. Moreover, the CO-GQDs have more sp^2 backbone carbons (49.8%) than the LA-GQDs (32.6%), indicating that the former has a larger sp^2 carbon domain than the latter, consistent with the AFM measurements.

Table 2.1 C1s binding energies and fractions of various carbons in the CO- and LA-GQDs determined by XPS

Assignment	C1s binding energy (eV)	CO-GQDs	LA-GQDs
sp2	284.3	49.8%	32.6%
sp3	284.9	23.9%	22.5%
C-O	286.1	3.5%	20.2%
C=O	287.7	9.0%	15.0%
O-C=O	288.5	13.9%	9.8%

Various particle sizes also explain the difference in ratios of the oxygen containing functional groups as summarized in Table 2.2. It has been shown that O-H groups are more stable than C=O or C-O=C groups on smaller GQDs, smaller particles thus are expected to favor a higher relative concentration of O-H surface functional groups.[68] For the LA-GQDs, hydroxyl –bonded carbons are dominant accounting for 44.9% of the oxygen bonded carbons, while carbonyl and carboxylic carbons account for 33.3% and 21.8%, respectively. For the CO-GQDs, carboxylic groups are dominant accounting for 53.7% of the oxygen bonded carbons, while hydroxyl-bonded and carbonyl carbons account for 13.3% and 34.0%.

Table 2.2 Relative amounts of the oxygen-containing functional groups of the CO- and LA-GQDs.

Assignment	CO-GQDs	LA-GQDs
R-C-OH	13.3%	44.9%
R-C=O	34.0%	33.3%
R-COOH	52.7%	21.8%

Figure 2.6 shows the normalized FT-IR spectra of both CO-GQDs (top) and LA-GQDs (bottom). The CO-GQD spectrum shows a strong broad phenolic O-H stretching band at 3450 cm^{-1}, a broad carboxylic O-H stretching band at 2500 cm^{-1}, a sharp C=O stretching peak at 1700 cm^{-1}, a strong and sharp aromatic ring stretching peak at 1600 cm^{-1}, a sp^2 carbon-bonded phenolic C-O stretching peak at 1225 cm^{-1}, and a CH$_2$ bending transition at 1450 cm^{-1}. Compared to the CO-GQDs, the LA-GQD spectrum displays greatly diminished intensities of the carboxylic O-H, C=O, and sp^2 bonded phenolic C-O stretches as well as a relatively weaker aromatic ring stretch, but new transitions corresponding to the sp^3 C-H stretch at $\sim$ 3000 cm^{-1}, CH$_3$ bend at 1380 cm^{-1} and sp^3 carbon-bonded alcoholic C-O stretch at 1100 cm^{-1}.[190] Overall, the FT-IR data indicates that the LA-GQDs have less aromatic sp^2 carbons and carboxylic groups, but more sp^3 carbons and hydroxyl groups than the CO-GQDs. The dominance of the sp^3 carbons over the sp^2

carbons, the larger concentration of the O-H groups, and fewer carboxylic groups in the LA-GQDs determined by FT-IR are consistent with the XPS results discussed above.

The difference in the surface functional groups offers insight into the observed optical properties. It has been reported that a carboxylic substitution has a greater effect on the n-π* absorption transition than a hydroxyl substitution.[63] This effect is also evident from our UV-Vis absorption spectra as the CO-GQDs show much stronger absorption in the n-π* region than the LA-GQDs. The higher fraction of the hydroxyl groups also contributes to the blue shifted emission of the LA-GQDs. It has been shown that chemically reducing GQDs with sodium borohydride increases the ratio of hydroxyl to carboxylic groups while preserving the size and structure of the GQDs, shifts emission to the blue and enhances PL quantum yield compared to the GQDs prior to chemical reduction.[191-192] Further reactions to remove the hydroxyl groups quenches the PL, demonstrating that the blue shift is due to the increased surface concentration of hydroxyl groups.[191] This suggests that the hydroxyl functional groups in these systems behave more as localized, molecule-like states rather than acting as electron donating groups to the intrinsic state, which would have an opposite effect inducing a PL red shift due to an increase of the energy of the highest occupied molecular orbital and thus a decreased bandgap.[64, 193] We observe a similar effect with the LA-GQDs. Although the LA-GQDs have smaller sizes compared to the CO-GQDs, which could cause the blue shifted emission, we suspect that the extrinsic emission from the surface functional groups is the dominating contribution to the emission, and the blue shifted emission thus is due to the higher relative number of hydroxyl groups, whereas the longer wavelength emission of the CO-GQDs is due to the higher relative number of the carboxylic groups. Additionally, because they are smaller in diameter, the LA-GQDs should have a higher surface to volume ratio of these functional groups and further enhance blue emission.
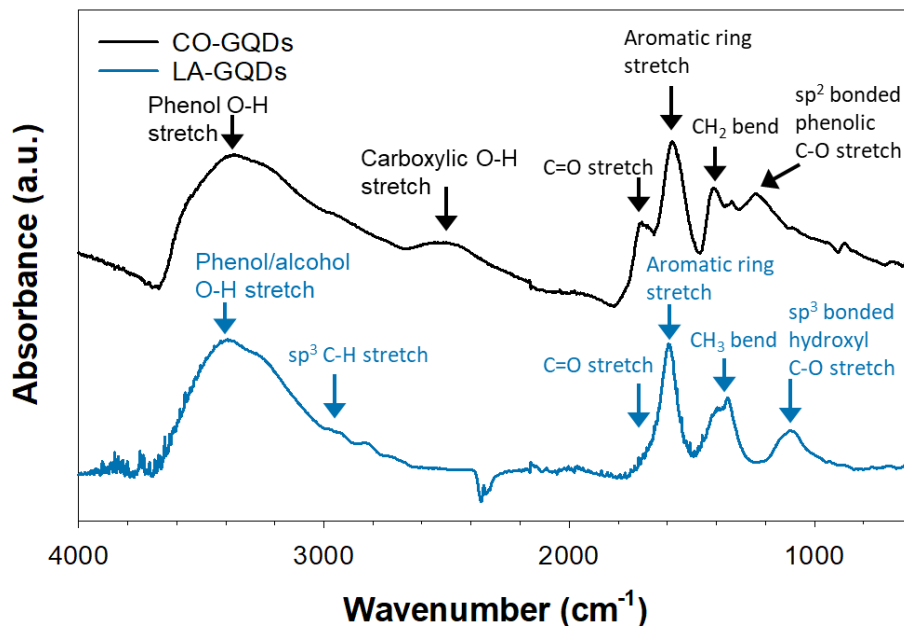
Figure 2.6 Normalized FT-IR of the CO- (black) and LA-GQDs (blue).

2.3.3 Photoluminescence lifetime results

To further understand the PL mechanism, we investigated the PL lifetime of the GQDs using TCSPC. The measurements were obtained using a 333 nm excitation source, and emission was measured at 430, 475, and 515 nm because the LA-GQDs exhibit strong emission at 430 nm, the CO-GQDs exhibit strong emission at 515 nm, and both types of the GQDs exhibit moderate emission at 475 nm. The instrument response function was determined by measuring the scattering of a ludox solution at 333 nm emission. Figure 2.7(a, b) shows the PL decay curves of the CO-GQDs at 515 nm emission and the LA-GQDs at 430 nm emission. The PL decay curves for the remaining emission wavelengths for both CO- and LA-GQDs are shown in Figures S2.4 and S2.5, respectively. The decays were fit to three exponential functions, and the resultant lifetimes and their relative contributions are tabulated in Table 2.3. The exponential fit parameters are tabulated in Tables S2.1 and S2.2. Both CO- and LA-GQDs show a fast component, τ_1, which is attributed to the intrinsic states of the GQDs,[61] and two slower components, τ_2 and τ_3, which

50

are attributed to decays of the various extrinsic states from the surface functional groups. Interestingly, we have observed changes in the relative contributions at different emission wavelengths. For the CO-GQDs, at 430 nm emission the intrinsic component of 0.66 ns is the dominant deactivation process with a relative contribution of 63%. As the emission moves to longer wavelengths, the relative contribution from the intrinsic effects becomes smaller, with a relative contribution of 52% at 475 nm and 34% at 515 nm; however, the lifetime remains unchanged, which suggests uniformity in the intrinsic states. At 515 nm emission, the deactivations due to surface functional groups dominate with $\tau_2 = 2.51$ ns and $\tau_3 = 7.90$ ns contributing 37% and 28%, respectively. As with the τ_1 intrinsic state, τ_2 and τ_3 do not change with emission wavelength.
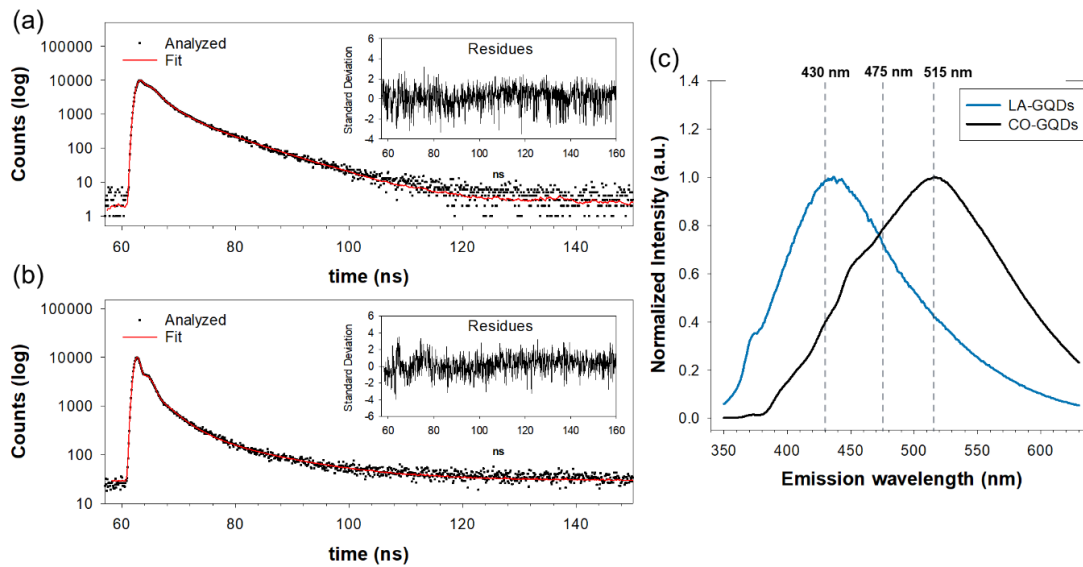
Figure 2.7 TCSPC decay curves of the CO-GQD 515 nm emission (a) and the LA-GQD 430 nm emission (b) at 333 nm excitation. The red lines show the fits and the insets present the residues for three exponential fits. Overlaid emission spectra of the CO- and LA-GQDs at 333 nm excitation (c).

The LA-GQDs show a slightly different trend. For all three emission wavelengths, the intrinsic deactivation process is dominant. However, the τ_2 and τ_3 deactivations from the surface functional groups show their strongest contributions at 430 nm emission with

19% for τ_2 and 11% for τ_3. It also should be noted that the τ_1 component is much faster for the LA-GQDs, which is likely due to the increased disorder from a higher sp^3 carbon fraction that provides more non-radiative pathways leading to the increase of the deactivation rate. Figure 2.7c presents the emission profiles of the CO- and LA-GQDs excited at 333 nm. Among the three marked emission wavelengths, the CO-GQDs displays the strongest emission at 515 nm, where the deactivation processes from the surface functional groups have their strongest contributions, and the weakest emission at 430 nm, where the intrinsic deactivation has the highest contribution. On the other hand, the LA-GQDs exhibit the peak emission at 430 nm, the same position where the surface functional groups have their strongest contributions. As the emission moves towards the red, the intensity decreases as do the relative contributions of τ_2 and τ_3. Based on these observations, we conclude that the surface functional groups on the GQDs are much brighter states than the intrinsic states.[36] Going further, we have observed that for the CO-GQDs the relative contribution of τ_2 only changes slightly as the emission moves from 430 nm to 515 nm; however, the relative contribution of τ_3 increases significantly from 7% at 430 nm to 28% at 515 nm. Since the carboxylic groups are the dominating functional groups present on the CO-GQDs, and the PL intensity increases with the increasing contribution of τ_3, we envision that the τ_3 lifetime is due to deactivations of the carboxylic functional groups. For the LA-GQDs, the relative contribution of τ_3 remains fairly constant at all three emission wavelengths but the contribution of τ_2 is the highest at 430 nm emission. Because the higher concentration of hydroxyl groups has greater influence on the blue shifted emission, we predict that the τ_2 lifetime is due to deactivations of the hydroxyl functional groups. Finally, it should also be noted that the high relative contribution from intrinsic deactivations is consistent with the absorbance which shows the π-π* transition as the dominant transition with only weak n-π* transitions from surface functional groups.

Table 2.3 Lifetimes(τ_1, τ_2, and τ_3) of emissions (λ_{em}) and their relative contributions (%) for the CO- and LA-GQDs measured by TCSPC at 333 nm excitation.

	λ_{em} (nm)	τ_1 (ns)	% τ_1	τ_2 (ns)	% τ_2	τ_3 (ns)	% τ_3
CO-GQD	430	0.66(2)	63(2)	2.31(6)	30(2)	8.5(2)	7(2)
	475	0.63(2)	52(2)	2.33(5)	36(2)	8.07(12)	37(3)
	515	0.63(2)	34(2)	2.51(12)	37(2)	7.9(6)	28(2)
LA-GQD	430	0.093(8)	69(4)	3.18(10)	19(2)	12.5(2)	11(3)
	475	0.103(8)	73(4)	2.569(13)	13(2)	8.8(2)	15(4)
	515	0.135(14)	77(5)	2.00(3)	11(3)	7.9(4)	12(5)

Based on the observed LA-GQD composition, the thermal evaporation mechanism for GQD formation is proposed. The laser is incident on the nCNO precursor and causes fast ejection of carbon atoms, ions, and small fragments of the nCNOs which then form a dense plasma. The plasma is quickly condensed by the deionized water, and nucleation of carbon clusters begin to form. Further laser pulses cause more plasma formation, and the species grow on the existing nuclei and also react with the surrounding water. This growth process is evidenced by the large fraction of sp^3 carbons. The reliance on water as the sole oxygen source leads to the higher surface concentration of the hydroxyl groups. If the explosive ejection mechanism was observed, we would expect to observe larger sp^2 domains retained from the source material. The larger observed fraction in sp^3 character contributes to a higher amount of disorder within the LA-GQDs, and we speculate that a more accurate description of the LA-GQD structure is that a particle contains several small sp^2 domains within a sp^3 matrix. As observed in the FT-IR spectra, the hydroxyl groups are mostly bonded to sp^3 carbon which isolates them from the intrinsic states. This allows the hydroxyl groups to behave as separate emitting species rather than as electron donating groups to the intrinsic states which would shift the emission to longer wavelengths. Non-uniformity in the size of the sp^2 domains could account for the observed excitation-

dependent emission despite the uniform sizes of the particles. This disorder also likely has a high contribution to the non-radiative decay of the LA-GQDs as it increases the rate constant of non-radiative relaxation path, k_{nr}, as evidenced by the much faster τ_1 intrinsic lifetime of the LA-GQDs compared to the CO-GQDs. Finally, as a note on nomenclature, we refer to the particles synthesized through liquid-phase laser ablation as LA-GQDs for consistency when comparing them to CO-GQDs. However, based on the small sizes of the graphitic sp^2 domains and high fraction of sp^3 carbons, a more general name such as carbon nanodots could also be used to describe these particles.

2.4   Concluding remarks

In summary, we have presented liquid-phase LA as a fast, single-step, and clean method to prepare GQDs from nCNOs. Compared to those prepared through chemical methods, these GQDs have smaller and more uniform sizes and show blue shifted absorbance and emissive properties with peak PL observed at 445 nm. A combination of the smaller sp^2 domains and the larger fraction of the hydroxyl functional groups is responsible for the blue shifted emission. However, we have determined through TCSPC that the intrinsic states have the fastest lifetimes and are weak emitting states, while the surface functional groups have slower lifetimes and are much stronger emitting. This suggests that the PL properties are more dominantly affected by the nature of the functional groups present and only minimally through size effects of the intrinsic state, and that by careful selection of functional groups present PL can be tuned to desired wavelengths. Because of the thermal decomposition mechanism, the LA-synthesized particles are similar to those produced through reported bottom up approaches. Our work suggests that the liquid-phase LA method can be expanded to prepare GQDs from other source materials or in different solvents to allow for either doping or inclusion of additional functional groups

for further control over the PL properties. Promising alternative carbon precursors could include cheaper and more abundant biomass or industrial byproducts and dopants such as nitrogen or sulfur other heteroatoms could be used for incorporation of new functional groups in further studies.

2.5 Supporting Information

2.5.1.1 Materials

Sulfuric acid (H_2SO_4, ACS reagent, 95.0-98.0%) was purchased from Sigma-Aldrich. Nitric acid (HNO_3, Certified ACS Plus) was purchased from Fisher Chemical. Potassium hydroxide (KOH, ACS grade) was obtained from the British Drug Houses. Sodium hydroxide (NaOH, ACS reagent) was obtained from EMD Millipore. Nanodiamonds (98+%, 6 nm diameter) powders were obtained from Nanostructured Amorphous Materials Inc. All of these chemicals were used without purification. Dialysis tubing (1kD) was obtained from Spectrum Laboratories, Inc. and allowed to soak in deionized water for 15 minutes prior to use. Deionized water was obtained using a Barnstead™ E-Pure™ Ultrapure Water Purification System.

2.5.1.2 Sample characterization

UV-visible absorption spectra were obtained using a Thermo Scientific Evolution 201 UV-Visible Spectrophotometer. PL spectra were obtained using a Horiba Scientific Fluoromax Plus-C fluorimeter. Emission scans were collected at various excitation wavelengths to test for excitation-dependent emission. PL lifetime measurements were conducted using a DeltaHub™ high throughput time correlated single photon counting (TCSPC) controller and a 333 nm pulsed NanoLED excitation source. Experimental PL

lifetime results were fitted with exponential decay curves using Horiba Scientific Decay Analysis Software. Fourier-transform infrared (FT-IR) spectra were obtained using a Nicolet IS50 FT-IR Spectrometer equipped with a diamond attenuated total reflectance (ATR) plate. X-ray photoelectron spectroscopy (XPS) measurements were obtained using a Thermo Scientific K-Alpha X-ray Photoelectron Spectrometer System. Atomic force microscopy measurements were made using a Park XE-70 Atomic Force Microscope in tapping mode. The analyses of line scans and average particle heights were conducted using the software Gwyddion. Transmission electron microscopy (TEM) images were obtained using a JEOL 2010F Transmission Electron Microscope. Average particle diameters and their lattice spacing were measured using the ImageJ software package.

2.5.2 Optical spectroscopic characterization of precursor nCNOs
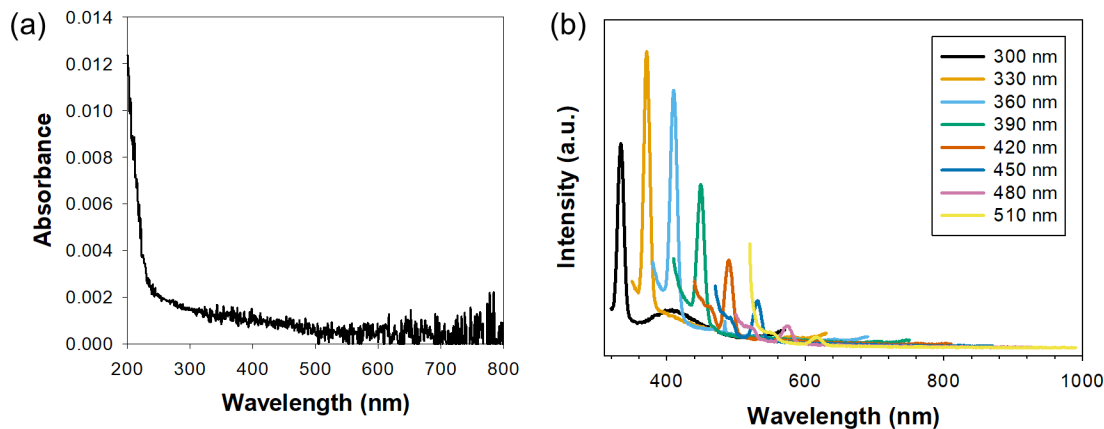
Figure S2.1 UV-Vis absorption (a) and photoluminescence (b) spectra of nCNOs used as a precursor for GQD formation. The nCNOs show continuous absorbance at all wavelengths, indicating their metallic character, and no photoluminescence when excited at various wavelengths. The sharp peaks in the photoluminescence spectrum are from water Raman scattering.

2.5.3   Liquid-phase   laser   ablation   power   dependence   of   LA-GQD

photoluminescence

Samples were prepared in a similar manner to those described in the main text with all of the parameters the same as described except for the laser power. Laser powers of 0.11, 0.57, 0.95, and 1.26 W were used. All samples were filtered with a 450 nm syringe filter and dried in an oven. For analysis, the samples were dissolved in 3 mL of deionized water, and the entire sample was used.
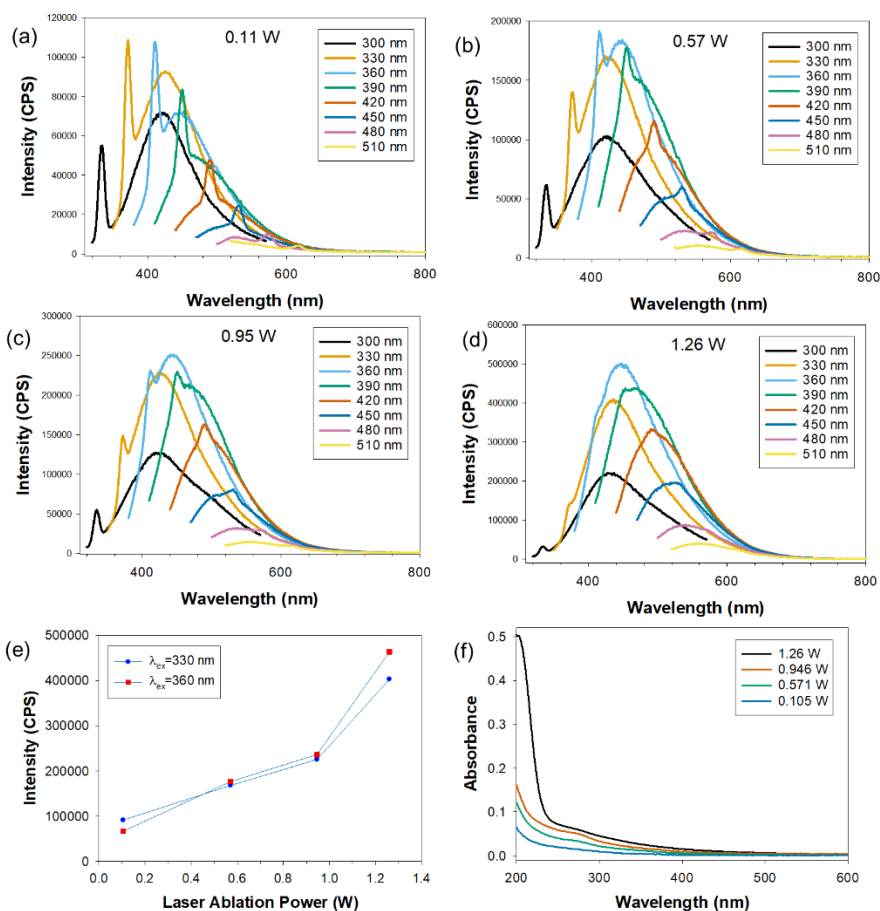
Figure S2.2 Laser ablation power-dependent photoluminescence spectra (a-d), 430 nm emission intensity at 330 and 360 nm excitation (e), and absorbance spectra (f) of the LA-GQDs

2.5.4 Reproducibility of LA-GQDs
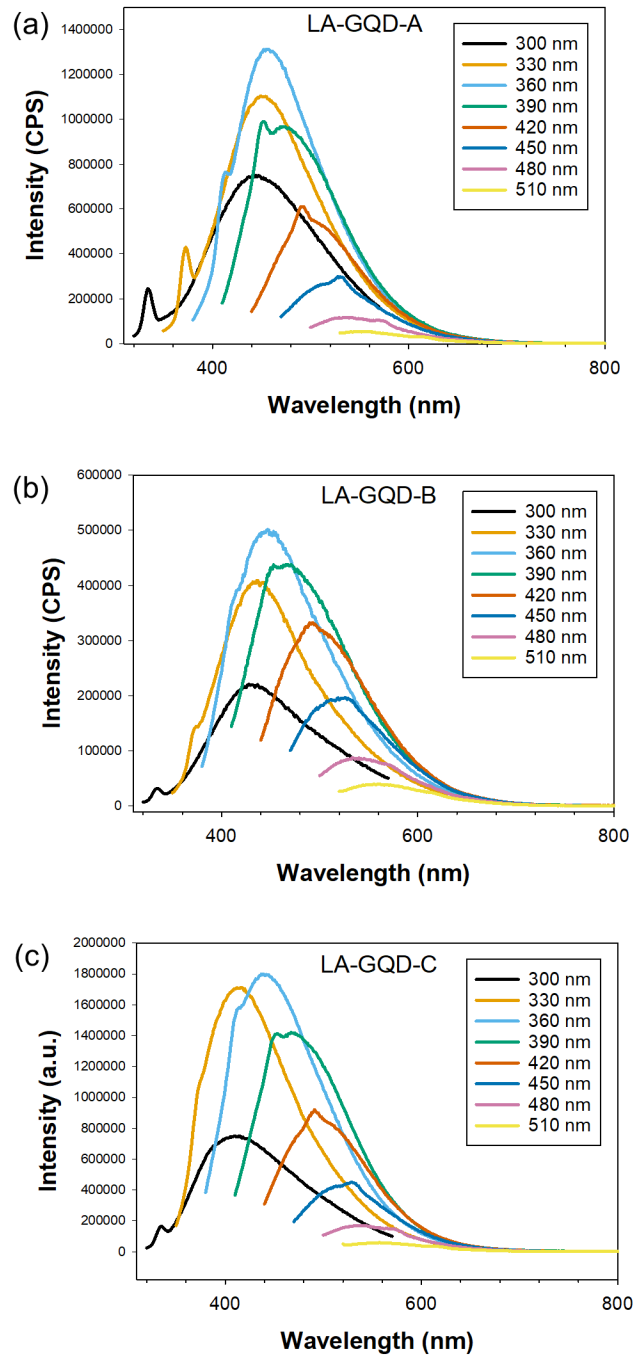
Figure S2.3 PL spectra of three LA-GQD samples produced at 1.30 W. The similar spectra of All three samples indicate the reproducibility of the LA-GQD method.

2.5.5 Time correlated single photon counting (TCSPC) measurements of the CO-and LA-GQDs

Photoluminescence decays were fit to three exponential functions in the form

$$y = A + B_1 e^{-t/\tau_1} + B_2 e^{-t/3} + B_3 e^{-t/\tau_3} \qquad \text{(Equation 2.1)}$$

and the relative contributions were calculated by:

$$\% \tau_n = 100 \times \frac{B_n \tau_n}{B_1 \tau_1 + B_2 \tau_2 + B_3 \tau_3} \qquad \text{(Equation 2.2)}$$

Table S2.1 Exponential fitting parameters for the TCSPC fluorescence lifetime analyses of the CO-GQDs at various emission wavelengths (λ_{em}).

	CO-GQDs		
λ_{em}	430 nm	475 nm	515 nm
A	3.2(8)	1.57(7)	1.46(7)
B1	0.1808(8)	0.1709(8)	0.1418(9)
τ_1 (ns)	0.66(2)	0.63(2)	0.63(2)
B2	0.0249(2)	0.0324(3)	0.0386(3)
τ_2 (ns)	2.31(6)	2.33(5)	2.51(12)
B3	0.00151(2)	0.00309(3)	0.00939(5)
τ_3 (ns)	8.5(2)	8.07(12)	7.90(6)

Table S2.2 Exponential fitting parameters for the TCSPC fluorescence lifetime analyses of the LA-GQDs at various emission wavelengths (λem).

	LA-GQDs		
λ_{em}	430 nm	475 nm	515 nm
A	28.8(2)	68.7(3)	1.03(5)
B_1	1.789(6)	1.530(5)	1.065(11)
τ_1 (ns)	0.093(8)	0.103(8)	0.135(14)
B_2	0.01465(11)	0.0106(2)	0.0101(6)
τ_2 (ns)	3.18(10)	2.56(13)	2.0(3)
B_3	0.00226(2)	0.00355(4)	0.00273(8)
τ_3 (ns)	12.5(2)	8.8(2)	7.9(4)
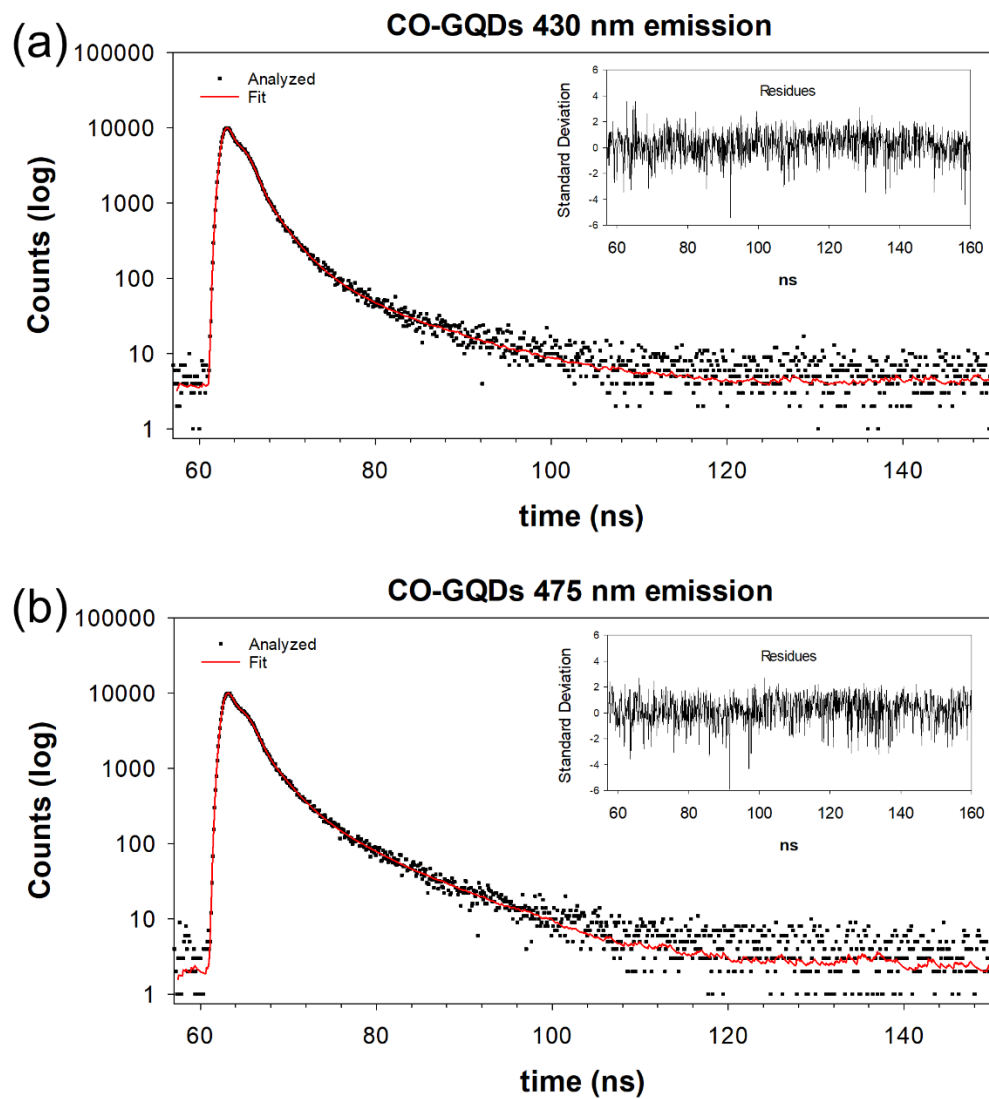
Figure S2.4 TCSPC measurements of the CO-GQDs excited with 333 nm at 430 nm (top) and 475 nm (bottom) emission.
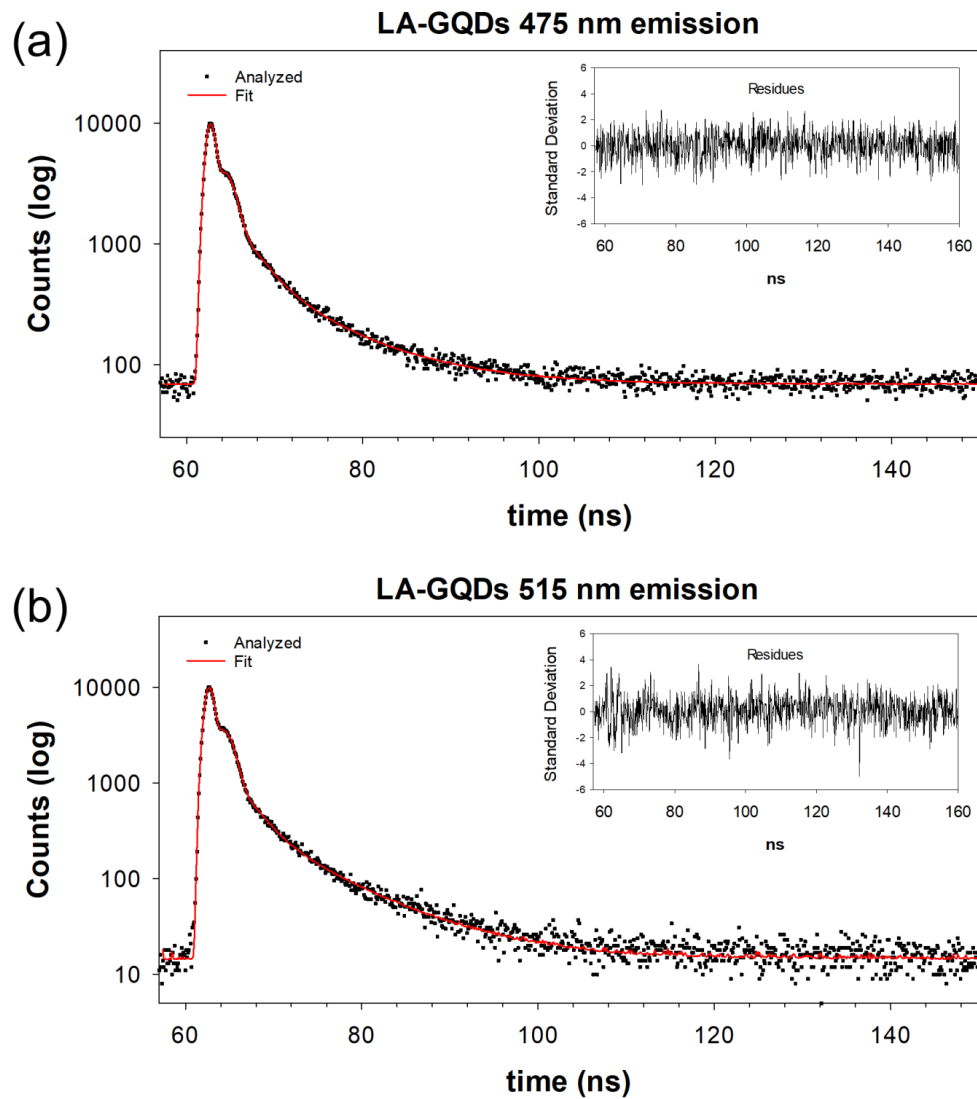
Figure S2.5 TCSPC measurements of the LA-GQDs excited with 333 nm at 475 nm (top) and 515 nm (bottom) emission.

CHAPTER 3. CONTROLLED NITROGEN DOPING OF GRAPHENE QUANTUM DOTS THROUGH LASER ABLATION IN AQUEOUS SOLUTIONS FOR PHOTOLUMINESCENCE AND ELECTROCATALYTIC APPLICATIONS

3.1   Introduction

Graphene quantum dots (GQDs) are promising for many applications in sensing[47, 194], imaging[48], photovoltaics, displays[195], photodynamic therapy[175, 196], and catalysis[13, 197-198]. GQDs have drawn special attention because they can be synthesized from cheap and abundant carbon sources in a large scale, avoid the use of heavy metals, and are light weight as well as biocompatible. [32-33] Many of their applications are driven by their absorbance and photoluminescent (PL) properties with the goal of color control and high PL quantum yield (PLQY). While some previous work has suggested that the size of sp^2 carbon domains, termed intrinsic states, within a GQD could be used to control the absorbance and emission through quantum confinement effects,[63] others have demonstrated that defect states associated with functional groups present on the surface, often termed extrinsic states or molecule-like states, of GQDs, could govern the emission and increase the PLQY.[36, 41] Therefore, by controlling the functional groups present on the GQDs, it is possible to tune the emission to the desired wavelength with improved PLQY.

Various research groups have demonstrated that the chemical state of oxygenated functional groups on GQDs has considerable influence on the emission. For instance, a high degree of chemical oxidation leads to a red shift in emission,[55] while chemical

reduction of oxidized GQDs blue shifts the PL.[191, 199] Nitrogen doping has also been proven to have influence on the emissive properties of GQDs, however, there is still much debate on how various nitrogen functional groups affect the PL. Nitrogen can be present in various forms on GQDs including pyridinic, pyrrolic, amine, amide, graphitic, and nitro groups. One recent report shows a trend of enhanced PL with increased fractions of pyridinic nitrogen, while higher fractions of pyrrolic nitrogen have the opposite effects and favor non-radiative deactivations which decrease the PL.[200] Another shows that increased concentrations of graphitic nitrogen can red shift the PL while also lowering the PLQY due to the introduction of mid-gap states that decrease the HOMO-LUMO gap.[62] This is attributed to the electron donating effect of the graphitic nitrogen into the intrinsic states of GQDs, but other types of nitrogen including pyridinic, pyrrolic, or amino groups did not have a similar effect.[201]

In contrast to the reports arguing for the role of nitrogen as dopants influencing HOMO-LUMO gap, other reports claimed that nitrogen doping could blue shift the emission relative to undoped GQDs and this blue shift is attributed to a change in defect states and surface functional groups.[202] In fact, certain reaction conditions can allow the formation of molecule-like fluorophores that are attached to the GQDs and act as the primary emitting species.[53] For example, blue shifted emission is observed with the introduction of a high fraction of pyridinic nitrogen[49], while the red shifting of emission results from the increased concentration of amine groups.[203] Finally, samples containing higher overall nitrogen content have exhibited higher PLQYs when compared to similarly prepared samples with low nitrogen content.[204] Although the role of dopants in photoluminescence is not fully understood, it is clear that controlling both the ratios of the functional groups and the overall nitrogen content could influence the optical properties of the GQDs.

GQDs have been prepared through many top-down methods, such as chemical exfoliation, hydrothermal synthesis, and electron beam lithography, and by bottom-up

methods, such as stepwise organic synthesis and pyrolysis of carbon precursors.[32-33, 205-206] However, these methods suffer from limitations of multiple steps for preparation, low production yields, use of many hazardous chemicals, long purification processes, and production of non-uniform samples in both size and morphology. Pulsed laser ablation in liquid (LAL) has recently been proven as an alternate single-step method to produce various carbon nanomaterials including GQDs.[154, 178, 180, 185, 207] Potentially, LAL can overcome many of the limitations of other synthetic methods because it uses fewer chemicals, produces higher yields of desired products with few byproducts, and simplifies purification processes. [160, 164-165, 208] Typically, pulsed laser irradiation is incident on a target, generating plasma plumes that expand in liquid. The plasma is subsequently cooled by the surrounding liquid.[161] The presence of dopant molecules in the surrounding liquid allows for the inclusion of various heteroatoms and functional groups[153]. Nitrogen doping in particular has been achieved by laser ablation of carbon precursors with dopants including diethylenetriamine[152], aminotoluene[209] or urea[210]. It has been reported that an increase in laser power can induce a red shift in emission[209] and that nitrogen content can be controlled by varying the dopant concentration in liquid[210]. To the best of our knowledge, however, there are no reports on how the choice of nitrogen precursors in LAL would influence the distribution of nitrogen functional groups and the photoluminescence of the produced GQDs.

The oxygen reduction reaction (ORR) is an important reaction for energy conversion, biological respiration, and industry applications. ORR can occur through 4- and 2-electron processes that result in the production of water and hydrogen peroxide, respectively, in acidic environments[211]. While the 4-electron process is important for the overall efficiency of fuel cells, the 2-electron process is receiving an increased attention due to its efficient production of hydrogen peroxide. Hydrogen peroxide is an important chemical in many industrial applications including medical, environmental, food and beverage, cosmetics, paper making, and chemical synthesis.[212-213] Current methods to

produce hydrogen peroxide, the anthraquinone process or direct synthesis from H_2 and O_2 gas, require multiple steps or involve dangerous reactions.[212] The implementation of the electrocatalytic ORR to produce hydrogen peroxide offers several advantages such as the availability of abundant and clean precursors, few, if any, purification steps, and safer production. The thermodynamic potential for the ORR to form peroxide is 0.76 V vs. reversible hydrogen electrode (RHE).[214] and it is highly desirable to develop an efficient catalyst that is capable of reducing oxygen to hydrogen peroxide through the dominant 2-electron process with low overpotential. Platinum has been shown to catalyze the ORR with low overpotential, however, it is expensive, susceptible to corrosion and CO poisoning, and only active for the 4-electron process without modification.[213] GQDs address some of these limitations as they are produced from cheap and abundant precursors, are lightweight, and their catalytic properties can be tuned by doping with heteroatoms.[49, 198] However, challenges remain to be addressed regarding the efficient scale up of catalysts with enhanced tolerance against surface deactivation by byproducts and impurities.

We report the synthesis of nitrogen-doped GQDs (N-GQDs) through LAL of carbon nano-onions (CNOs) in water along with the characterization of the PL and electrocatalytic properties of the LAL-prepared N-GQDs in comparison with LAL-prepared undoped GQDs. The nitrogen functional groups of the GQDs were tuned by use of different nitrogen containing precursors dissolved in water, including ammonia (N_A-GQDs), ethylenediamine (N_E-GQDs), and pyridine (N_P-GQDs). These N-GQDs were compared to GQDs that were produced in water without any nitrogen precursor molecules (Ox-GQDs). In general, N-GQDs with high fractions of pyridinic groups tended to favor blue emission, while amine groups resulted in a red-shifted emission. These N-GQDs showed high catalytic selectivity for the 2-electron ORR process with the N_P-GQDs having the best performance. LAL demonstrated the single-step, fast, and clean production of the N-GQDs with few byproducts and tunable PL. LAL is a novel synthetic approach to

produce clean electrocatalysts without surface contamination of active sites by using fewer chemicals and a simple synthetic step.

3.2   Experimental

3.2.1   Materials

Ammonia hydroxide (ACS 28.0-30.0% NH_3) was purchased from Alfa Aesar, ethylene diamine ($\geq$99.5%) from Sigma-Aldrich, and pyridine ($\geq$99.0%) from EMD Millipore. Nanodiamond (98+%, 6 nm diameter) powders were purchased from Nanostructured Amorphous Materials Inc. Potassium hydroxide (ACS grade) was purchased from VWR Analytical, a nafion dispersion (D520, alcohol based 1000 equivalent weight at 5 wt. %) from FuelCellStore, acetylene carbon black (100% compressed) from Strem chemicals, Inc., and 20% Pt on Vulcan XC-72 (fuel cell grade) from Premetek Co. All chemicals were used without further purification. Deionized water was obtained from a Barnstead™ E-Pure™ Ultrapure Water Purification System. Iso-Disk™ Filters (PTFE 25-4 25 mm $\times$ 0.45 μm) were purchased from Supelco Inc.

3.2.2   Sample Preparation

3.2.2.1   Preparation of CNOs

CNOs were obtained by thermally annealing detonation nanodiamonds in a graphitization furnace under helium flow at 1650 °C for 1 hour.

3.2.2.2 LAL Synthesis of GQDs

The LAL to produce GQDs was carried out similarly to our previously reported procedure.[207] In a typical setup about 50 mg of CNOs were pressed into a pellet at 10,000 psi and kept under pressure for 15 minutes. The pellet was transferred to a small vial and 3 mL of liquid was added. The vial was placed in a larger secondary container with a quartz lid to prevent evaporation. The reaction container was placed on a rotating stand. The laser beam from a Quanta-Ray Lab 170 Series Nd:YAG Q-switched laser was directed to the pellet using a prism and focused on the pellet surface using a lens. The laser power after passing through the prism and lens was measured to be 80% of the power before the optics. The pulse width was 6-8 ns and the repetition rate was 50 Hz. The pellet was irradiated for one hour with 532 nm light at 100 mJ/pulse (measured before the prism) with the focal spot size of 1.5 mm diameter on the CNO target. After accounting for power loss due to focusing optics, this laser power and spot size results in a laser fluence of 4.5 J/cm^2. DI water was used to prepare Ox-GQDs; 2.5 M solutions of ammonia, ethylenediamine, and pyridine were used to prepare N_A-GQDs, N_E-GQDs, and N_P-GQDs, respectively. Following the laser ablation, the solution was filtered with a 450 nm syringe filter to remove any unconverted CNO pellet and dried overnight in an 80°C oven to remove the liquid. The collected GQDs were redistributed in DI water prior to analysis.

3.2.2.3 Characterization Details

PL spectra were collected with a Horiba Scientific Fluoromax Plus-C fluorometer using 2 nm entrance and exit slits and an integration time of 0.1 s for both excitation and emission scans. PL lifetime measurements were performed using a DeltaHub™ high throughput time correlated single photon counting (TCSPC) controller and a NanoLED-390 pulsed excitation source (excitation wavelength 393 ± 10 nm). TCSPC measurements

were collected at 425 and 465 nm emission with 5 nm bandpass at a repetition rate of 1 MHz over a measurement time of 200 ns. The instrument response function (IRF) was determined by measuring the scattering of the excitation source with a ludox sample. Lifetime fitting was done using Horiba Scientific decay analysis software DAS6. Ultraviolet-visible (UV-Vis) absorption spectra were obtained from a Thermo Scientific Evolution 201 UV-Visible Spectrophotometer at a scan rate of 600 nm/minute and an integration time of 0.1 s. Fourier-transform infrared (FT-IR) spectra were obtained with a Thermo Scientific Nicolet iS50 FT-IR Spectrometer equipped with a diamond attenuated total reflectance (ATR) plate. To collect each spectrum a small (<10 μL) drop of highly concentrated GQD solution was placed on the ATR plate and was dried for 20 minutes in a 40°C oven. Each spectrum was collected using 64 scans and a resolution of 4 cm^{-1}. X-ray photoelectron spectroscopic (XPS) measurements were conducted with a Thermo Scientific K-Alpha X-ray Photoelectron Spectrometer System using an aluminum K$_\alpha$ x-ray source. Samples were drop cast on a silicon wafer. A flood gun was used during analysis. The spot size of x-ray was about 400 μm. XPS survey spectra were obtained with 5 scans, and C1s and N1s XPS high resolutions spectra were obtained with 10 scans. For transmission electron microscopy (TEM), 0.5 mg/mL solutions of GQDs were sonicated for 1 hour, and then 10 μL of the solutions were drop cast on Lacey carbon 300-mesh copper grids. TEM images were obtained using a Thermo Scientific Talos F200X scanning/transmission electron microscope. Particle size analysis was carried out using the open source ImageJ software package. Atomic force microscopy (AFM) measurements were obtained using a Bruker Dimension Icon Scanning Probe Microscope.

3.2.2.4   Electrochemical Measurements

All electrochemical measurements were performed in a 0.1 M KOH solution using a CHI-760D potentiostat with a Ag/AgCl electrode as the reference electrode, a Pt wire

coil as the counter electrode, and a ring disk electrode (4mm glassy carbon disk, 1 mm Pt ring) as the working electrode. For the working electrode, a GQD/carbon black composite was prepared in a 1:2 ratio. A solution containing 1 mg/mL composite with 0.5 wt % nafion binder in water was prepared and sonicated for 1 hour. Following sonication, 10 μL of the solution was drop cast on the glassy carbon disk of the ring-disk electrode and allowed to dry in a 50 °C oven overnight. A N_2 or O_2 saturated environment was produced by bubbling the corresponding gas in the KOH solution for 30 minutes. For a typical sample cyclic voltammetry (CV) scans were collected in both N_2 and O_2 saturated environments. CV scans were collected in the scan range 1.26 to -0.24 V (vs. RHE) at a scan rate of 20 mV/s. Rotating disk electrode (RDE) linear sweep voltammetric (LSV) measurements were collected in an O_2 saturated environment in the scan range 1.26 to -0.24 V (vs. RHE) at a scan rate of 5 mV/s at rotation speeds ranging from 400 to 3200 rpm in increments of 400 rpm. Rotating ring disk electrode (RRDE) measurements were performed in an O_2 saturated environment at 1600 rpm in the scan range 1.26 to -0.24 V (vs. RHE) at a scan rate of 5 mV/s and a constant potential of 0.35 V was applied to the ring to detect any generated hydrogen peroxide. All samples were analyzed in the potential range of 1.26 to -0.24 V except for the Pt/C electrode which was analyzed in the potential range 0.3 to 0.06 V.

3.3   Results

Figure 3.1a presents a schematic representation of a typical laser ablation setup. In general, a 532 nm pulsed nanosecond laser beam is directed through a prism and focused onto the pellet using a lens. Once the laser interacts with the CNO target (Figure 3.1b), a dense plasma of fragments from the precursor and carbon atoms is formed and then expands. Subsequently, the plasma is cooled by the surrounding liquid.[161] As the plasma cools, it nucleates and reacts with the water, and nitrogen containing solutes are dissolved

in water, allowing for incorporation of various functional groups such as hydroxyl, carbonyl, and carboxyl oxygen groups and pyridinic, amine, pyrrolic, and graphitic nitrogen groups (Figure 3.1c). By focusing the laser pulse on the CNO pellet, further laser pulses have minimal interactions with the formed GQDs that are in the solutions. The GQDs also have negligent absorbance at 532 nm which further minimizes interactions of the GQDs with the laser pulses. TEM images of the Ox-GQDs and N-GQDs are presented in Figure 3.2 and histograms of their particle size analysis are reported in Figure S3.1. The Ox-GQDs showed the presence of isolated particles (Figure 3.2a, inset), and most particles formed agglomerates due to their hydrophobicity. However, the small particles on the nanoscale were visible within the agglomerates. The Ox-GQDs have a much smaller particle size with an average diameter of 4.0(9) nm, while the N doped samples (Figure 3.2b-d) have particle diameters of 14(4) nm, 14(3) nm, and 15(4) nm for N_A-GQDs, N_E-GQDs, and N_P-GQDs, respectively. All four samples have similar size distributions with relative standard deviations of 20-25%, indicating that the choice of dopant does not greatly affect the size uniformity. AFM measurements are detailed in Figure S3.2 and show particle heights of 2.2(8) nm for Ox-GQDs, 6(2) nm for N_A-GQDs, 5.1(15) nm for N_E-GQDs, and 3.7(13) nm for N_P-GQDs indicating that the lateral dimensions for all GQD samples are larger than their heights, and that Ox-GQDs are in general smaller than the N-GQDs. The production yield was also considered by comparing the mass of produced GQDs to the mass of consumed CNOs. In a typical LAL experiment 53(7)% of the consumed CNOs are converted to GQDs while the remaining consumed pellet was filtered out of the solution. Future implementation of methods to recover and reuse the large filtered fragments of CNOs can used to further improve the production yield.
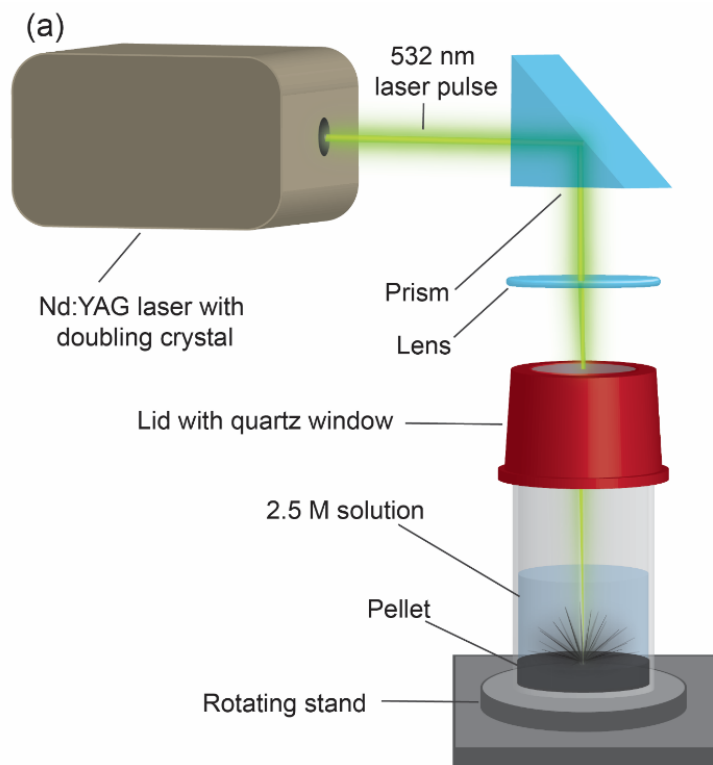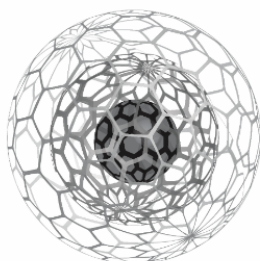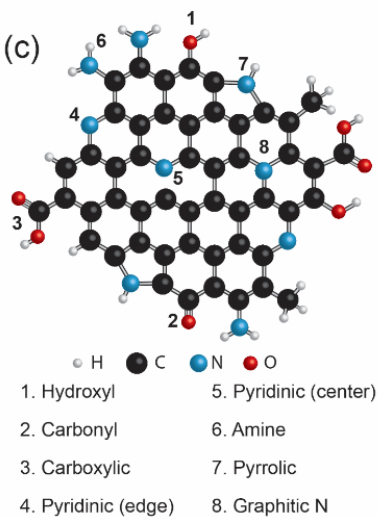
Figure 3.1 Schematic representation of a typical laser ablation setup (a). Upon laser irradiation, the precursor CNOs (b) are converted into graphene quantum dots (c).
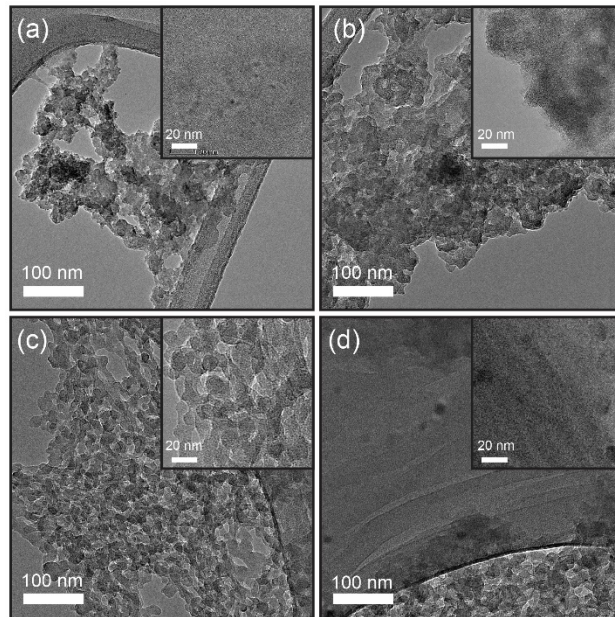
Figure 3.2 TEM images of the Ox-GQDs (a), and N-GQDs produced with ammonia (b), ethylenediamine (c) and pyridine (d). The scale bar for the larger images is 100 nm, and the scale bar for the insets is 20 nm.

The choice of the nitrogen precursor solutes had an influence on the functional groups formed on the nitrogen doped GQDs. The FT-IR spectrum of each sample is presented in Figure 3.3. The spectrum of the Ox-GQDs shows a broad peak with the maximum around 3400 cm^{-1} and several narrow ones in the region below 2000 cm^{-1}. The 3400 cm^{-1} peak is attributed to the hydrogen-bonded O-H stretching of hydroxyl functional groups, the 1700 cm^{-1} shoulder to the C=O stretching from carboxylic groups or ketones, the 1600 cm^{-1} peak to the aromatic ring stretch of the sp^2 hybridized carbon domains within the GQDs, the 1375 cm^{-1} peak to a CH$_3$ bend, and the 1150 cm^{-1} one to a sp^3 bonded C-O stretch. The spectra of the N$_A$-GQDs have a similar absorption profile to that of the Ox-GQDs. However, the peak in the O-H stretching region is much broader and shifted towards 3300 cm^{-1}, suggesting the presence of an amine N-H stretch. A new, strong peak appears at 1350 cm^{-1} due to an aryl C-N stretch[190], and the sp^3 bonded C-O peak at 1150 cm^{-1} is split into two due to the additional presence of a sp^3 bonded C-N stretch. For both N$_E$-GQDs and N$_P$-GQDs, the amine N-H stretch at 3250 cm^{-1} is stronger relative to the O-

H stretching which is present as a shoulder, and the C-H stretching associated with the sp^2 and sp^3 carbons is more sharply defined at 3050 cm^{-1} and 2950 cm^{-1}, respectively. Similar to the N$_A$-GQDs, the N$_E$-GQDs and N$_P$-GQDs show the N-H stretch, aromatic ring stretching, aryl C-N stretching, and sp^3 bonded C-N and C-O stretching in the 700 - 1700 cm^{-1} range[190], however, the relative intensities are different for each sample. For the N$_E$-GQDs and N$_P$-GQDs the sp^3 bonded C-N and C-O stretching peaks become less resolved and much weaker, and the aryl C-N stretch is also suppressed. Moreover, the spectra of these two nitrogen-doped GQDs show an additional sharp, strong peak at 1670 cm^{-1} which can be assigned to the N-H bend, and the spectrum of the N$_p$-GQDs exhibits a large intensity increase of the aromatic ring stretch peak at 1600 cm^{-1} compared to those of the other GQDs.

The functional groups of the LAL-prepared GQDs were further investigated by XPS. The XPS survey spectra are shown in Figure S3.3, and the resultant elemental ratios are presented in Table S3.2. The Ox-GQDs consist of mainly carbon (64.8%) and oxygen (33.5%). The small amount of nitrogen present is likely due to adsorbed nitrogen from the atmosphere. Among the three types of the N-GQDs, the nitrogen content increases from 4.8% in the N$_A$-GQDs, to 10.2% in the N$_p$-GQDs, and to 23.% in the N$_E$-GQDs. The highest content of nitrogen in the N$_E$-GQDs is consistent with the fact that each ethylenediamine molecule has two nitrogen atoms and with a previous report that primary amines allow for high degrees of nitrogen doping.[204] While all three nitrogen doped samples contain oxygen, the N$_A$-GQDs contain the largest fraction of oxygen (55.9%), and the N$_p$-GQDs have the largest fraction of carbon (68.2%) out of all of the samples. Figure 3.4 presents the XPS C1s high resolution spectra for all four samples, and their binding energies and relative contributions are summarized in Table S3.3. The deconvoluted spectra show the presence of sp^2- and sp^3-C in the carbon domain and C-N, hydroxyl C-O, carbonyl C=O, and carboxylic O-C=O bonded carbon at 284.5, 285.3, 286.1, 287.0, 288.0, and 289.0 eV, respectively.[215-217] The Ox-GQDs are the only sample where the relative amount of the sp^2

bonded carbons is higher than the sp^3 bonded carbons. For the Ox-GQDs, hydroxyl groups are the major functional group, with carbonyl and carboxylic groups also present. For the N-doped GQDs, the C-N bonded carbon is dominant over all oxygen containing functional groups, and the hydroxyl groups have a higher fraction than the carbonyl and carboxylic groups. The N$_P$-GQDs have the highest fraction of the sp^2 carbons (26.2%) out of all of the N-GQDs which is attributed to the pyridine nitrogen source maintaining its sp^2 nature during doping.
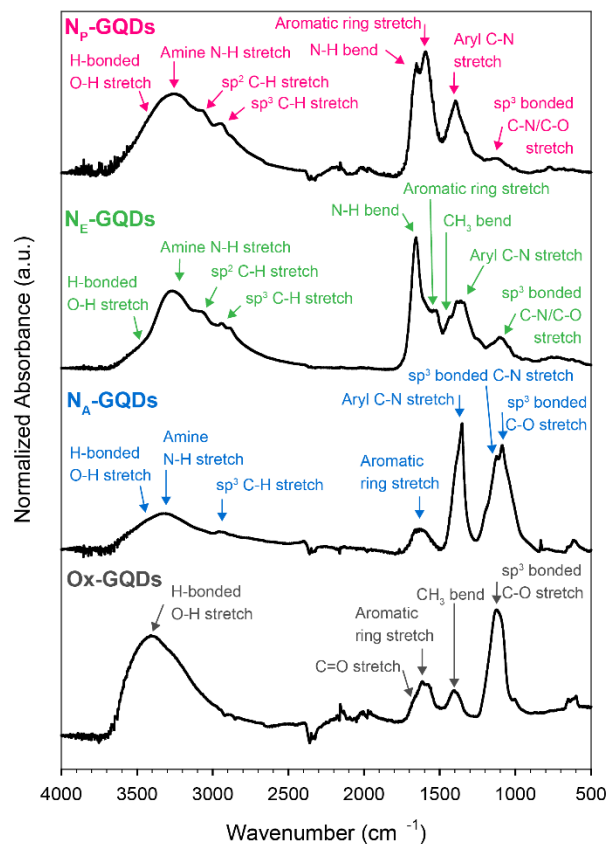
Figure 3.3 FT-IR spectra for the Ox-GQDs and N-GQDs produced with ammonia, ethylenediamine and pyridine.

The various nature of nitrogen doping of the N-GQDs was investigated by analyzing the N1s XPS spectra. The N1s XPS raw and deconvoluted spectra are presented in Figure 5a-c, and their total nitrogen content is presented in Figure 3.5d. The binding

energies and relative contributions are summarized in Table S3.4. All three types of the N-GQDs have a mixture of pyridinic, amine, pyrrolic, and graphitic nitrogen at 398.8, 399.7, 400.7, and 401.8 eV, respectively.[215, 218-219] Although specific types of nitrogen precursors were used for the doping, nitrogen is converted to various chemical states after incorporation. For the N_A-GQDs and N_E-GQDs, the dominant functional groups are amine and pyrrolic nitrogen with the N_A-GQDs having considerably less total nitrogen functional groups than the N_E-GQDs. The N_E-GQDs have the largest fraction of amine functional groups among the three N-GQDs which accounts for 49.3% of the nitrogen containing functional groups. Overall, nitrogen precursor solutes were found to influence both the total amount of incorporated nitrogen and the distribution of functional groups. For example, the N_E-GQDs retain the largest amount of amines, although a fraction of amines is converted to pyridinic, pyrrolic and graphitic nitrogen. While the N_E-GQDs and N_P-GQDs both contain similar amounts of pyridinic and graphitic nitrogen, these functional groups contribute to a higher percentage of the N_P-GQDs, with the pyridinic group accounting for 31.3% and the graphitic group accounting 13.0% of the total nitrogen sites. These results give further insight into the GQD formation mechanism. During LAL, the dopant molecules are recruited and chemically bonded to the resultant GQDs rather than just physisorption. This is supported by the presence of various nitrogen functional groups in each N-GQD sample rather than observation of only those the functional groups present in the corresponding dopant molecule.
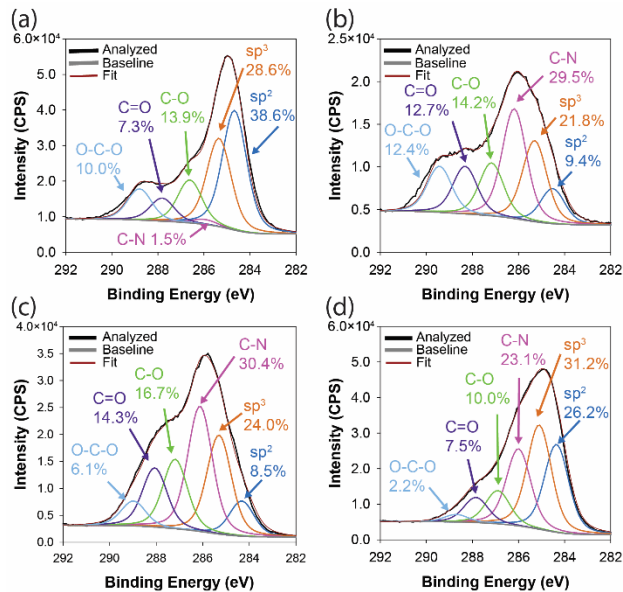
Figure 3.4 High resolution C1s XPS spectra for the Ox-GQDs (a) and N-GQDs produced with ammonia (b), ethylenediamine (c) and pyridine (d).
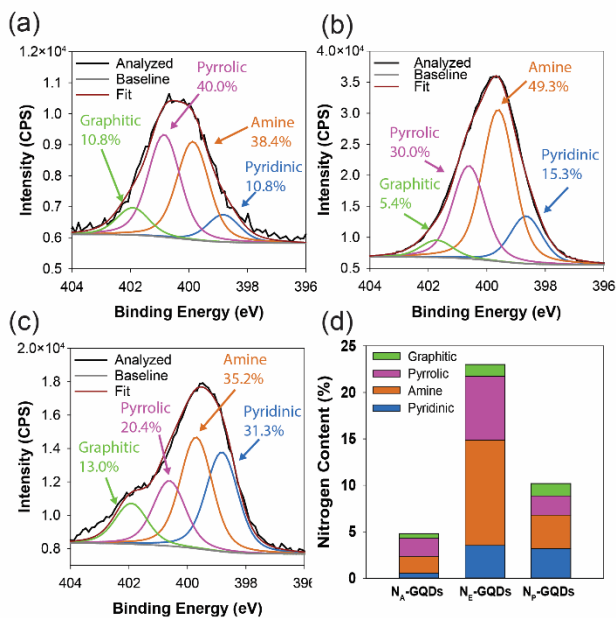
Figure 3.5 High resolution N1s XPS spectra of the N-GQDs produced with ammonia (a), ethylenediamine (b) and pyridine (c). The content of each nitrogen chemical state is summarized in (d).

Figure 3.6a presents the UV-Vis absorption spectra of the various GQD samples. The Y axis of the absorption spectra is extinction mass coefficient (ε, cm^{2}g^{-1}). For GQDs, the short wavelength absorption (< 250 nm) is typically attributed to π-π^* transitions of the sp^2 hybridized carbon backbone and the longer wavelength absorptions (>250 nm) are due to n-π^* transitions of functional groups present.[220] All samples exhibit strong absorbance in the deep UV (200-210 nm) region from the π-π^* transitions of the carbon backbone. None of the samples show any absorption past 450 nm which indicates that all absorbance transitions occur in the UV - blue range. As previously mentioned, this also results in minimal interactions of the GQDs with the 532 nm laser pulses during LAL. The Ox-GQDs have shoulders at 265 and 350 nm which can be attributed to the n-π^* transitions of various oxygenated functional groups. Similarly, the N$_A$-GQDs have a peak at 280 nm, however, it is more strongly defined. The N$_E$-GQDs have the weakest absorbance with only weakly absorbing shoulders observed at 270 and 350 nm. The N$_P$-GQDs have a shoulder occurring at 260 nm. All of the N-GQDs are only weakly absorbing in the 350-450 nm range without any well-defined features that reflect the wide distributions of surface functional groups. Figure S3.4 shows the absorbance and PL spectra of the precursor CNOs indicating a major change in optical properties following LAL.

The PL excitation (PLE) spectra for the various GQD samples are shown in Figure 3.6b. Each spectrum was collected at the emission wavelength where maximal emission occurs for each individual sample (445 , 465 , 435 , and 415 nm for the Ox-GQDs, N$_A$-GQDs, N$_E$-GQDs, and N$_P$-GQDs, respectively). For each GQD, the profile of the PLE spectrum is quite different from its absorbance spectrum, due to the different PLQYs of the bands. For the Ox-GQDs, the strongest emission occurs with 310 nm excitation and with decreasing emission at longer wavelengths. The slight shoulder at 385 nm is due to Raman scattering of the water solvent. The N$_A$-GQDs show a gradual increase in emission with increasing excitation wavelength with a slight shoulder apparent at 325 nm and a well-defined peak at 375 nm. The N$_A$-GQDs are the only sample that has its strongest emission

at a longer wavelength excitation (380 nm). The N_E-GQDs show peak emission with 330 nm excitation and decreasing emission at longer wavelengths and a slight shoulder at 380 nm. The N_P-GQDs have the shortest wavelength excitation with a peak at 310 nm and a shoulder around 330 nm. The full excitation spectra for each sample is shown in Figure S3.5. For the N_A-GQDs, two peaks at 325 and 375 nm are apparent at all emission wavelengths with the relative intensities of each peak changing with emission wavelength. At shorter emission wavelengths the peak at an excitation of 325 nm is stronger and as the emission wavelength increases the peak excitation shifts towards favoring 375 nm. The N_E-GQDs, on the other hand, show a similar excitation profile, but it shifts towards longer excitation wavelengths with increasing emission wavelength.

The PL properties were further examined by considering the emission spectra of each sample (Figure 3.6c-f). The Ox-GQDs have a peak emission occurring at 445 nm with 330 nm excitation. The sharp, excitation dependent shoulders on the short wavelength side of each PL curve are also due to the Raman scattering of the water solvent. The N_A-GQDs have peak emission occurring at 465 nm with 390 nm excitation. At 330 nm excitation, a shoulder is also observed at 400 nm emission but is suppressed at excitation wavelengths longer than 360 nm. The N_E-GQDs have the strongest emission occurring at 435 nm with 360 nm excitation, and the N_P-GQDs peak emission occurs at 415 nm with 330-360 nm excitation. It is observed that all four GQDs exhibit some combination of both excitation independent and excitation dependent emission. For the Ox-, N_E-, and N_p-GQDs, the excitation independent emission is observed at shorter wavelengths and excitation dependent emission is observed at longer excitation wavelength. For the N_A-GQDs, the excitation dependence is only weakly observed while excitation independent emission is strongly observed at 465 nm emission. The excitation dependent emission is attributed to non-uniform sp^2 carbon domains within a sample favoring different emissions based on the quantum confinement effect. These emissions are weaker than the excitation independent emissions that are attributed to emission from functional groups.[36-37]
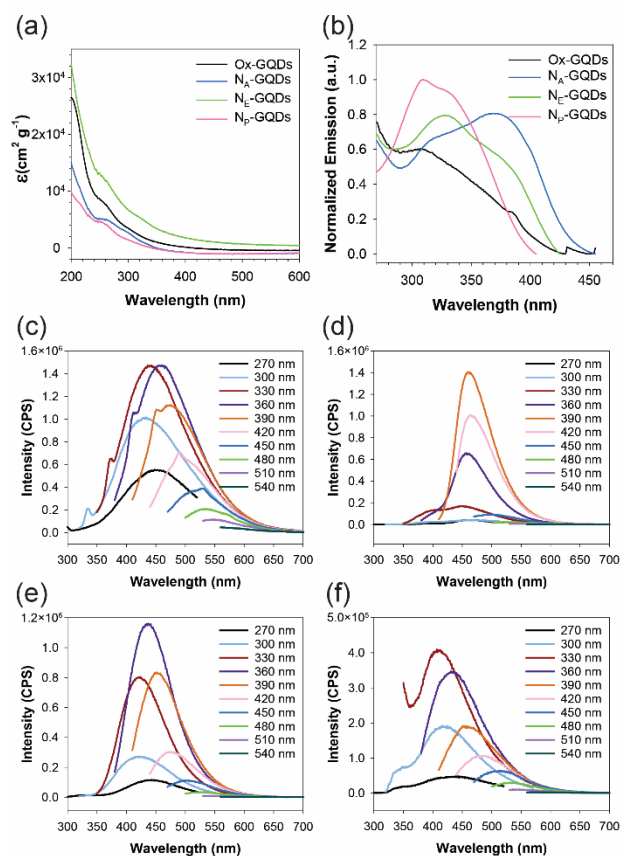
Figure 3.6 Absorbance spectra of the Ox-GQDs and N-GQDs produced with various precursors (a), PLE spectra collected from emissions at 445 nm for the Ox-GQDs, at 465 nm for the NA-GQDs, at 435 nm for the NE-GQDs, and at 415 nm for the NP-GQDs (b), and PL emission spectra at various excitation wavelengths for the Ox-GQDs (c), and the N-GQDs produced with ammonia (d), ethylenediamine (e) and pyridine (f).

The emissive properties can be understood by considering the functional groups present in the samples. The Ox-GQDs have the weakest emission out of all the samples, which is expected since they lack nitrogen doping that is expected to enhance the emission. The peak emission at 445 nm is attributed to emission from the large fraction of hydroxyl groups as carboxyl groups are expected to contribute to longer wavelength emissions.[199] It has been reported that amine and pyrrolic nitrogen red shifts emission while edge pyridinic nitrogen blue shifts the emission.[221] The N_A-GQDs have amine nitrogen as their primary

nitrogen functional group, and we assign the strong excitation independent emission at 465 nm to be from these amine groups. The N_E-GQDs have a high nitrogen content; while they favor amine and pyrrolic nitrogen, they still have a high number of pyridinic and graphitic nitrogen sites. This results in strong excitation dependent emission from the various types of nitrogen doping. The bluer emission occurs due to the pyridinic nitrogen, and redder emission is mainly from the amine nitrogen. The N_P-GQDs have the bluest emission among all GQDs, attributable to the largest fraction of the pyridinic nitrogen. They also have the largest fraction of the graphitic nitrogen, and while it is reported that the graphitic nitrogen can red shift emission[62], we expect this to have minimal effect due to the large fraction of the sp^3 carbon causing disordered structures and small sp^2 carbon domain sizes. Based on these observations, we can assign the PLE bands observed in the N-GQDs. The N_P-GQDs have the strongest emission with shorter wavelength excitation (310 nm) which is mainly influenced by transitions related to the pyridinic nitrogen. The N_A-GQDs exhibit the strongest emission at longer wavelength excitation (380 nm) due to mainly amine nitrogen groups. N_E-GQDs have a large number of both types of nitrogen and demonstrate strong bands at both wavelengths.

Fluorescence intensity decay measurements were performed at 390 nm excitation and measured at 425 (Figure 3.7a) and 465 nm emission (Figure 3.7b.) The fluorescence intensity decay profile tracks the deactivation kinetics of electrons from an excited state to the ground state via radiative and non-radiative paths. The decay curves were fit to three exponentials as is common with previously reported measurements.[55] The lifetimes and their overall contributions are summarized in Table 3.1, and the complete fit parameters are shown in Tables S3.4-S3.5. All decays had a fast component (τ_1) from the radiative recombination of the intrinsic states[36] and two slower components (τ_2 and τ_3) that are attributed to the surface functional groups[55]
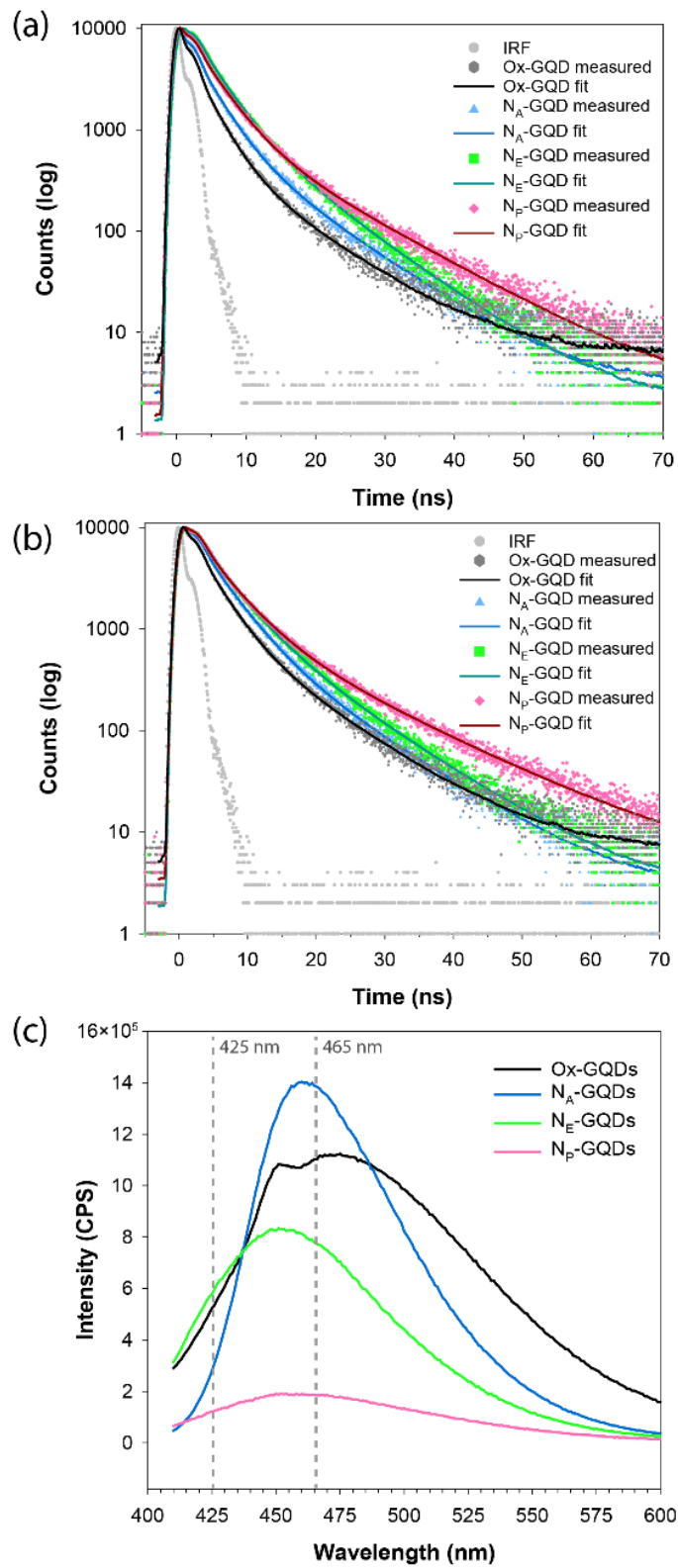
Figure 3.7 TCSPC of the Ox-GQDs and N-GQDs, and the corresponding IRF at 425 nm
(a) and 465 nm (b) emission. PL spectra at 393 nm excitation (c)

Table 3.1 Time correlated single photon counting lifetimes and relative contributions of the Ox-GQDs and N-GQDs at 425 nm and 465 nm emission.

		Ox-GQDs		N_A-GQDs		N_E-GQDs		N_P-GQDs	
		Lifetime (ns)	Contribution (%)	Lifetime (ns)	Contribution (%)	Lifetime (ns)	Contribution (%)	Lifetime (ns)	Contribution (%)
λ_{em} = 425 nm	τ_1	0.346(10)	39.0(8)	0.355(12)	28.6(7)	0.92(5)	16.5(8)	0.56(3)	19.4(8)
	τ_2	2.71(5)	44.0(7)	3.02(5)	48.9(6)	3.52(4)	56.5(6)	3.56(3)	55.0(6)
	τ_3	9.13(8)	17.0(3)	9.17(6)	22.5(3)	8.86(5)	27.0(3)	11.43(5)	25.6(3)
λ_{em} = 465 nm	τ_1	0.60(2)	24.0(5)	0.80(3)	20.0(6)	1.09(2)	18.2(4)	1.15(2)	19.2(4)
	τ_2	3.24(6)	51.7(6)	3.92(4)	57.3(4)	4.17(11)	53.2(7)	4.44(9)	53.5(5)
	τ_3	9.58(7)	24.3(3)	10.01(7)	22.7(3)	9.91(6)	28.6(4)	13.31(7)	27.3(3)

We previously reported that for GQDs containing a mixture of hydroxyl and carboxylic groups the intrinsic state showed the fluorescence decay with the fast τ_1 component and was weakly emitting, while the hydroxyl groups were responsible for the intermediate τ_2 component and carboxylic groups were responsible for the longest τ_3 component, and both functional groups were strongly emitting.[207] Other reports also suggest that the intrinsic states have low PLQYs with a fast non-radiative deactivation component.[36] It also has been suggested that functional groups with a higher degree of oxidation or polarity will have a longer lifetime component that also increases with increasing emission wavelength.[14]

Here, we observe a similar trend for the current GQD samples. The τ_1 component is slower at 465 nm emission than at 425 nm emission. Since the τ_1 is related to the intrinsic states from the sp^2 carbon domains, the shift to longer wavelengths relates to the emission from larger carbon domains that have a smaller energy gap. The relative contributions also change due to varying amounts of the different sized sp^2 carbon domains. Out of the three different decays, the τ_1 is the least similar when comparing the various samples, which can be explained by the large amount of the disorder and sp^3 carbon within the samples. With 390 nm excitation, the emission intensity for the Ox-GQDs is significantly higher at 465 nm than 425 nm (Fig 7c.). The relative contributions of the τ_2 and τ_3 components also increase at 465 nm emission, which further supports that these decays are due to components with a strong radiative nature . Since the Ox-GQDs only have oxygen containing functional groups, we assign the τ_2 to hydroxyl groups and the τ_3 to more oxidized and polar carboxylic groups similar to previous work.[14, 207] Since hydroxyl groups account for the highest percentage of oxygen containing functional groups on the Ox-GQDs, it makes sense that the τ_2 component will have the highest relative contribution.

The N$_A$-GQDs also show a significant increase in emission intensity with the shift from 425 to 465 nm emission. While τ_2 shows a higher relative contribution at 465 nm, the τ_3 component does not show any significant difference between the two emissions. The

dominant functional groups on the N_A-GQDs are hydroxyl and amine groups so we expect them to be the major contributing factors in the τ_2 decay. While the intrinsic τ_1 component is present at 465 nm emission, it is expected to have a low PLQY and minimally contribute to the emission.[207] Therefore, the strong emission observed at 465 nm is assigned to surface functional groups from the τ_2 component. Both the N_E-GQDs and N_P-GQDs show only slight increase in emission intensity at 465 nm, and their τ_2 and τ_3 components have much less difference at the two emission wavelengths. For both samples, the τ_2 component decreases slightly, while the τ_3 component increases slightly. The emission peaks at 390 nm excitation are also blue shifted relative to the Ox-GQDs and N_A-GQDs. As previously mentioned, the N_E-GQDs have a high nitrogen content which contributes to excitation dependent emission and a high quantity of different types of emitting functional groups. Since the τ_2 component is attributed to amine functional groups, we expect τ_3 to be strongly influenced by the more polar, pyridinic nitrogen sites. Finally, it is noted that the τ_3 component for the N_P-GQDs is noticeably slower when compared to the other samples. The N_P-GQDs have the highest overall percentage of pyridinic nitrogen and the bluest shifted emission out of all of the samples. If the τ_3 component is influenced by the pyridinic nitrogen groups, it makes sense that the N_P-GQDs would have such a long lifetime at 390 nm excitation because the radiative component of deactivations is quite weak as shown by the weak emission at 390 nm excitation in the PLE spectra regardless of the emission wavelength (Figure S3.5d). The emission at 465 nm could be due to an energy transfer process because it would take longer for the higher energy states of the N_P-GQDs to decay to longer wavelengths before emitting. Since the N_P-GQDs are only weakly emitting with 390 nm excitation, we expect τ_3 for this sample to have a strong non-radiative component and a weak radiative component.

The PLQY of the GQDs was measured relative to a quinine sulfate standard (Figures S3.6-S3.8). The Ox-GQDs had a PLQY of 0.81(7)%. The addition of nitrogen resulted in an increase of PLQY with N_A-, N_E-, and N_P-GQDs having PLQYs of 3.8(5)%,

8.6(4)%, and 4.6(3)%, respectively. Total nitrogen content clearly influenced the PLQY as N_E-GQDs had both the highest nitrogen content and the highest PLQY while N_A-GQDs had both the lowest nitrogen content and PLQY of the three N-GQDs. The photostability of the GQDs was considered by measuring their emission at continuous excitation for one hour at their maximum excitation and emission wavelengths (Figure S3.9). All four samples showed a decrease in intensity of less than 7% indicating the samples are stable in water under continuous excitation and suitable for applications that use similar conditions intensity excitation. Finally, the effects additional purification had on the spectra was considered. Samples were dialyzed for one week in a 1000 Da molecular weight cut off membrane to remove any small side products that could have formed during LAL. Spectra were collected both before and after dialysis (Figure S3.10a-h) and showed very similar PL profiles which indicates that the emitting species is retained in the dialysis membrane. The outer solution was also analyzed (Figure S3.10i-l) and only showed minimal emission. These results support LAL as a method to produce PL materials in a way that is fast and requires minimal purification.

To test catalytic performance of the N-GQDs for the ORR reaction, CV curves were recorded in either N_2 saturated or O_2 saturated electrolyte. The performance of the N-GQDs was compared to those of Pt/C and carbon black support in the absence of the GQDs (Figure S3.11). Each CV curve was corrected for IR (current times resistance) to compensate for a large resistance that is due to the large content of nafion (Table S3.12). All samples showed featureless CV curves in the N_2 saturated environment, indicating that no faradaic reactions are taking place. For all samples in an O_2 saturated environment, as the potential was swept towards a more negative voltage, a clear increase in reduction current density is apparent due to the occurrence of the ORR reaction.
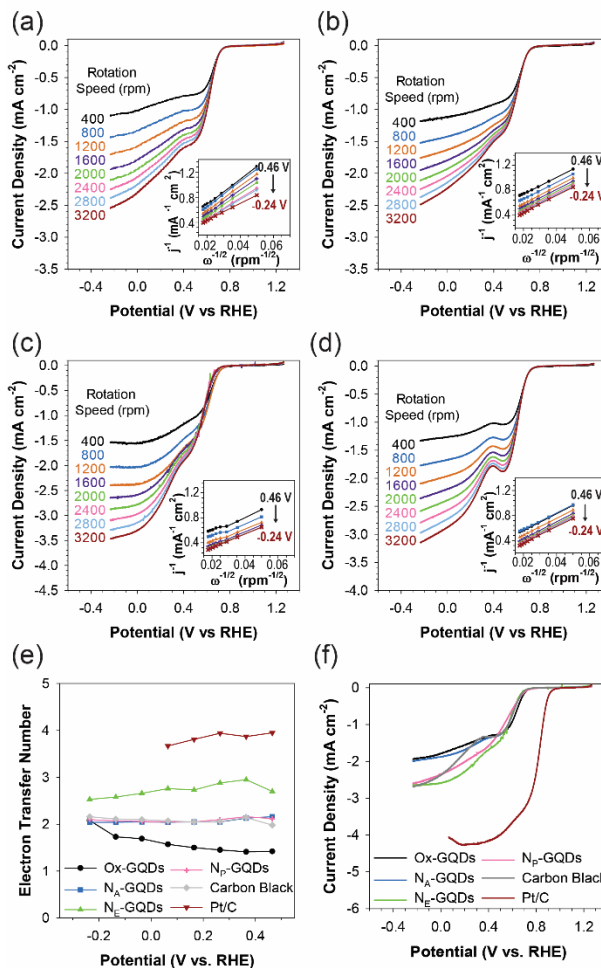
Figure 3.8 RDE LSV scans for the Ox-GQDs (a), Na-GQDs (b), Ne-GQDs (c), and Np-GQDs (d) and their derived KL plots (insets). For the insets the various potentials are represented by black circles at -0.5 V, blue squares at -0.6 V, orange triangles at -0.7 V, purple crosses at -0.8 V, green hexes at -0.9 V, pink diamonds at -1.0 V, light blue inverted triangles at -1.1 V, and red x's at -1.2 V. Electron transfer numbers (e), and overlaid LSV scans of each sample collected at 1600 rpm (f).

RDE measurements and their Koutecky-Levich plots are reported in Figure 3.8a-d for the GQD samples and in Figure S3.12 for the reference samples. A plot of the calculated electron transfer numbers is shown in Figure 3.8e, and an overlay of RDE LSV scans for each sample at 1600 rpm is shown in Figure 3.8f. RDE measurements were performed at rotation speeds ranging from 400 to 3200 rpm, and potentials ranging from 0.46 to -0.24 V (vs. RHE) were analyzed to determine electron transfer numbers. Details of the Koutecky-

Levich equation are included in the supporting information. For Pt/C the electron transfer number is close to 4 at low potentials but decreases slightly at higher potentials indicating slight peroxide formation. The Ox-GQDs show an electron transfer number slightly lower than 2 which could indicate a mix of a 2-electron pathway to form peroxide and 1-electron pathway to form superoxide.[222] The N_E-GQDs have an electron transfer number close to 3 at low applied potentials that approaches 2 as the potential becomes more negative. The N_A-GQDs, N_P-GQDs, and carbon black all show an electron transfer number that favors a 2-electron process at all potentials, indicating good selectivity for peroxide formation. All LSV scans were swept from 1.26 to -0.24 V (vs. RHE). Compared to the onset potential of carbon black (0.70 V), all GQD samples showed positively shifted onset potentials (N_A-GQDs: 0.72 V, N_E-GQDs: 0.74 V, and N_P-GQDs: 0.75 V). It has been reported that carbon atoms neighboring pyridinic sites have the best catalytic activity[223], so it is not surprising that the N_E-GQDs and N_P-GQDs show the lowest onset potentials as they contain a comparable number of pyridinic and graphitic sites. Moreover, the N_E-GQDs and N_P-GQDs have shown the largest ORR current densities among the GQD samples, exceeding the N_A-GQDs, Ox-GQDs, and carbon black (Figure 3.8f). The Pt/C reference sample had the lowest onset potential at 0.90 V and the highest current density out of all of the samples, however, it should be noted that this reference is catalyzing a 4-electron primarily over the 2-electron process which was favored by all of the carbon samples. It is also apparent that for most RDE and RRDE measurements two separate increases in current density are observed. This is especially prominent in the N_P-GQDs. We attribute the feature of two increasing currents to the disturbance of mass transfer due to the porous nature of the samples during the rotations of electrodes, not to the presence of multiple catalytic sites.
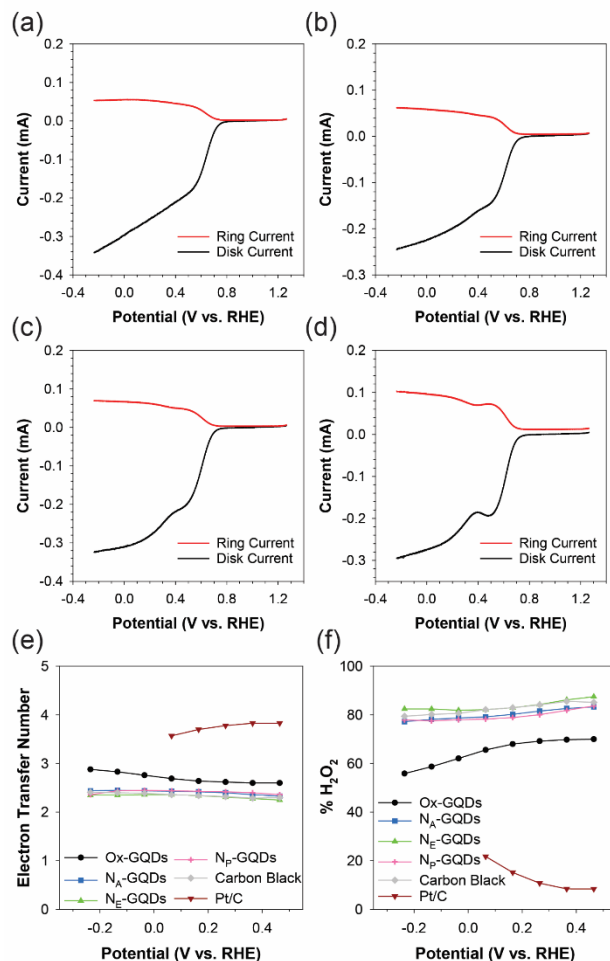
Figure 3.9 RRDE LSV scans for the Ox-GQDs (a), Na-GQDs (b), Ne-GQDs (c), and Np-GQDs (d). Electron transfer numbers (e) and % H2O2 formation (f) for the Ox-GQDs (black circles), Na-GQDs (blue squares), Ne-GQDs (green triangles), carbon black only (grey diamonds), and Pt/C (red inverted triangles).

RRDE measurements are reported in Figure 3.9a-d for the GQD samples and Figure S3.13 for the reference samples. In Figure 3.9a-d, the disk current is from ORR occurring at each GQD working electrode while the ring current is from oxidation of hydrogen peroxide produced from ORR. From the RRDE results, electron transfer numbers are determined for each GQD. The plots of the determined electron transfer number and the percentage of hydrogen peroxide produced are shown in Figure 3.9e-f. Similar to the RDE measurements, the RRDE shows that all three N-GQD samples have an electron transfer number close to 2 consistently across all applied potentials. Their percent hydrogen peroxide production is close to 80% which indicates good selectivity towards the 2-electron

process. The Ox-GQDs have much lower selectivity at 60% which decreases with increased applied potential. It should be noted that the electron transfer numbers for the Ox-GQDs calculated by RRDE are significantly different from the RDE measurements. For the Ox-GQDs, not only ORR but also the reduction of oxygen-containing functional groups present in the sample contribute to the overall reduction current, as is previously reported .[224] Therefore, electrochemical measurements alone without separate product analyses are less reliable for the determination of ORR pathway for Ox-GQDs. The N-GQDs presented better consistency. Due to their low onset potentials and high selectivity towards the 2-electron process, both N_E-GQDs and N_P-GQDs are good candidates for electrocatalysis of hydrogen peroxide formation. Due to the high resistance of the electrodes, further work could improve this process by increasing the hydrophobicity of the GQDs so that they require a lower nafion content as a binder.

3.4 Conclusion

In conclusion, we have prepared nitrogen doped GQDs from CNOs using laser ablation in liquid. This method offered several advantages over traditional methods due to few byproducts, fast production times, and the tunability of the PL and functional groups. The choice of solutes in the liquid allowed for tuning of the types of nitrogen functional groups that were present and also influenced the overall nitrogen content. The resultant N-GQDs had PL properties that were tunable based on the ratios of N-functional groups. It was observed that a high content of amine functional groups resulted in more red shifted emission, while a high concentration of pyridinic nitrogen significantly blue shifted the emission. PL lifetime measurements indicated that intrinsic states have a fast decay, while the functional groups exist as extrinsic states with slower decays. A combination of hydroxyl and amine functional groups lead to a decay in the 3-4 ns range, while the more polar carboxylic or pyridinic groups have decays that range from 9 to 13 ns. These N-

GQDs exhibited highly selective catalytic activity towards the 2-electron process for the ORR, with the N_E-GQDs and N_P-GQDs having the best onset potentials and selectivity. Future works will look towards improving the catalytic performance by increasing the hydrophobicity of the samples through tuning of laser solution parameters, and alternative, more readily available carbon precursors will also be explored. Finally, it should be noted that the choice of solvent and its properties such as polarity and viscosity may significantly influence PL lifetime and PLQY of GQDs and should be considered for applications.

3.5 Supporting information

3.5.1 TEM Histograms
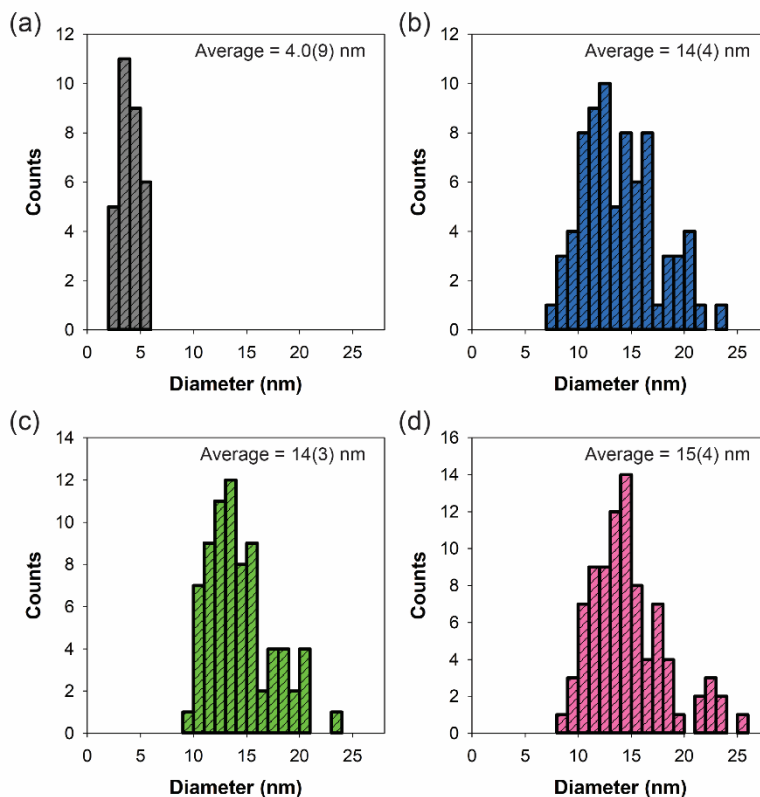
Figure S3.1 Histograms of GQD diameter distributions obtained from TEM images for Ox-GQDs (a), NA-GQDs (b), NE-GQDs (c), and NP-GQDs (d).

3.5.2 AFM Measurements

3.5.2.1 AFM Experimental Details

Solutions of the various GQDs were adjusted in concentration to have an absorbance of 0.15 at 200 nm. A 5 μL aliquot of each solution was spin cast on a mica disk (Ted Pella, Inc.) at 2000 rpm for 60 s. Samples were analyzed using a Bruker Dimension Icon Scanning Probe Microscope in ScanAsyst PeakForce Tapping mode using a silicon tip on a nitride lever. Samples were analyzed using the free and open source scanning probe microscopy data visualization and analysis software Gwyddion.

3.5.2.2 AFM images and height information
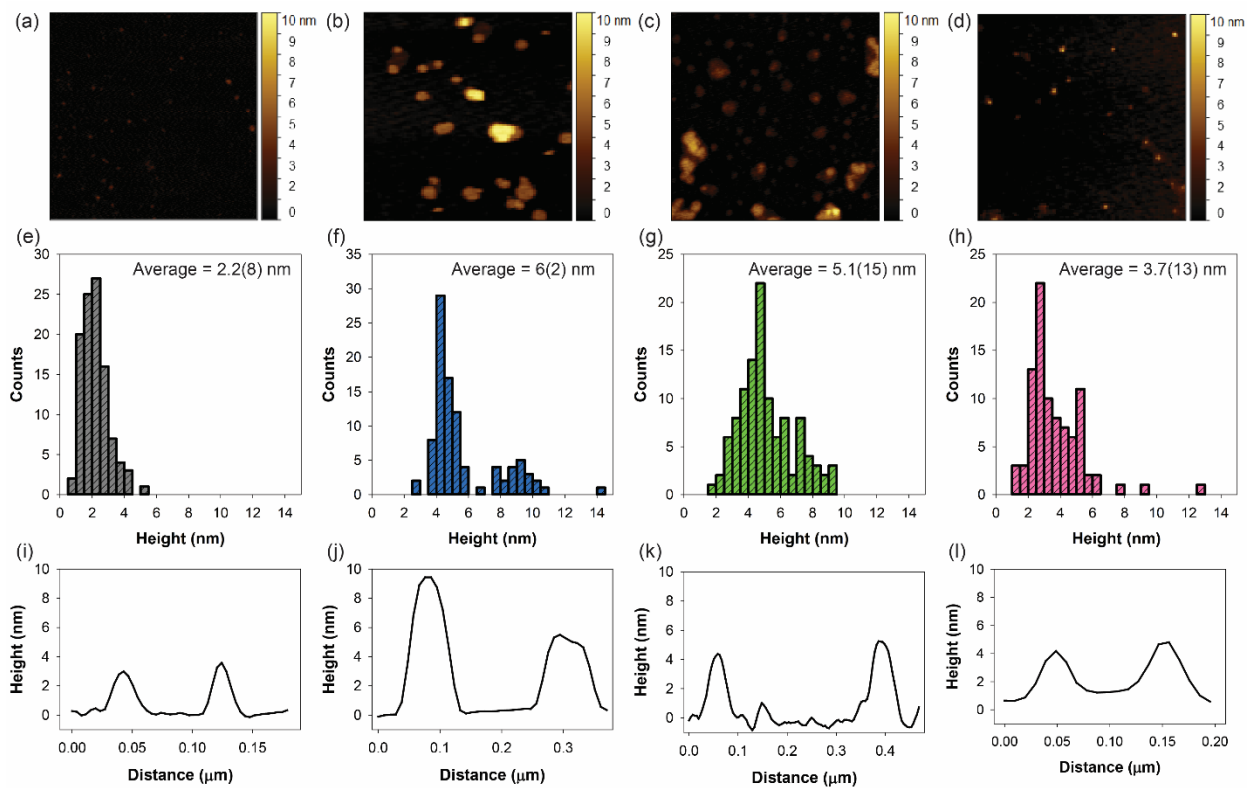
Figure S3.2 AFM images (a-d), height distributions (e-h), and height profiles of various particles (i-l) for Ox-GQDs (left), NA-GQDs (left center), NE-GQDs (right center), and NP-GQDs (right).

3.5.3 Product Yield

The percent mass yield of GQDs formed during a typical LAL experiment was determined by calculating the ratio of Ox-GQDs formed to unreacted pellet. The difference in mass of the pellet before and after LAL was used to determine how much of the pellet was consumed in the reaction. Following LAL, the pellet was dried in a 40 °C oven overnight following LAL and then allowed to return to room temperature before obtaining the mass, and the mass of the Ox-GQDs after filtration was used to determine the yield.

$$Percent\ mass\ yield = 100 \times \frac{Mass\ of\ LA-GQDs}{Mass\ of\ Consumed\ Pellet} \qquad \text{(Equation 3.1)}$$

Table S3.1 Calculation of product yield

Mass pellet before ablation:	44.6(1) mg
Mass pellet after ablation:	42.6(2) mg
Mass of consumed pellet:	2.0(2) mg
Mass Ox-GQDs before filtering:	1.7(2) mg
Mass Ox-GQDs after filtering:	1.03(8) mg
% Mass Yield (after filtering):	53(7)%

3.5.4 XPS Details

3.5.4.1 XPS Survey Scans

XPS survey scans were obtained using a Thermo Scientific K-Alpha X-ray Photoelectron Spectrometer System with an Al K_α x-ray source. For each sample five scans in the range of -10 to 1350 eV were measured with a spot size of 400 µm. The relative percentages were calculated using Thermo Avantage version 5.925 software.
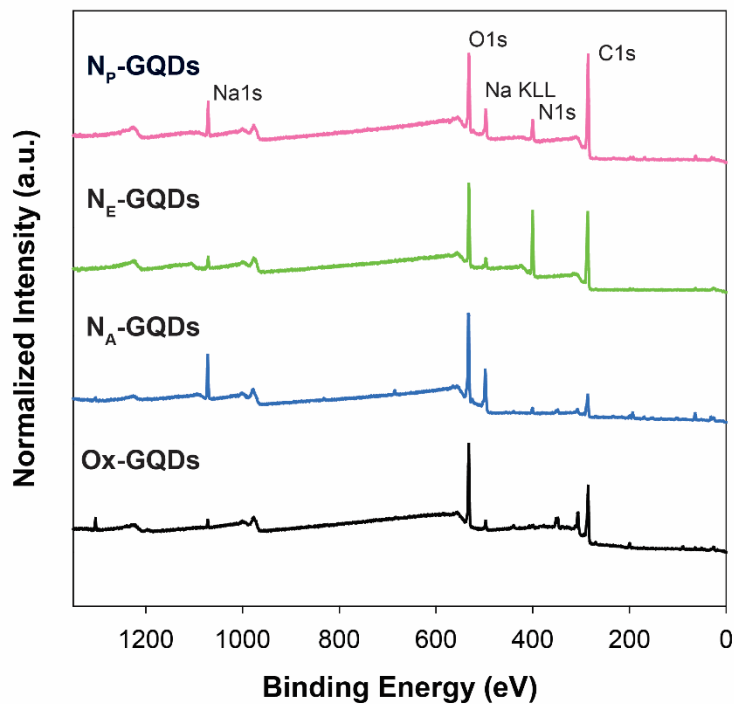
Figure S3.3 Survey XPS spectra for the Ox-GQDs and N-GQDs produced with ammonia, ethylenediamine and pyridine.

Table S3.2 Elemental ratios of the Ox-GQD and N-GQDs as determined from XPS survey scans.

Element	Ox-GQDs	N_A-GQDs	N_E-GQDs	N_P-GQDs
C	64.8	39.3	56.8	68.2
O	33.5	55.9	20.2	21.5
N	1.7	4.8	23.0	10.2

3.5.4.2   XPS C1s high resolution scans

XPS C1s high resolution scans were obtained by measuring 10 scans in the range 279-298 eV with a spot size of 400 μm. The spectra were deconvoluted using Thermo

Avantage software with a full width at half max (FWHM) of 1.25 eV for each peak and a 30% Lorentzian/Gaussian (L/G) mixed convolution.

Table S3.3 XPS C1s high resolution energies and fractions of various carbon chemical states in the GQDs.

Assignment	C1s binding energy (eV)[215-217]	Ox-GQDs	N_A-GQDs	N_E-GQDs	N_P-GQDs
sp^2	284.5	38.6%	9.4%	8.5%	26.2%
sp^3	285.3	28.6%	21.8%	24.0%	31.2%
C-N	286.1	1.5%	29.5%	30.4%	23.1%
C-O	287.0	13.9%	14.2%	16.7%	10.0%
C=O	288.0	7.3%	12.7%	14.3%	7.5%
O-C=O	289.0	10.0%	12.4%	6.1%	2.2%

3.5.4.3   XPS N1s high resolution scans

XPS N1s high resolution scans were obtained by measuring 10 scans in the range 392-410 eV with a spot size of 400 µm. The spectra were deconvoluted using Thermo Avantage software with a FWHM of 1.3 eV for each peak and a 30% L/G mixed convolution.

Table S3.4 XPS N1s high resolution energies and fractions of various nitrogen chemical states in the N-GQDs.

Assignment	N1s binding energy (eV)[215, 218-219]	N_A-GQDs	N_E-GQDs	N_P-GQDs
Pyridinic	398.8	10.8%	15.3%	31.3%
Amine	399.7	38.4%	49.3%	35.2%
Pyrrolic	400.7	40.0%	30.0%	20.4%
Graphitic	401.8	10.8%	5.4%	13%

3.5.5   Precursor CNO Optical Data

A suspension of CNOs in water was prepared and sonicated prior to obtaining absorbance and PL spectra. A baseline absorbance with no resolved peaks indicates that the CNOs are metallic in nature and lack any quantum confinement effects. Similarly, the PL spectra show no emission peaks at any excitation wavelengths indicating the precursor lacks any PL prior to laser ablation. (The sharp, excitation dependent peaks are Raman scattering from water.)
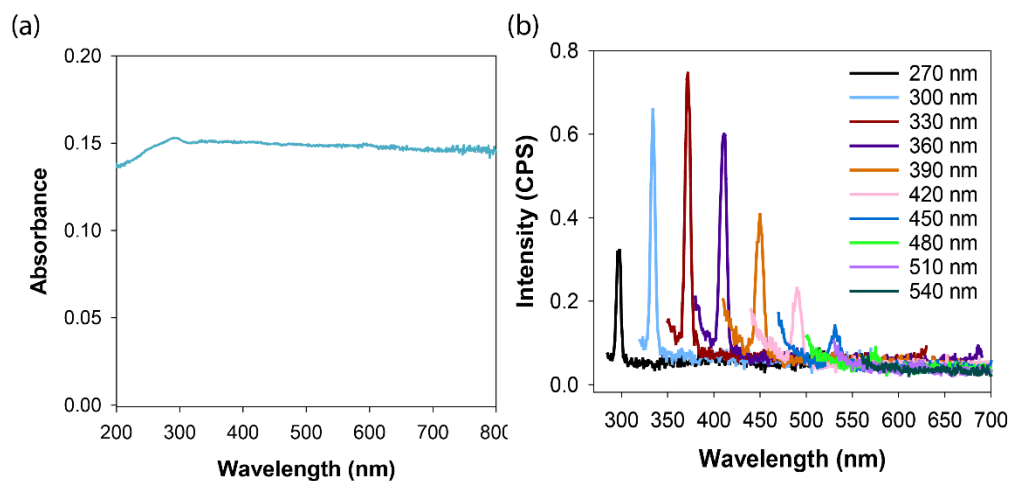
Figure S3.4 Absorbance (a) and PL emission spectra (b) of the precursor CNOs.

3.5.6   Excitation Spectra of GQDs
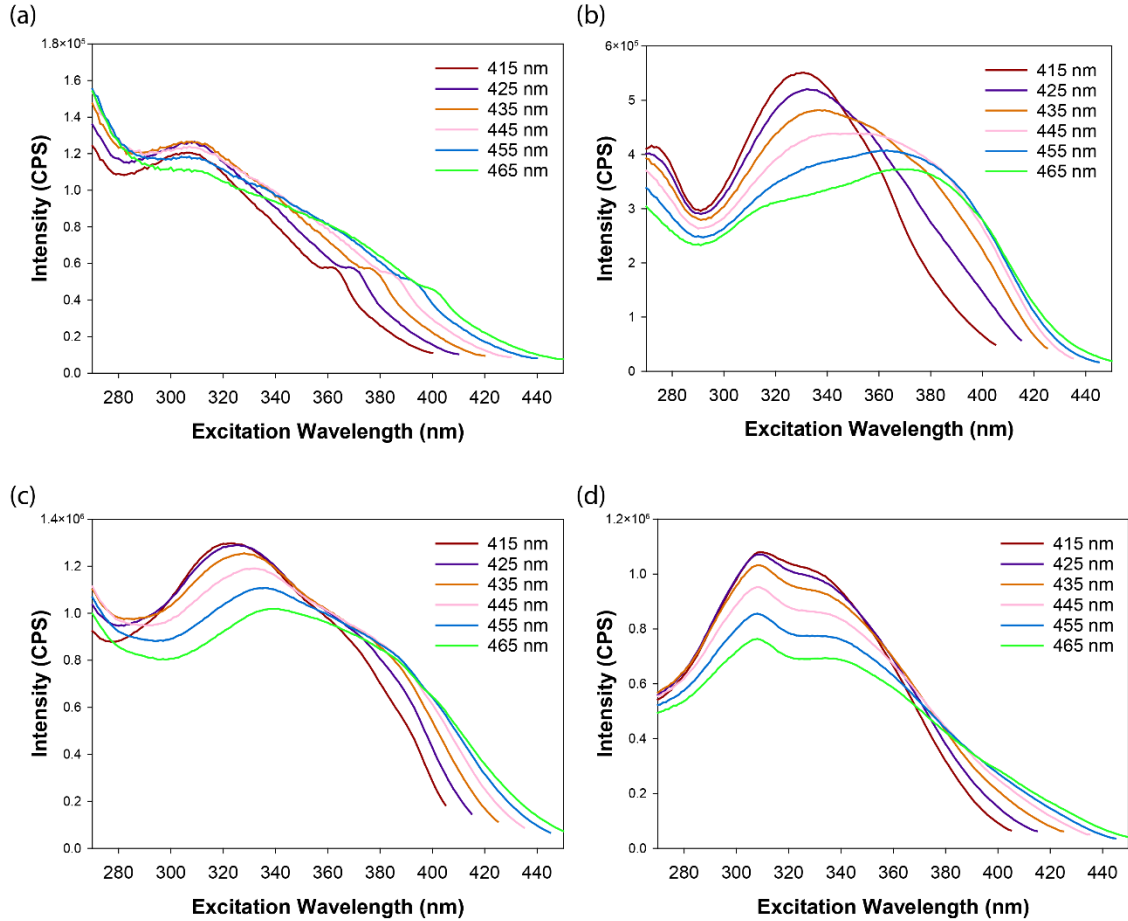
Figure S3.5 PL excitation spectra at various emission wavelengths for the Ox-GQDs (a), NA-GQDs (b), NE-GQDs (c), and NP-GQDs (d).

3.5.7   Time Correlated Single Photon Counting (TCSPC) Measurements of GQDs

Photoluminescence decays were fit to three exponential functions in the form of Equation 2.1: $y = A + B_1 e^{-t/\tau_1} + B_2 e^{-t/3} + B_3 e^{-t/\tau_3}$ and the relative contributions were calculated by Equation 2.2: $\% \tau_n = 100 \times \dfrac{B_n \tau_n}{B_1 \tau_1 + B_2 \tau_2 + B_3 \tau_3}$.

Table S3.5 Exponential fitting parameters for the TCSPC fluorescence lifetime analyses of the GQDs at 425 nm emission.

$\lambda_{ex} = 393$ nm, $\lambda_{em} = 425$ nm				
Sample	*Ox-GQDs*	*N$_A$-GQDs*	*N$_E$-GQDs*	*N$_P$-GQDs*
A	5.10(10)	2.53(10)	1.34(9)	1.51(6)
B$_1$	0.1177(4)	0.0965(4)	0.0276(2)	0.0519(2)
τ_1 (ns)	0.346(10)	0.355(12)	0.92(5)	0.56(3)
B$_2$	0.01689(6)	0.01946(6)	0.02482(8)	0.02336(6)
τ_2 (ns)	2.71(5)	3.02(5)	3.52(4)	3.56(3)
B$_3$	0.001944(11)	0.002953(13)	0.00470(2)	0.003376(11)
τ_3 (ns)	9.13(8)	9.17(6)	8.86(5)	11.43(5)

Table S3.6 Exponential fitting parameters for the TCSPC fluorescence lifetime analyses of the GQDs at 465 nm emission.

$\lambda_{ex} = 393$ nm, $\lambda_{em} = 465$ nm				
Sample	*Ox-GQDs*	*N$_A$-GQDs*	*N$_E$-GQDs*	*N$_P$-GQDs*
A	5.14(13)	1.90(11)	1.86(12)	3.5(2)
B$_1$	0.0544(3)	0.0378(2)	0.0280(2)	0.02121(6)
τ_1 (ns)	0.60(2)	0.80(3)	1.09(2)	1.15(2)
B$_2$	0.02180(7)	0.02195(7)	0.02133(8)	0.02937(15)
τ_2 (ns)	3.24(6)	3.92(4)	4.17(11)	4.44(9)
B$_3$	0.00347(2)	0.00344(2)	0.00482(2)	0.003612(13)
τ_3 (ns)	9.58(7)	10.01(7)	9.91(6)	13.31(7)

3.5.8 PLQY Measurements

PLQY values were obtained using a traditional relative quantum yield method. Several concentrations of each sample were prepared such that their absorbance ranged from about 0.02-0.1 at the excitation wavelength that gave maximum emission (λ=330 nm for Ox-GQDs and N$_P$-GQDs, λ=360 nm for N$_E$-GQDs, and λ=390 nm for N$_A$-GQDs. Solutions of quinine sulfate (Fisher Scientific) were prepared in 0.01 M H$_2$SO$_4$ (VWR) to use as a standard and were adjusted in concentration to range from 0.02-0.1 at 330 nm, 360 nm, and 390 nm. The PL emission spectra of each solution was collected at the appropriate excitation wavelength using slit widths of 1.5 nm and an integration time of 0.1 s. The spectra were corrected for differences in collection efficiency and gratings at various emission wavelengths. The resulting spectra were integrated using Horiba Scientific FluoroEssence™ software. The integrated PL was plotted vs. their corresponding absorbance at the chosen excitation wavelength and the slopes of the linear best fits were used to calculate quantum yield based on the following equation where Φ represents PLQY, and η represents the refractive index of the solvent:

$$\Phi_{GQD} = \Phi_{Quinine\ Sulfate} \left(\frac{Slope_{GQD}}{Slope_{Quinine\ Sulfate}} \right) \left(\frac{\eta^2_{H_2O}}{\eta^2_{0.1\ M\ H_2SO_4}} \right) \qquad \text{(Equation 3.2)}$$

The known values $\Phi_{Quinine\ Sulfate}$= 54%, η_{H_2O}=1.33, and $\eta_{H_2SO_4}$=1.33 were used to calculate PLQY for the various GQD samples.[215]
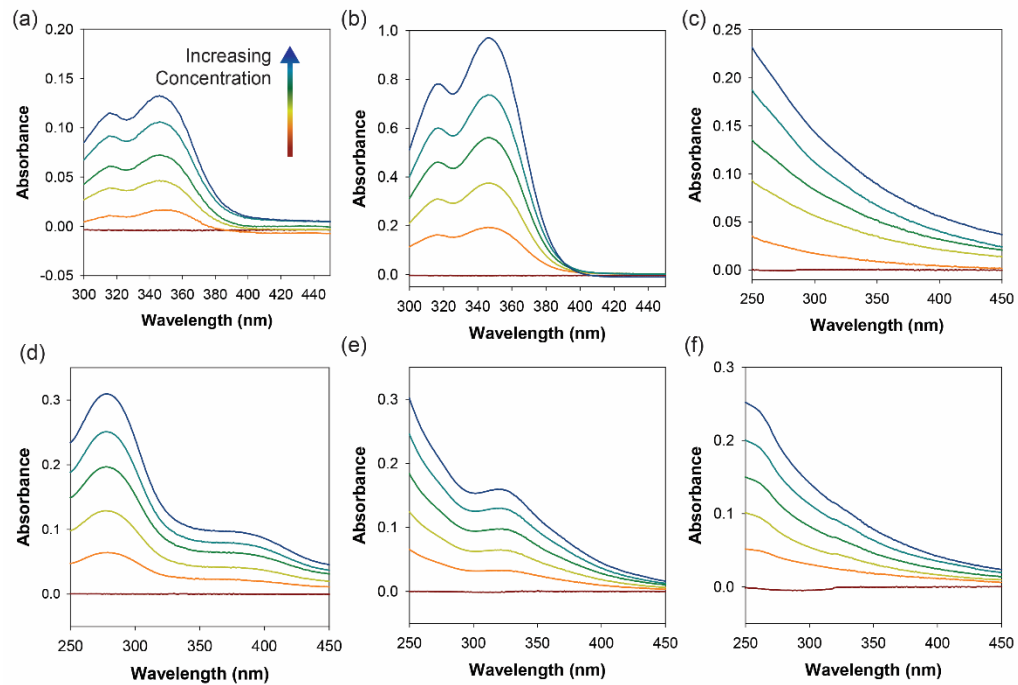
Figure S3.6 UV-visible absorbance spectra at various concentrations for quinine sulfate (a-b), Ox-GQDs (c), NA-GQDs (d), NE-GQDs (e), and NP-GQDs (f).
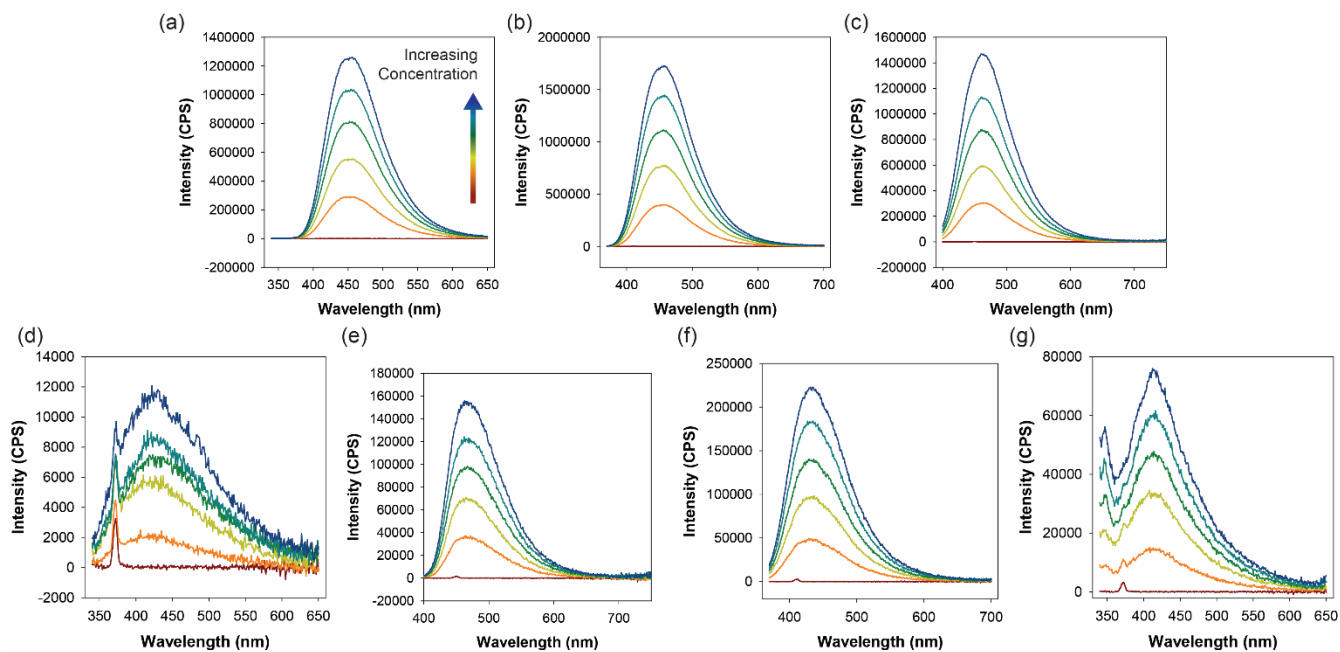
Figure S3.7 PL spectra at various concentrations for quinine sulfate at 330 nm excitation (a), 360 nm excitation (b), and 390 nm excitation (c), and Ox-GQDs at 330 nm excitation (d), NA-GQDs at 390 nm excitation (e), NE-GQDs at 360 nm excitation (f), and NP-GQDs at 330 nm excitation (g).

Table S3.7 Absorbance and Integrated PL intensities for various concentrations of quinine sulfate.

	$\lambda_{330\ nm}$		$\lambda_{360\ nm}$		$\lambda_{390\ nm}$	
	Abs.	*Integrated PL (a.u.)*	*Abs.*	*Integrated PL (a.u.)*	*Abs.*	*Integrated PL (a.u)*
H_2SO_4	-0.004	72,727	-0.004	65,979	-0.004	20,413
Solution 1	0.010	28,822,903	0.013	39,838,124	0.017	30,133,589
Solution 2	0.037	55,230,908	0.036	77,408,002	0.029	58,497,403
Solution 3	0.059	80,809,408	0.058	111,745,468	0.042	86,502,525
Solution 4	0.088	103,340,776	0.086	145,342,251	0.051	112,024,931
Solution 5	0.110	126,153,721	0.107	174,345,861	0.052	146,178,750

Figure 3.8 Absorbance and Integrated PL intensities for various concentrations of GQD samples.

	Ox-GQDs ($\lambda_{330 \text{ nm}}$)		N_A-GQDs ($\lambda_{390 \text{ nm}}$)		N_E-GQDs ($\lambda_{360 \text{ nm}}$)		N_P-GQDs ($\lambda_{330 \text{ nm}}$)	
	Abs.	*Integrated PL (a.u.)*	*Abs.*	*Integrated PL (a.u.)*	*Abs.*	*Integrated PL (a.u)*	*Abs.*	*Integrated PL (a.u.)*
H₂O	0.0005	36,000	0.0001	33,204	0.0001	30,923	-0.0004	36,000
Solution 1	0.012	308,202	0.021	3,656,450	0.021	5,179,554	0.022	1,803,232
Solution 2	0.043	886,033	0.04	7,048,606	0.04	10,431,821	0.041	4,162,513
Solution 3	0.063	1,175,252	0.061	10,050,865	0.06	14,987,750	0.061	5,843,780
Solution 4	0.083	1,317,399	0.076	12,714,121	0.08	19,784,354	0.083	7,513,861
Solution 5	0.109	1,811,518	0.092	15,797,590	0.098	23,954,636	0.103	9,249,581
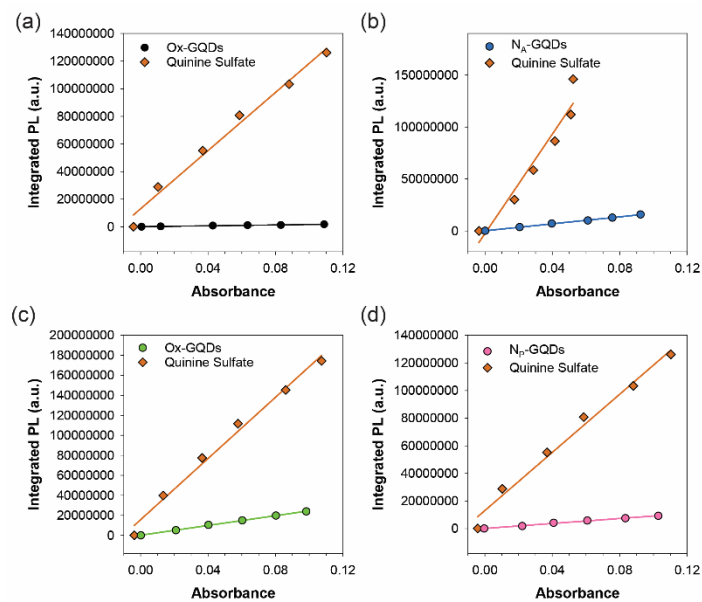
Figure S3.8 Plots of integrated PL intensity vs. absorbance and their corresponding linear best fits at 330 nm for Ox-GQDs (a), at 390 nm for NA-GQDs (b), at 360 nm for NE-GQDs (c), and at 330 nm for NP-GQDs (d).

Table S3.9 Linear fit parameters for absolute quantum yield measurements.

Sample	Slope	R^2
Quinine Sulfate $\lambda_{330\ nm}$	$1.05(6) \times 10^9$	0.9857
Quinine Sulfate $\lambda_{360\ nm}$	$1.53(8) \times 10^9$	0.9888
Quinine Sulfate $\lambda_{390\ nm}$	$2.4(3) \times 10^9$	0.9321
Ox-GQDs	$1.57(10) \times 10^7$	0.9852
N_A-GQDs	$1.68(3) \times 10^8$	0.9986
N_E-GQDs	$2.44(3) \times 10^8$	0.9993
N_P-GQDs	$9.0(3) \times 10^7$	0.9945

Table S3.10 Calculated relative PLQYs for the various GQD samples.

Sample	Ox-GQDs	N_A-GQDs	N_P-GQDs	N_P-GQDs
PLQY(%)	0.81(7)	3.8(5)	8.6(4)	4.6(3)

3.5.9 Photostability Tests

A 0.025 mg/mL solution of each GQD sample was measured at continuous excitation for 1 hour. Each sample was measured at the excitation and emission wavelength that gave maximum emission. To account for any fluctuation in excitation intensity the, excitation was monitored throughout the measurement and the ratio of the emission and excitation intensity is shown in the figure below. To determine the percent decrease in intensity, the average intensity from the first minute was compared to the average intensity from the last minute. The minimal decrease in intensity indicates that the GQDs are photostable under conditions with low intensity illumination.
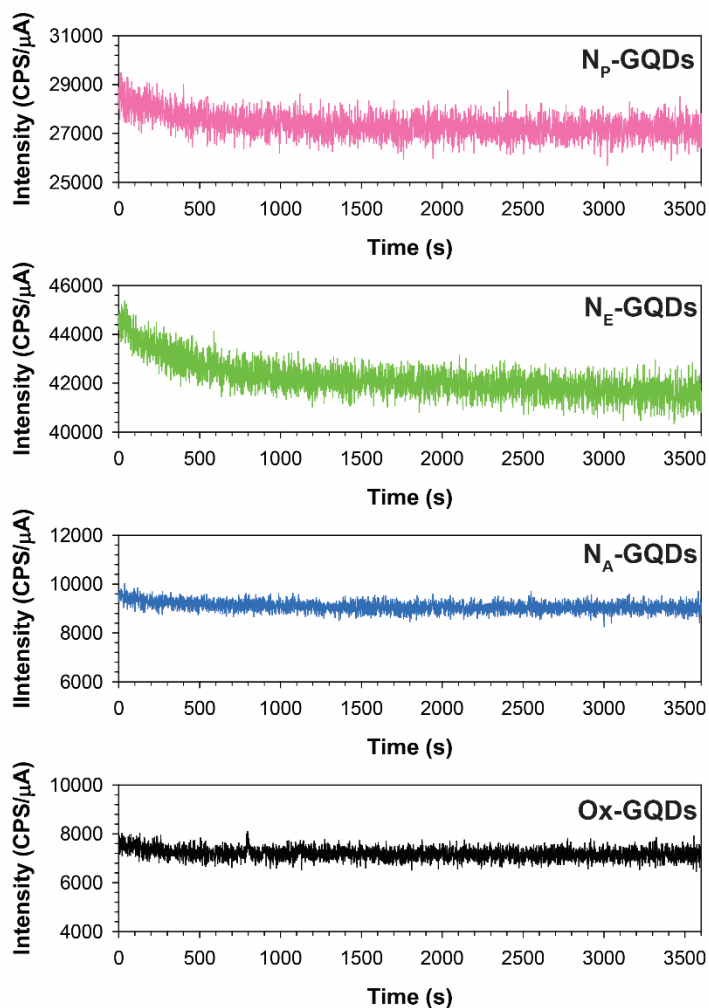
Figure S3.9 Photostability tests of various GQD samples.

Table S3.11 Calculated decrease in PL intensity for various GQD samples.

	Ox-GQDs	N$_A$-GQDs	N$_E$-GQDs	N$_P$-GQDs
λ_{ex} (nm)	330	390	360	330
λ_{ex} (nm)	445	465	435	415
Average Initial Intensity (CPS/μA)	7559	9518	44457	28447
Average Final Intensity (CPS/μA)	7133	9016	41545	27178
Intensity Decrease (%)	5.6	5.3	6.6	4.5

3.5.10   Purification Effects on PL

To test the effects that purification had on the PL properties, dialysis was performed for one week on each sample using a 1000 Dalton molecular weight cutoff membrane and water as the liquid. PL spectra of the GQDs were obtained both before and after dialysis. Additionally, the liquid outside the membrane was saved and a majority of the water was evaporated out to concentrate any removed components before collecting PL measurements. The spectra before and after dialysis show very similar profiles, indicating that the emitting species is retained in the dialysis membrane. The components that escaped the membrane show only weak PL, and for Ox-GQDs and N$_A$-GQDs the emission profile is noticeably different from the samples retained during dialysis. This suggests that a majority of the PL properties are from the GQDs rather than small side components that would be removed during dialysis.
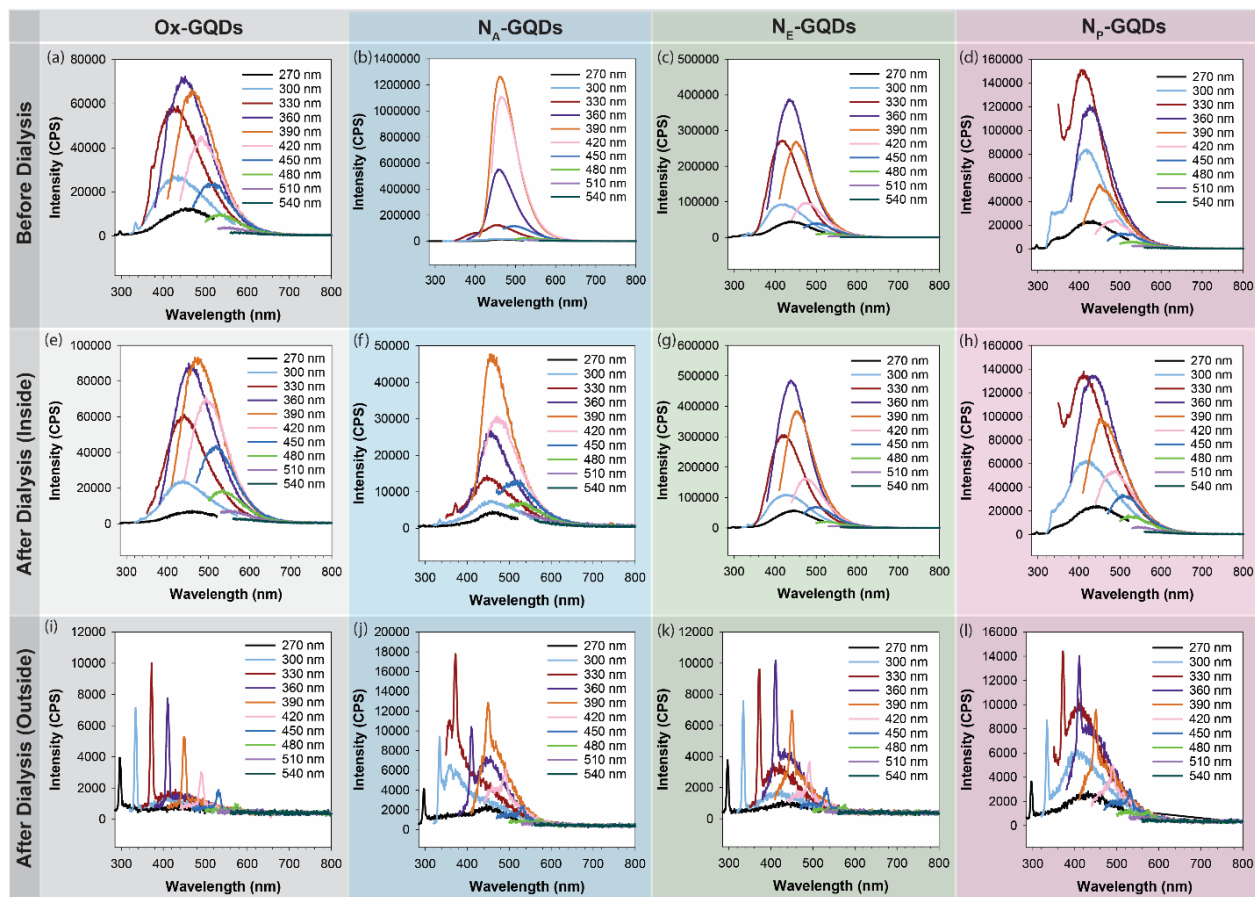
Figure S3.10 Test of purification effects on GQD PL. The spectra of various Ox-GQDs (a, e, i), NA-GQDs (b, f, j), NE-GQDs (c, g, k), and NP-GQDs (d, h, l) are shown before dialysis (top row), after dialysis inside the dialysis membrane (center row), and after dialysis outside the dialysis membrane (bottom row).

3.5.11 Electrochemical Measurements

3.5.11.1 Current-Resistance Compensation

The measured potentials were corrected for uncompensated resistance according to the following equations:

$$E_{real} = E_{measured} - IR_u \qquad \text{(Equation 3.3)}$$

Where E_{real} is the real potential, $E_{measured}$ is the uncompensated, measured potential, I is the current at the particular potential, and R_u is the uncompensated resistance.[225-226] The uncompensated resistance values for each electrode were measured with the potentiostat and are reported in Table S3.12.

Table S3.12 Measured resistance values for various electrodes in a N2 and O2 saturated environment.

Sample	N$_2$ Saturated Resistance (Ω)	O$_2$ Saturated Resistance (Ω)
Carbon Black	122.8	60.4
Pt/C	118.1	72.8
Ox-GQDs	99.3	58.4
N$_A$-GQDs	122.8	71.3
N$_E$-GQDs	501.8	503.6
N$_P$-GQDs	729.2	530.8

3.5.11.2 Conversion From Ag/AgCl to RHE

The measured potentials were converted from Ag/AgCl to the reversible hydrogen electrode (RHE) via the Nernst equation as follows:

$$E_{RHE} = E_{Ag/AgCl} + 0.059 \, pH + E°_{Ag/AgCl} \qquad \text{(Equation 3.4)}$$

In this equation E_{RHE} is the potential vs. RHE, $E_{Ag/AgCl}$ is the measured potential (vs. Ag/AgCl), pH refers to the pH of the solution, and $E°_{Ag/AgCl}$ is the standard potential for Ag/AgCl at 25°C ($E°_{Ag/AgCl}$ = 0.1976 V)[227]. Since all measurements were collected in 0.1 M KOH (pH = 13) the equation simplifies to:

$$E_{RHE} = E_{Ag/AgCl} + 0.9646 \qquad \text{(Equation 3.5)}$$

3.5.11.3 Cyclic Voltammetry Scans
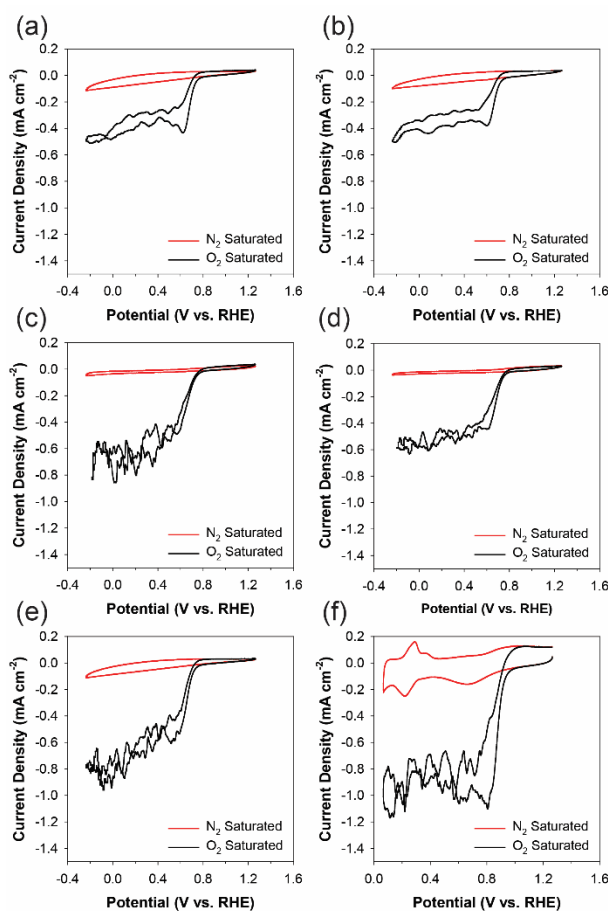
Figure S3.11 CV scans in a N2 (gray lines) and O2 saturated (black lines) environment of the Ox-GQDs (a), NA-GQDs (b), NE-GQDs (c), NP-GQDs (d), carbon black (e) and Pt/C (f).

109

3.5.11.4 Rotating Disk Electrode Measurements and the Koutecky-Levich Equation

The Koutecky-Levich (K-L) equation was used to determine the electron transfer number from rotating disk electrode (RDE) measurements at various potentials for the various GQD samples. The equation is defined as:

$$\frac{1}{j} = \frac{1}{j_k} + \frac{1}{B\omega^{0.5}}$$

(Equation 3.6)

In this equation, j is the current density in units of A cm^{-2}, j_k is the kinetic current density, B is the Levich slope, and ω is the rotation speed in units of rpm. B is defined as:

$$B = 0.2nF\left(D_{O_2}\right)^{\frac{2}{3}}v^{-\frac{1}{6}}C_{O_2}$$

(Equation 3.7)

Where the constant 0.2 is used when the rotation speed is in rpm, n is the electron transfer number, F is the Faraday constant (F=96485 C mol^{-1}), D_{O2} is the diffusion coefficient of O_2 in a 0.1 M KOH solution (D_{O2} = 1.9 ×10^{-5} cm^2 s^{-1}), v is the kinematic viscosity for KOH (v = 0.01 cm^2 s^{-1}) and C_{O2} is the concentration of O_2 in solution at room temperature (C_{O2} = 1.2 × 10^{-6} mol cm^{-3}).[49, 228]
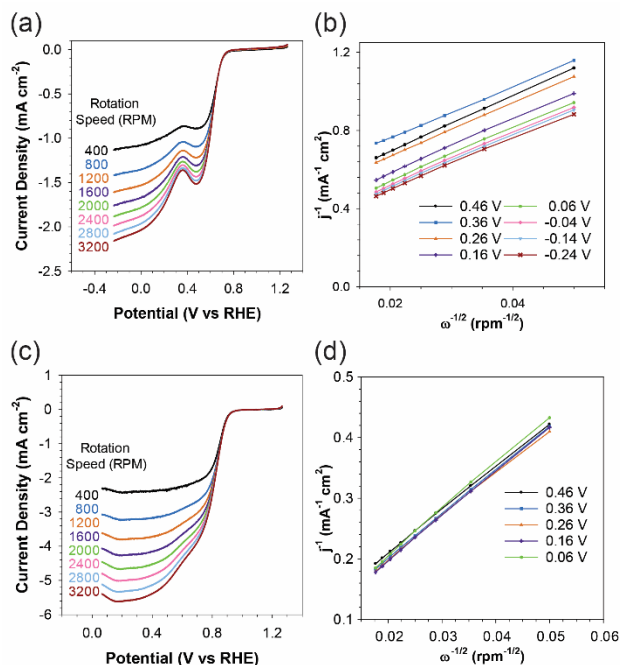
Figure S3.12 RDE LSV scans in an O2 saturated environment of the carbon black (a) and Pt/C (c) and their derived K-L plots (b,d).

Table S3.13 Onset potentials and electron transfer numbers for various GQDs samples, carbon black, and Pt/C determined from RDE measurements.

	Ox-GQDs	N_A-GQDs	N_E-GQDs	N_P-GQDs	Carbon black	Pt/C
Onset Potential (V)	0.72	0.72	0.74	0.75	0.70	0.90
Potential (V)	Calculated electron transfer number (RDE)					
-0.5	1.42	2.16	2.7	2.12	1.98	3.95
-0.6	1.41	2.13	2.95	2.16	2.14	3.87
-0.7	1.45	2.05	2.88	2.1	2.06	3.94
-0.8	1.50	2.05	2.73	2.05	2.05	3.81
-0.9	1.57	2.04	2.76	2.05	2.07	3.67
-1	1.69	2.05	2.66	2.06	2.1	NA
-1.1	1.73	2.04	2.58	2.07	2.11	NA
-1.2	2.08	2.04	2.53	2.1	2.16	NA

111

3.5.11.5 Rotating Ring Disk Electrode Measurements

RRDE measurements were obtained using a glassy carbon disk working electrode where O_2 reduction takes place with an additional Pt ring working electrode where oxidation of peroxide (if produced by the disk electrode) takes place to detect peroxide production. A potential of 0.35 V was applied across the two electrodes and measurements were collected at 1600 rpm rotation speed. The following equations were used to determine electron transfer number (n) and percentage of peroxide production (%HO$^-_2$):

$$n = \frac{4j_d}{j_d + \frac{j_r}{N}} \qquad \text{(Equation 3.8)}$$

$$\%HO_2^- = 200 \times \frac{\frac{j_r}{N}}{j_d + \frac{j_r}{N}} \qquad \text{(Equation 3.9)}$$

In this equation j_d is the disk current, j_r is the ring current, and N is the collection efficiency of the Pt ring electrode (N=0.4)[229]. The value of N was determined from the reduction of potassium ferricyanide.
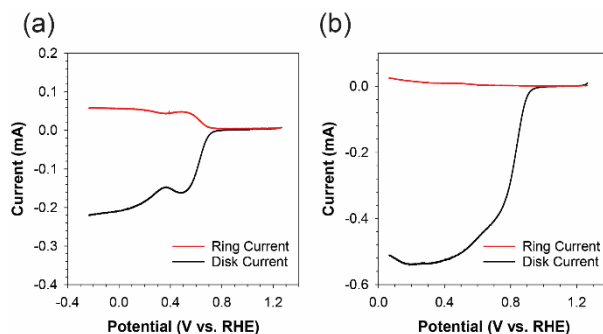
Figure S3.13 RRDE LSV scans in an O2 saturated environment of the carbon black (a) and Pt/C (b).

Table S3.14 Electron transfer numbers for various GQDs samples, carbon black, and Pt/C determined from RRDE measurements.

Calculated electron transfer number (RRDE)						
Potential (V)	Ox-GQDs	N_A-GQDs	N_E-GQDs	N_P-GQDs	Carbon black	Pt/C
-0.5	2.60	2.33	2.25	2.36	2.3	3.83
-0.6	2.60	2.36	2.28	2.4	2.29	3.83
-0.7	2.62	2.4	2.31	2.42	2.32	3.78
-0.8	2.64	2.42	2.34	2.43	2.34	3.7
-0.9	2.69	2.43	2.36	2.44	2.36	3.57
-1	2.76	2.44	2.36	2.45	2.39	
-1.1	2.83	2.45	2.35	2.44	2.4	
-1.2	2.88	2.44	2.35	2.36	2.41	

Table S3.15 H_2O_2 production efficiency for various GQDs samples, carbon black, and Pt/C determined from RRDE measurements.

Calculated H_2O_2 Efficiency (RRDE)						
Potential (V)	Ox-GQDs	N_A-GQDs	N_E-GQDs	N_P-GQDs	Carbon black	Pt/C
-0.5	70.0	83.31	87.49	83.69	85.17	8.4
-0.6	69.8	82.65	86.18	81.87	85.57	8.44
-0.7	69.2	81.57	84.26	80.09	84.13	10.77
-0.8	68.0	80.21	82.94	78.92	82.94	15.17
-0.9	65.6	79.2	82.16	78.28	82.16	21.75
-1	62.1	78.69	81.9	78.01	80.61	
-1.1	58.7	78.2	82.43	77.56	80.15	
-1.2	55.9	77.24	82.46	77.94	79.44	

CHAPTER 4. Controlled structure and solubility of NaYF$_4$:Yb/Er
upconverting nanoparticles produced by laser ablation in liquid

4.1   Introduction

Upconverting nanomaterials have received considerable attention due to their ability to convert low energy, near infrared (NIR) light into higher energy, visible light.[82, 84] Specifically, NaYF$_4$ co-doped with Yb^{3+} and Er^{3+} (NaYF$_4$:Yb/Er) has been widely studied as a system that undergoes the energy transfer upconversion (ETU) mechanism.[99] This system is advantageous because the NaYF$_4$ matrix is optically transparent in both NIR and visible regions and has a low phonon energy which makes it less susceptible to non-radiative relaxation.[82] Yb^{3+} acts as a photosensitizer and has a uniquely strong NIR absorbance around 980 nm for the $^2F_{5/2} \leftarrow\ ^2F_{7/2}$ transition.[230] Energy from the initially photoexcited Yb^{3+} sensitizer is transferred to an activator Er^{3+} which has close energy matching with Yb^{3+} and long-lived excited states.[95, 230] This allows multiple energy transfers to occur before Er^{3+} emits in the visible region with strong green emission bands at 525 and 545 nm and a red emission band at 660 nm (Figure S4.1). Since the emission occurs from lanthanide atomic transitions that originate from 4f orbitals and Yb^{3+} and Er^{3+} embedded in the solid host are isolated from the fluctuating dipoles of solvent molecules, the photoluminescence (PL) bands are narrow, and the emission wavelengths are not sensitive to either quantum confinement due to particle size or surrounding environment such as a capping agent or a solvent.[82, 96] In addition to narrow emission bands, NaYF$_4$:Yb/Er nanomaterials offer many other advantages over other traditional PL materials such as no autofluorescence, a resistance to photobleaching, non-blinking behavior, low cytotoxicity, and longer penetration depths in tissues since the excitation and some emission bands of NaYF$_4$:Yb/Er are in the window of optical transparency for biological tissues.[99, 114-115, 147, 150] These unique PL properties make lanthanide based upconverters desirable for many biological applications including imaging[99, 132], targeted

drug delivery[125], sensing[122], and photodynamic therapy[121, 231].

A high upconversion efficiency is a prerequisite of UCNPs. It has been established that NaYF$_4$:Yb/Er materials can exist in either a cubic phase (α-phase) or hexagonal phase (β-phase) and that a β-phase leads to a better upconversion efficiency and is therefore more desirable.[101] However, a β-phase is harder to produce and requires higher reaction temperatures and highly controlled conditions. Many methods implemented to produce a β-phase involve high boiling point solvents, long reaction times, or high temperature and pressure environments, and these techniques suffer limitations of toxic side products, irreproducibility, and water-insoluble products due to an oleate capping agent.[86, 100, 137] The solubility issue is most commonly addressed by post modification strategies that include ligand exchange, amphiphilic polymers to form bilayers, inorganic shells, emulsions, or chemically modifying the existing capping agent to make it more water soluble.[96, 115, 129, 137, 232] Ligand free UCNPs stabilized by electrostatic interactions have also been considered but still require additional steps to remove the native oleate ligand.[146] Other researchers have shown that the crystallinity and phase can be improved by annealing the nanoparticles after synthesis; however, this method often leads to agglomeration of the particles and reduced solubility.[86, 107, 143] Solvothermal or hydrothermal synthesis has also been proposed as an alternate strategy to produce highly efficient, β-phase upconverters[107], but the required high temperatures and pressures needed to form the UCNPs can cause degradation of the capping agent.[137]

Laser ablation in liquid (LAL) has emerged as a promising method to produce nanomaterials with use of fewer chemicals, production of fewer by-products, and requiring fewer purification steps.[161, 179] Typically, a target of precursor material is placed for the irradiation of a pulsed laser in the presence of a liquid. The laser irradiates the target which then releases material that can interact with the liquid. The mechanism for the nanomaterial formation is highly dependent on the laser pulse width and fluence and the properties of the target material.[164] LAL has been implemented to produce a variety of optically active

nanomaterials including lanthanide based UCNPs.[155-159, 233] However, many of these studies used an oxide host lattice which is less desirable due to a higher phonon energy than the fluoride based UCNPs.[99] Additionally, it is desirable to compare UCNPs with those prepared by more traditional methods to assess the feasibility of LAL as an alternative approach for UCNP preparation.

Herein we present the novel synthesis of water stable UCNPs using the LAL approach. By using a β-phase target, a bulk starting material was converted into UCNPs with high upconversion efficiency. By employing capping agents dissolved in water, the surface of UCNPs was modified during LAL and the UCNPs became more stabilized in water. The capping agents were found to have a substantial impact on the PL lifetimes of the produced material. We found that at low laser fluences, chemical composition of the UCNPs deviated from that of the target material; however, at high laser fluence, their composition resembled that of the bulk. Finally, we compared the LAL-produced nanoparticles to particles prepared by solvothermal synthesis to address the advantages and limitations of the LAL method.

4.2   Experimental

A detailed description of the materials and the characterization methods used is presented in the supporting information (section 4.5). Figure 4.1a-c illustrate experimental procedures to produce UCNPs through the LAL.

4.2.1   Pellet preparation and annealing

The NaYF$_4$:Yb/Er target was prepared by coprecipitation followed by annealing. 2.4 mmol Y(NO$_3$)$_3$•6H$_2$O, 0.51 mmol Yb(NO$_3$)$_3$•H$_2$O, and 0.09 mmol Er(NO$_3$)$_3$•H$_2$O were

dissolved in 30 mL deionized (DI) water. A separate solution of 27 mmol NaOH and 27 mmol NH_4F was prepared in 30 mL DI water. The two solutions were then combined, an additional 30 mL DI water was added, and the mixture was stirred for 30 minutes. The mixture was centrifugated by dividing it into eight centrifuge tubes and then washed three times with reagent alcohol. The resultant precipitate was dried overnight in a 40 °C oven. The dried precipitate from a single centrifuge tube was transferred into a pellet press and pressed to 10,000 psi for 15 minutes. The pellet was transferred to a quartz weighing boat for annealing under argon flow of about 0.5 L/ minute. Argon was first allowed to flow through the tube for 30 minutes. Then, in a typical experiment, the sample was heated at 30 °C/minute to 400 °C and maintained at 400 °C for 45 minutes. The sample was then cooled under argon flow. Various annealing parameters were investigated as described in the Results and Discussion section.

4.2.2 Laser ablation

In a typical LAL experiment, the pellet was transferred to a 2-dram (7.5 mL) vial. 3 mL of water, or an aqueous solution of citric acid (CA) or poly (ethylene glycol) (PEG, average M_n= 3000 Da) was added to the vial. The sample was then placed on a rotating stand and exposed to a nanosecond, Nd:YAG laser that was frequency doubled to 532 nm. The laser was directed through a prism and focused with a lens to a spot size of 1.5 mm diameter. The laser ablation was continued for 10 minutes, and then the liquid was extracted for analysis. Laser energies ranging from 10 to 110 mJ/pulse were investigated.

4.2.3 Solvothermal synthesis

For comparison with the LAL method, samples were also prepared via a more traditional, solvothermal route, similar to a previous report.[107] Briefly, a 10 mL mixture of 0.27 mmol Y(NO$_3$)$_3$•6H$_2$O, 0.06 mmol Yb(NO$_3$)$_3$•H$_2$O, 0.01 mmol Er(NO$_3$)$_3$•H$_2$O, 3 mmol NaOH, 3 mmol NH$_4$F, and 1 mmol CA was placed in a 20 mL Teflon inner vessel and transferred to a steel solvothermal reactor. The sample was placed in an oven and heated to 200 °C. Once the oven reached the reaction temperature, the sample was kept in the oven for 5 minutes, 3 hours, or 24 hours. The sample was cooled by placing the chamber in cold water. The final sample was washed similarly to those prepared by the coprecipitation method and described previously.

4.3 Results and Discussion

4.3.1 Laser ablation effects

Laser ablation of annealed samples in DI water reduced the particle size from micro- to nanometer and retained the favorable β-phase. Figure 4.1 presents an experimental scheme of our LAL setup, scanning electron microscopy (SEM) images of the pellet before and after annealing and a transmission electron microscopy (TEM) image of a sample produced by LAL. The size of particles in the pellet typically ranges from hundreds of nanometers to microns. After annealing, the particles were coalesced with a negligible change in the shape and size. Following LAL, they were converted to UCNPs which were < 10 nm in diameter. Figure 4.2 presents the x-ray diffraction (XRD) pattern, Raman spectra, and upconversion PL of the NaYF$_4$:Yb/Er powder before annealing, the NaYF$_4$:Yb/Er pellet after annealing at 400 °C, and the product after LAL at 50 mJ/pulse in DI H$_2$O. All upconversion PL spectra were collected using 980 nm continuous wave (CW)

excitation from a diode laser. Prior to annealing, the powder showed broad XRD peaks with a pattern like the α-phase, and the XRD peaks were relatively broad reflecting its polycrystallinity and small domains. Following annealing, the peaks became sharper, indicating improved crystallinity, and the pattern of peaks became more like the β-phase, suggesting some powder conversion from the α- to β-phase. Following LAL, the β- to α-phase ratio improved even further. The Raman spectra shows a similar trend. Prior to annealing, only two broad peaks were apparent at 275 and 740 cm^{-1}, which are associated with the α-phase.[106] The broad Raman peaks are due to defects and grain boundaries in the sample that reduce the lifetime of phonons. The sharp peak observed at 475 cm^{-1} is from the silicon wafer used to load the sample. Following the annealing step, several sharper peaks at 250, 305, 365, 490, and 625 cm^{-1} were observed, which are characteristic of the β-phase.[106] The sample obtained by LAL shows a similar pattern to that expected for the β-phase. The upconversion PL showed no emission prior to annealing but green and red emission after the annealing step, with the green emission being favored. After LAL, a similar PL spectrum was observed with slightly lower intensity. Despite the higher β- to α-phase ratio, the lower PL intensity is expected since bulk $NaYF_4$:Yb/Er generally has a higher upconversion efficiency due to a lower surface-to-volume ratio that protects it from surface quenching.[23]
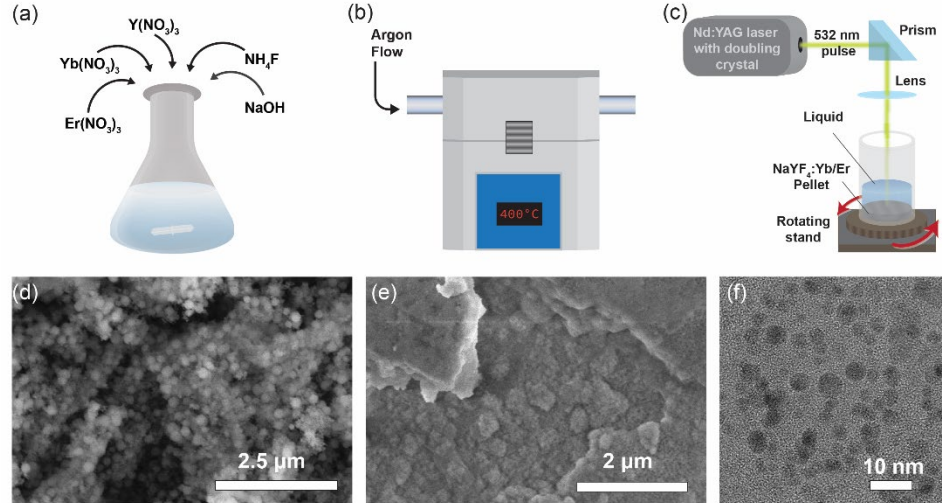
Figure 4.1 Experimental scheme of the various steps to prepare NaYF4:Yb/Er nanomaterials. The first step is the coprecipitation (a) to form a powder. The powder is pressed into a pellet and annealed under Ar flow in a tube furnace (b). The final step is LAL on the pellet (c). SEM images of the coprecipitate (d) and annealed powder (e) indicate minimal change in the shape and size of the pressed particles before and after annealing. TEM image after LAL (f) shows that the final product is significantly smaller in size than those after the previous steps.

4.3.2   Annealing temperature optimization

Before LAL was performed, influences of annealing temperature on the phases of pellets and upconversion PL were investigated. The optimized annealing temperature in terms of upconversion efficiency was determined to be 400 °C. To investigate the effects of annealing temperatures, several pellets were annealed at temperatures ranging from 200 to 800 °C. Figure 4.3a presents the XRD patterns of the pellets annealed at various temperatures along with references for both the α- and β-phases from the Crystallography Open Database.[234-235] Prior to any annealing, the sample showed a pattern similar to the α-phase. However, the peaks were very broad which suggests that it was mostly amorphous in nature. After annealing at 200 °C, the peaks became slightly narrower but still showed a pattern of the α-phase. After annealing at 300 °C, the peaks sharpened, indicating improved crystallinity based on the Debye-Scherrer equation.[106] Peaks associated with the

β-phase also appeared. As the temperature increased to 400 °C, the ratio of the β-to-α-phase improved. There was a slight improvement at 500 °C and a slight decrease after reaching 600 °C. At higher temperatures from 700 to 800 °C, the phase was completely converted back to the α-phase, which was expected because the β-to-α-phase transition of $NaYF_4$ occurs at 691 °C.[236] A similar trend was found in the Raman scattering, which is reported and discussed in the ESI (Figure S4.2). The upconversion PL of the pellets annealed at various temperatures is presented in Figure 4.3b. All PL band intensities were normalized to that of the 980 nm Rayleigh scattering to account for differences in sample concentration. An overlay of the PL from the coprecipitate and 200 °C annealed pellets magnified by 50 times is included to better show the PL variation as the annealing temperatures increase. Without any annealing, there was no observed upconversion PL. Following annealing at 200 °C, weak PL with favorable green emission appeared. In the 300-500 °C range, the PL intensity increased as the annealing temperature increased, which was expected from the observed increased β-to-α ratio. At 600 °C, the PL intensity started to decrease, with very weak PL observed at 700 °C. Finally, at 800 °C, the green emission was no longer favored, and the red PL became stronger. Although the samples annealed at 700 and 800 °C were converted back to the α-phase, they still showed better upconversion PL than the pre-annealed sample because of the better crystallinity. The SEM images of the annealed pellets at various temperatures are shown in Figure S4.3. Despite the observed changes in the crystal structure, negligible difference was observed in the morphologies of pellets. Moreover, energy dispersive x-ray spectroscopy (EDS) measurements (Figure S4.4) showed that the annealing temperature had a minimal impact on the elemental ratios of the pellets. The effect of annealing duration and XRD patterns (Figure S4.5) showed that annealing time had minimal influence on the crystal structure.
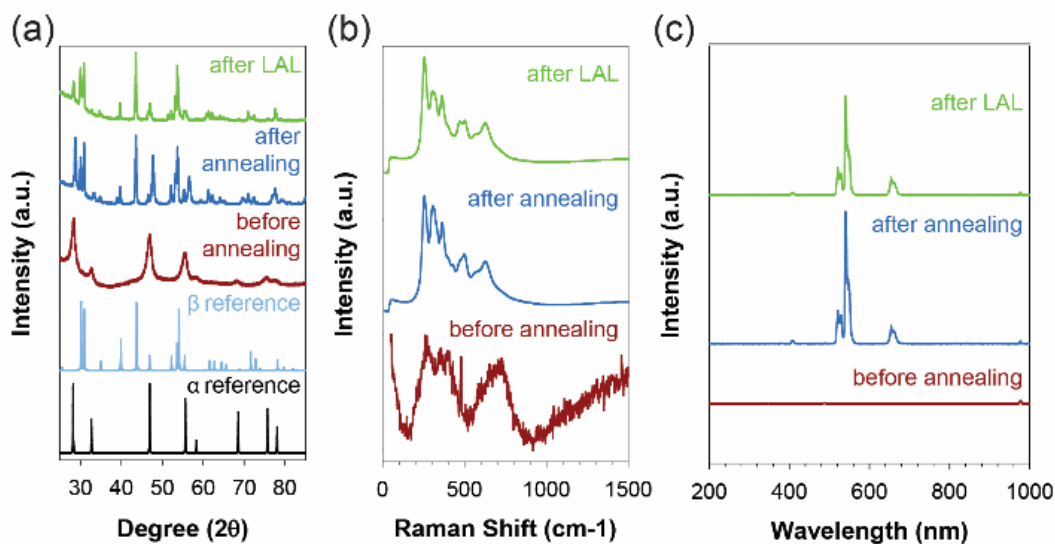
Figure 4.2 XRD patterns (a), Raman spectra (b), and upconversion PL collected with 980 nm CW laser excitation (c) of samples before annealing (red), after annealing at 400 °C (blue) and after LAL (green). Reference XRD patterns for the α-phase (black) and β-phase (light blue) were obtained from the Crystallography Open Database.[234-235]
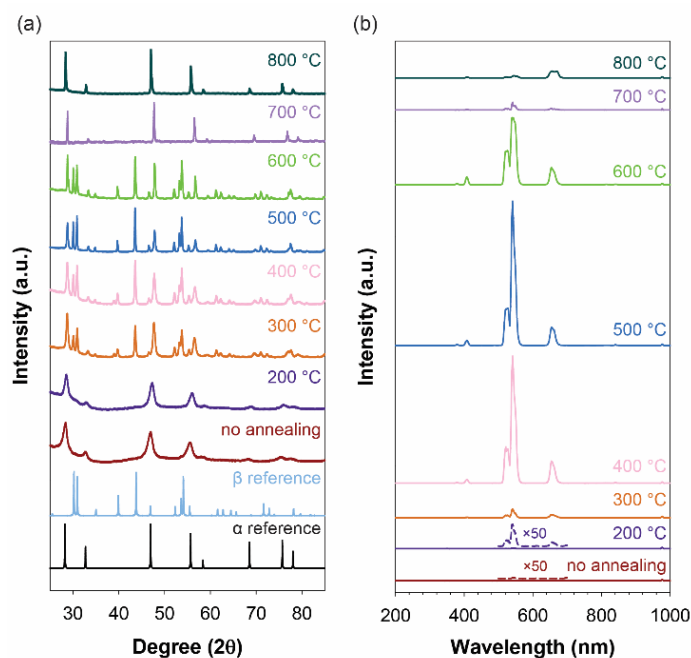
Figure 4.3 XRD patterns of the pellets annealed at various temperatures and the α- and β-phases (a), and upconversion PL of the different pellets collected at 980 nm excitation. Reference XRD patterns for the α-phase (black) and β-phase (light blue) were obtained from the Crystallography Open Database.[234-235]

122

4.3.3   Influence of capping agent

LAL of pellets annealed at 400 °C was done with a laser energy of 90 mJ/pulse (5.09 J/cm^2) in the presence of CA with concentrations of 0, 0.2, 2 , and 20 mg/mL, termed LAL-bare, LAL-CA-0.2, LAL-CA-2, and LAL-CA-20, respectively. Figure 4.4 shows the upconversion PL spectra of the LAL-bare and -CA samples (a) and the LAL samples with PEG concentrations of 0.2 mg/mL (LAL-PEG-0.2), 2 mg/mL (LAL-PEG-2), and 20 mg/mL (LAL-PEG-20) (b). All emission spectra showed similar spectral shapes with stronger green emission peaks at 525 and 545 nm and a weaker red emission peak at 660 nm, and a very weak blue peak at ~ 410 nm The LAL-CA samples showed similar emission intensities at all three concentrations, but the LAL-PEG-20 sample showed stronger emission over the LAL-PEG-0.2 and LAL-PEG-2 samples. To better understand how the capping agent influenced the PL properties, the green-to-red area ratios (I_g/I_r) for all the samples were calculated. Time correlated single photon counting (TCSPC) measurements were also collected at 980 nm excitation and emissions at 525 nm, 545 nm, and 660 nm. All samples were fit to a two-exponential that included both rising and decay components. Figure 4.4b shows the TCSPC decays and their fits for LAL-CA-20, and the I_g/I_r ratios and the rising and decay lifetimes for all the samples are summarized in Table 4.1.

The LAL-bare UCNPs had the lowest I_g/I_r ratio among all the samples. This can be attributed to surface passivation from the capping agents reducing quenching of the green bands at the surface by solvent water molecules. For the LAL-CA samples, however, the I_g/I_r ratio decreased as the concentration increased. The LAL-PEG samples showed the opposite trend, though there was less change in ratio compared to the LAL-CA samples. The TCSPC gives further information regarding the PL properties. In general, the decays for the LAL-bare UCNPs were slower than all the LAL samples produced in the presence of a capping agent. For LAL-CA the 525 nm τ_{decay} became slightly faster with increasing

CA concentration while the τ_{rise} component became slightly slower. At 545 nm, the τ_{decay} fluctuated; however, the τ_{rise} component also became slower. On the other hand, the 660 nm band had the opposite trend to the 525 nm band, with a τ_{rise} becoming faster with increasing concentration and a τ_{decay} being slower. The changes of both rise and decay times for the green emission bands were much smaller (<20 ns) compared to the changes observed in the red bands (>100 ns). Based on these results, we can conclude that for a particular emission band, as the rise time became longer, the decay time became shorter and vice versa, and the red (660 nm) band had larger changes compared to the green bands (525 and 545 nm). The faster rise time for the 660 nm band as the I_g/I_r ratio decreases and the CA concentration increases can be attributed to a greater amount of non-radiative transitions of the green bands to populate the red band. This likely originates from surface quenching from the capping agent. The LAL-PEG samples had much lower dependence on the PEG concentration. However, the green bands had significantly faster decay times (>100 ns) when compared to the LAL-bare and -CA samples. The red bands, on the other hand, were comparable to the LAL-bare and -CA samples. The different behaviors in PL of the CA and PEG with increasing concentration can be understood by considering the vibrational spectra of the two capping agents. Figure S4.6 shows the Fourier transform infrared spectroscopy (FT-IR) of CA, PEG, and the DI water solvent. The non-radiative $^4S_{3/2} \rightarrow {}^4F_{9/2}$ and $^4F_{9/2} \rightarrow {}^4I_{9/2}$ transitions of Er^{3+} are approximately 3000 cm^{-1} in energy.[110] If the surrounding ligands or solvent have vibrational bands overlapping with these Er^{3+} transitions, they can contribute to quenching of the activator ion.[110] CA has broad absorbance occurring at 3000 cm^{-1} which can contribute to the quenching. PEG, on the other hand, has a peak at 2890 cm^{-1} that does not overlap well with the Er^{3+} transitions. Therefore, increasing the PEG concentration has a minimal effect on the PL properties, while increasing the CA concentration both decreased the I_g/I_r ratio and influenced the PL lifetimes.
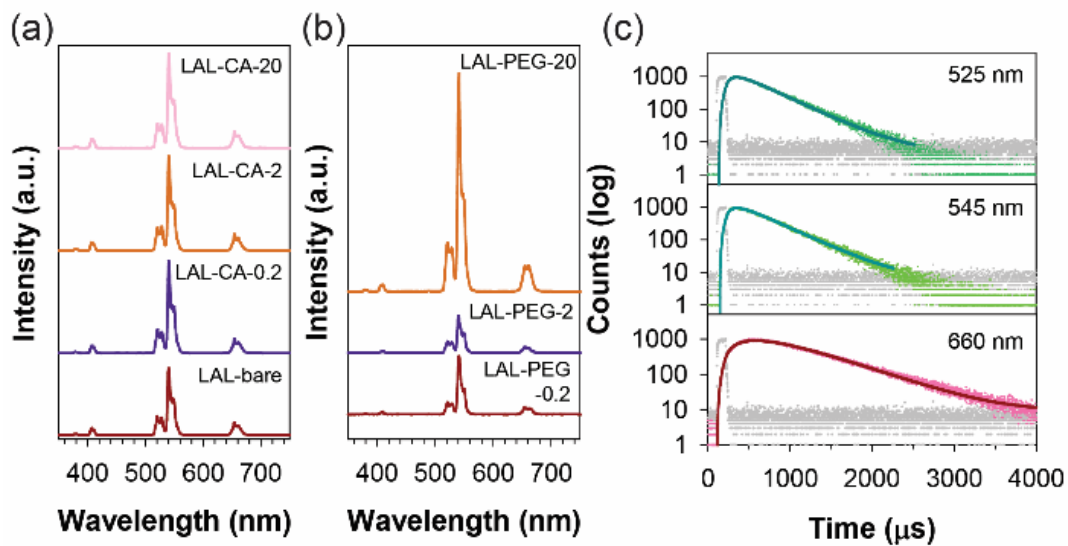
Figure 4.4 Upconversion PL of LAL samples prepared in water only and in the presence of various concentrations of CA (a), in various concentrations of PEG (b), and TCSPC measurements of the LAL-CA-20 sample at 525, 545, and 660 nm emission (c). All PL and TCSPC were collected with 980 nm excitation.

Table 4.1 Upconversion lifetimes and green to red emission intensity ratios of UCNPs prepared with various concentrations of capping agents. The LAL pulsed energy for preparing these samples was 90 mJ pulse-1 (5.09 J cm-1).

Sample description	I_g/I_r	$\lambda = 525$ nm		$\lambda = 545$ nm		$\lambda = 660$ nm	
		τ_{rise} (μs)	τ_{decay} (μs)	τ_{rise} (μs)	τ_{decay} (μs)	τ_{rise} (μs)	τ_{decay} (μs)
LAL-bare	5.4	84(2)	396.0(10)	90(2)	410.1(11)	273.1(15)	562(4)
LAL-CA-0.02	6	74(2)	384.5(11)	79(2)	375.2(12)	399(3)	418(3)
LAL-CA-2	5.7	83(2)	378.7(11)	80.3(12)	383.1(11)	248(2)	547(4)
LAL-CA-20	5.5	93(2)	371.5(11)	99(3)	379.6(11)	271.8(15)	522(4)
LAL-PEG-0.2	5.8	50.1(7)	251.7(7)	52.0(10)	247.9(8)	193(2)	530(2)
LAL-PEG-2	5.8	54.2(6)	259.6(7)	54.3(8)	249.3(8)	189(4)	498(5)
LAL-PEG-20	6	52.8(14)	248.0(10)	48.6(6)	261.6(6)	171(4)	501(3)
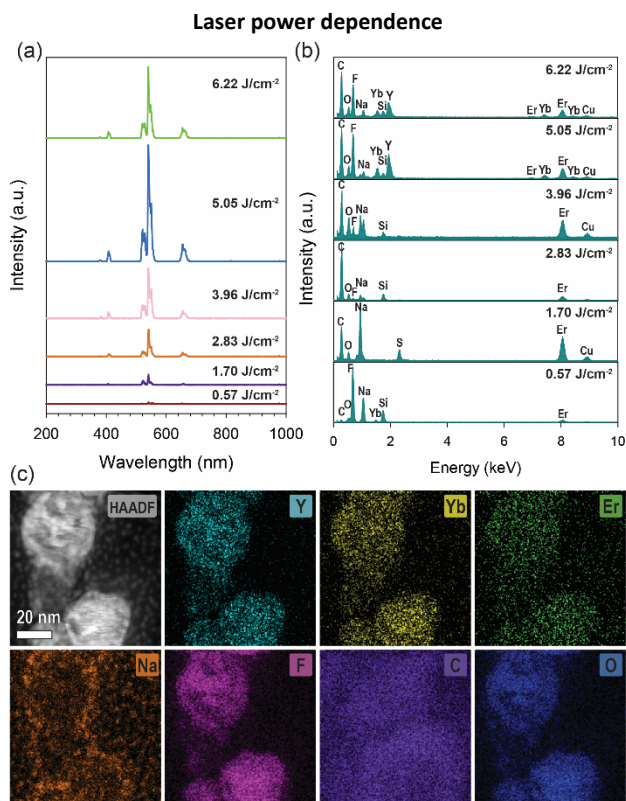
Figure 4.5 Upconversion PL of LAL-CA samples prepared at various laser energies (a), their EDS spectra (b), and a high-angle annular dark-field (HAADF) STEM image and EDS maps (c) for LAL-CA-20 sample prepared with 90 mJ/pulse.

Laser ablation power had a considerable influence on the PL properties and the elemental ratios of LAL-produced UCNPs. To investigate this, a laser pulsed energy (fluence) dependence ranging from 10 mJ/pulse (0.57 J/cm^2) to 110 mJ/pulse (6.22 J/cm^2) was done. All LAL experiments were conducted with the same laser beam size to avoid variations in production efficiency due to changes of ablation areas.[162] The TEM images of the samples produced at various laser pulse energies are presented in Figure S4.7. At low laser pulse energies, the size of the particles was large and non-uniform. As the fluence increased, the size of the particles started to decrease and became more uniform, which is consistent with previous reports.[164, 168] The upconversion PL, EDS spectra, and the high-angle annular dark-field (HAADF) scanning transmission electron microscopy (STEM)

image and EDS maps for the LA-NaYF4:Yb/Er sample prepared with 90 mJ/pulse (5.09 J/cm^2) are presented in Figure 4.5. The HAADF STEM images and EDS maps for the remaining power dependence samples are in Figs. S8-12. At very low laser fluence, the PL of the resultant sample was weak. As the fluence increased, so did the PL, and the sample produced with 90 mJ/pulse had the highest intensity. There was a slight decrease in upconversion PL when the laser pulse energy was increased to 110 mJ/pulse. This can be understood by considering the elemental compositions determined by EDS mapping. The calculated atomic percentages of Na, F, Y, Yb, and Er and the I_g/I_r ratios for the various samples are presented in Table 4.2, and additional data for C and O are presented Table S4.1.

At low laser fluence, only Na and F were observed in the EDS maps. As the laser fluence increased, so did the elemental ratios of Y, Yb, and Er. Surprisingly, at 1.7 J/cm^2, Er accounted for 18% of the elemental ratios while Y and Yb accounted for 3.9% and 2.7%, respectively. The observed amount of Er decreased as the laser fluence was further increased, while Y and Yb increased until 5.09 J/cm^2 with a slight decrease at 6.22 J/cm^2. When considering the total sum of Y, Yb, and Er, a total fraction of 16.7% is expected if the theoretical stoichiometric ratio is achieved. The samples obtained with 5.09 and 6.22 J/cm^2 were closest to this ratio with 18.2% and 17.5%, respectively. Table S4.2 presents the TCSPC lifetimes for the samples prepared at various laser pulsed energies. The PL for the sample prepared with 0.57 J/cm^2 was too weak to measure, and the red emission for the sample prepared at 1.70 J/cm^2 had a high uncertainty due to poor PL signal. In general, the decay times became faster as the laser fluence increased while the rise times became slower. Clearly, the laser parameters made a significant effect on particle composition and must be carefully considered when designing LAL experiments. At low laser fluences, the elements of the pellet were released individually and with varying efficiencies. Na and F were the only significant elements released at 0.57 J/cm^2. Er was released more efficiently than Y and Yb, as observed by the higher elemental ratio observed

at 1.70 J/cm^2. On the other hand, at higher laser fluences, the particles maintained the initial elemental ratio much better. At intermediate laser fluences, a mixed effect occurred, where some particles maintained the pellet compositions while others only included certain elements. This is consistent with a previous report that low laser fluences induced an evaporative phase changes where elements with lower heats of fusion and evaporation and with lower melting and boiling points escaped more readily. However, at higher laser fluences, the mechanism changed to explosive ejection and a majority of ablated material escaped.[167] Table S4.3 lists the melting points, boiling points, heats of fusion, and heats of vaporization for Na, F, Y, Yb, and Er. The thermodynamic values are all much lower for Na and F compared to Y, Yb, and Er, which explains why at low laser fluences they were the only observed elements present in the final product.[237-238] At high laser fluences, all of the elements were observed and their ratios became closer to the stoichiometric ratios of the target material. However, at intermediate fluences, the atomic percentage of Er was much higher than Y and Yb despite having heats of fusion/vaporization and melting/boiling temperatures that are comparable to or higher than those of Y and Yb.[237-238] This can be understood by considering the absorbance spectra of the Y^{3+}, Yb^{3+}, and Er^{3+} ions (Figure S4.13). Y^{3+} does not have any strong absorbance peaks in the 350-1000 nm region. Note that the strong peaks observed at 300 nm are from the nitrate counter ions in the solutions. Yb^{3+} on the other hand, only has a peak appearing at 980 nm, where the $^2F_{5/2} \leftarrow {}^2F_{7/2}$ transition occurs. Neither Y^{3+} nor Yb^{3+} shows any absorbance at 532 nm, the laser wavelength used for LAL. Er^{3+}, however, has many absorbance bands occurring in the 350-1000 nm range including near 532 nm. Since Er^{3+} can absorb the laser fluence more readily than Y^{3+} and Yb^{3+}, it will have a rise in temperature and be more likely to melt and evaporate at the surface.[168] This explains why at intermediate fluences the amount of Er was higher than that of Y and Yb, despite the lower amount present in the target material.

Table 4.2 Elemental ratios and green to red PL peak area ratios of samples prepared at varying laser fluences

Laser energy / fluence (mJ pulse^{-1} / J cm^{-2})	10 / 0.57	30 / 1.7	50 / 2.83	70 / 3.96	90 / 5.09	110 / 6.22	Theoretical
Na	26.2	66.1	52.6	61.9	5.5	10.9	16.7
F	73.7	9.1	41.3	32.2	76.2	71.6	66.7
Y	0.1	3.9	0.5	1.2	14.5	13.9	13.3
Yb	0	2.7	0.5	0.6	2.3	2.5	2.8
Er	0	18.2	5.2	4.1	1.5	1.2	0.5
I_g/I_r	2.3	6.0	5.7	6.3	6.2	5.4	-

Table 4.3 Green-to-red PL peak area ratios and upconversion lifetimes for the solvothermally synthesized samples.

Solvothermal time	I_g/I_r	$\lambda = 525$ nm			$\lambda = 545$ nm			$\lambda = 660$ nm		
		τ_{rise} (μs)	τ_1 (μs)	τ_2 (μs)	τ_{rise} (μs)	τ_1 (μs)	τ_2 (μs)	τ_{rise} (μs)	τ_1 (μs)	τ_2 (μs)
5 minutes	1.9	3.3(8)	0.2(7)	79.3(6)	110(14)	50(3)	500(300)	49(3)	50(10)	219(5)
3 hours	3.0	27.3(15)	112(6)	315(2)	27.3(9)	118(5)	314(2)	147(5)	150(20)	483(3)
24 hours	3.0	28.3(9)	110(5)	283(2)	29.3(9)	115(5)	289(3)	98(15)	135(9)	492(14)

4.3.4 Solvothermal comparison

For comparison, samples were also prepared via a traditional solvothermal method based on literature.[106] Samples were heated in an oven and allowed to remain at 200 °C for 5 minutes, 3 hours, and 24 hours. The XRD patterns of these samples are reported in Figure 4.6a. The 5-minute reaction showed the presence of only the α-phase. The 3-hour and 24-hour reactions showed only the presence of the β-phase as well as narrower peaks, indicating improved crystallinity. The upconversion PL spectra (Figure 4.6b) showed very weak PL after 5 minutes but increased after increasing the reaction time to 3 and 24 hours. The SEM images indicate that the reaction time greatly affected the particle size and morphology (Figure 4.6c); however, all products were on the micrometer size scale. The samples that were heated for 24 hours produced hexagonal rod-shaped structures with jagged ends and fairly irregular sizes ranging from 2 to 22 μm in length. The samples that were heated for 3 hours showed hexagonal structures that were shorter in length compared to the 24-hour sample and were much more uniform in both shape and size with rod lengths ranging from 1.5 to 5 μm. Both the 24- and 3-hour samples also had small particles present on the surface of some of the rods. The sample that was heated for 5 minutes was comparatively more irregular with both small and large particles having no uniform shapes observed. We expect that the limited reaction time was insufficient for the formation of an ordered structure. While the solvothermal method at 3- and 24-hour reaction times allowed for preparation of samples that were completely hexagonal in nature and had high upconversion PL efficiency, it did not result in the formation of desirable nanoscaled materials. EDS (Figure S4.14) showed that the solvothermal reaction time had minimal influence on the sample composition.

The I_g/I_r ratios and TCSPC measurements of the solvothermal samples were also considered and are presented in Table 4.3. All three samples had lower I_g/I_r than the LAL samples. Another notable difference is the TCSPC decays best fit to three exponentials

(one rise and two decays), unlike the LAL samples that fit to two (one rise and one decay). The lifetimes for the 5-minute sample had large uncertainties due to the weak PL. The rise times for the 3- and 24- hour samples were notably faster than the LAL samples. Each component had two decays which likely arise from having bulk and surface states. The surface states will be much more susceptible to PL quenching and thus will have faster decays. The bulk states, on the other hand, are passivated by the surface states and protected from solvent effects.

One area to consider when doing solvothermal synthesis is the possibility of the degradation of various reagents that are present, such as the CA capping agent. It is well established that CA can be used as a reagent to form carbon dots via solvothermal methods.[32] We therefore investigated the PL properties of the hydrothermal samples, their supernatants obtained during purification, and CA only in water before and after solvothermal treatment. Samples were excited at various visible excitation wavelengths and their PL is reported in Figure S4.15. Both the 3- and 12- hour samples showed PL with 390 and 420 nm excitation, but the 5-minute sample did not show any PL (the sharp, excitation dependent peaks observed in several of the spectra are due to water Raman scattering from the solvent). However, the supernatants for all three samples had strong PL with 330 and 360 nm excitation, similar to the PL that was observed for carbon dots.[68] This suggests that a strongly emissive by-product was formed during solvothermal synthesis. CA only had no PL before solvothermal treatment, but after solvothermal treatment it had similar PL to the supernatants. Finally, a LAL sample produced with CA in the liquid was also measured and showed no PL properties. These results suggest that solvothermal synthesis is not suitable for in-situ coating of upconverting materials because the harsh conditions induced side reactions with the capping agents. LAL, however, did not show the emergence of any PL and is therefore a suitable method to directly cap UCNPs.
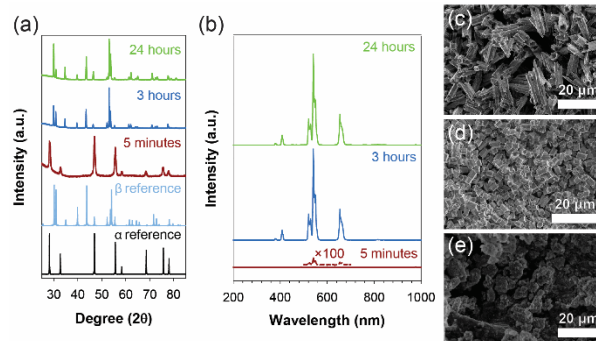
Figure 4.6 XRD patterns (a) and upconversion PL normalized at 980 nm (b) for solvothermally synthesized NaYF4:Yb/Er samples 5-minute (red), 3- hour (blue) and 24-hour (green) reaction times. The α- and β- reference XRD patterns are shown in black and light blue, respectfully. SEM images for the 24-hour (c), 3-hour (d) and 5- minute (e) reaction times indicate a time dependence on sample size and morphology. Reference XRD patterns for α-phase (black) and β-phase (light blue) were obtained from the Crystallography Open Database.[234-235]

4.4   Conclusion

In conclusion, we have successfully implemented LAL as a viable approach to convert bulk NaYF4:Yb/Er material into UCNPs that were stable in water. This method allowed for the formation of bare UCNPs and for the simultaneous coating of the UCNPs with water soluble ligands. Addition of CA and PEG capping agents allowed for surface passivation of the UCNPs and increased I_g/I_r ratios. The PL properties of the samples prepared with CA were more sensitive to concentration effects than those prepared with PEG due to greater vibrational energy overlap of the CA with the Er^{3+} transition energies. This method offers the advantage over other strategies to modify the surface such as ligand stripping in that it does not require extra chemicals or purifications to remove the ligands. The laser fluence had a considerable effect on the final product morphology and composition. At low laser fluence, the UCNPs consisted of mainly large particles that mostly contained Na and F. As the power increased, the particles became more uniform while also allowing UCNP formation with compositions that more closely resembled the bulk target material. These observations allowed a better insight into the LAL mechanism

133

where low fluences favored a thermal evaporation mechanism, while high fluences favored an explosive ejection mechanism. Finally, compared to the more commonly used solvothermal method, LAL produced smaller particles and no side products with the capping agent. Future work will aim to produce a LAL target that is completely hexagonal in phase and to further size refine the sample. Other factors such as laser wavelength and ablation time can affect the LAL mechanism[164] and should also be explored to better understand the UCNP formation process.

4.5   Supporting Information

4.5.1   Experimental Details

4.5.1.1   Materials Used

Yttrium (III) nitrate hexahydrate (99.9% REO), ytterbium (III) nitrate hydrate (99.9% REO), erbium (III) nitrate hydrate (99.9% REO), and ammonium fluoride (ACS, 98.0% min) were purchases from Alfa Aesar. Sodium hydroxide (99%) was purchased from Mallinckrodt AR®. Citric acid (≥97%) and poly(ethylene glycol) diamine (PEG) (average M_n=3000) were purchased from Sigma Aldrich. Reagent alcohol (ACS grade) was obtained from WVR Chemicals BDH. All chemicals were used without further purification. Deionized water was obtained using a Barnstead™ E-Pure™ Ultrapure Water Purification System.

4.5.1.2   Characterization Details.

4.5.1.2.1 PHOTOLUMINESCENCE (PL) MEASUREMENTS

PL measurements were obtained with a Horiba Scientific Fluoromax Plus-C equipped with an external 980 nm diode laser (Lasever Inc.) as the excitation source. During a typical upconversion PL measurement, the integration time was 0.1 s, and the exit slit was 1.5 nm. The 980 nm diode laser was operated in continuous wave (CW) mode at 2 W. For visible excitation measurements, samples were excited with the instrument's Xe arc lamp. For lifetime measurements the diode laser was configured to operate in pulsed mode using a DeltaHub™ high throughput time correlated single photon counting (TCSPC) controller. A typical lifetime measurement used a scan range of 2.7 ms, a repetition rate of 350 Hz , an average power of 2 W, and a bandpass of 10 nm. Decays were collected at 525, 545, and 660 nm emission. The instrument response function (IRF) was measured at 980 nm using a ludox solution. Lifetime fits were obtained using the Horiba Scientific decay analysis software DAS6.

4.5.1.2.2 SCANNING ELECTRON MICROSCOPY (SEM) MEASUREMENTS

SEM images were obtained using a Hitachi S-4300 Scanning Electron Microscope.

4.5.1.2.3 TRANSMISSION ELECTRON MICROSCOPY (TEM)

Samples were prepared for TEM by drop casting a 10 μL aliquot of solution on Lacey carbon 300-mesh copper grids. Images were obtained with a Thermo Scientific Talos F200X scanning/transmission electron microscope. Samples were analyzed in both TEM mode and STEM mode for EDS mapping.

4.5.1.2.4 RAMAN

Raman spectra were collected using a Thermo Scientific DXR Raman Microscope using a 10× objective, 532 nm excitation source, and an excitation power of 0.1 mW.

4.5.1.2.5 X-RAY DIFFRACTION (XRD)

XRD measurements were obtained using a Bruker D8 Advance instrument using a Cu K$_\alpha$ x-ray source.

4.5.1.2.6 FOURIER TRANSFORM INFRARED SPECTROSCOPY (FT-IR)

FT-IR measurements were collected on a Thermo Scientific Nicolet™ iS50 FT-IR Spectrometer. All samples were analyzed using a diamond attenuated total reflectance (ATR) plate.

4.5.1.2.7 ABSORBANCE

Absorbance measurements were collected on a Thermo Scientific Evolution™ 201 UV-Visible Spectrophotometer.

4.5.1.2.8 EDS

EDS for the annealed pellets and hydrothermal samples was collected with a Hitachi TM3000 TableTop Scanning Electron Microscope equipped with a SwiftED 3000 EDS detector.

4.5.2 Upconversion Mechanism
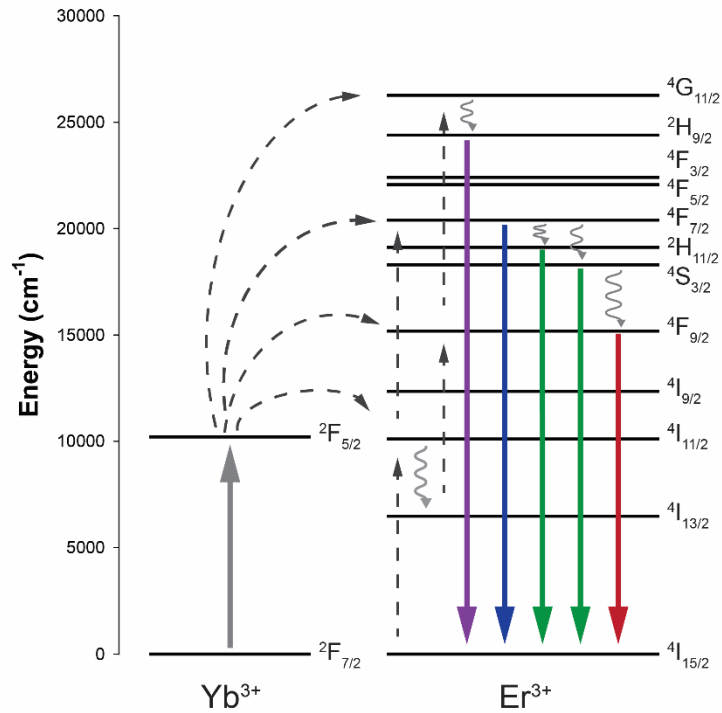
Figure S4.1 Energy transfer upconversion mechanism typical for a NaYF4:Yb/Er UCNP. The energy levels were acquired from the NIST atomic spectra database, and all terms have odd parity.[230] In this mechanism, Yb3+ and Er3+ atoms are hosted in an optically transparent NaYF4 host lattice. Yb3+ acts as a photosensitizer and absorbs 980 nm light. Yb3+ then transfers its energy to a nearby activator Er3+. Since Er3+ has excited states with long lifetimes, multiple energy transfers can occur prior to emitting a photon, allowing for upconversion to occur. The strongest emission bands originate from the 4F9/2 → 4I15/2 (660 nm), 4S3/2 → 4I15/2 (545 nm), and 2H11/2 → 4I15/2 (525 nm) transitions. Due to the multiple transition from Yb3+ to Er3+ necessary for upconversion to occur, the concentration of Yb3+ is typically much higher than that of Er3+.[82]

4.5.3 Annealing temperature and time dependence

4.5.3.1 Raman Spectra
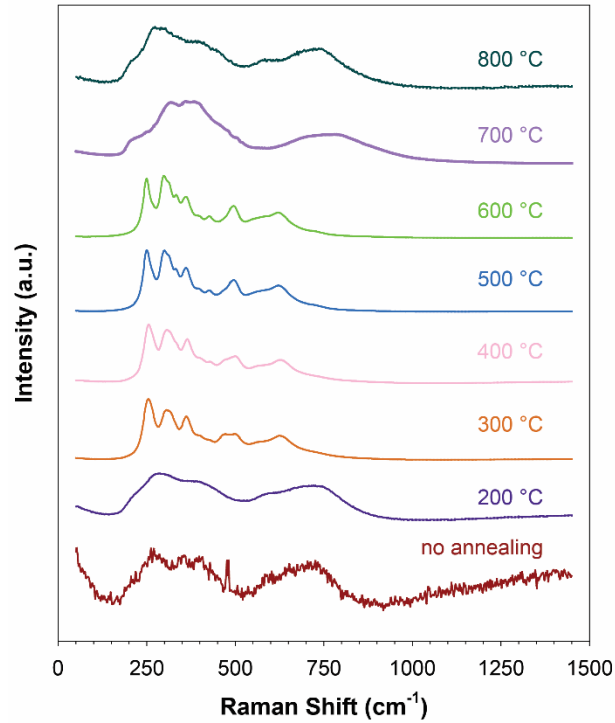
Figure S4.2 Raman spectra of NaYF$_4$:Yb/Er pellets annealed at various temperatures. The spectrum collected prior to annealing shows peaks similar to the α-phase. The low signal-to-noise is due to poor crystallinity and the sharp peak at 475 cm-1 is from the silicon wafer background used to load the sample. At 200 °C the sample still shows presence of the α-phase. A stretching characteristic of hexagonal structure is observed after 300 °C. Finally, after 700 °C, the structure is converted back to cubic structure. All spectra were collected using 0.1 mW laser excitation.

4.5.3.2   SEM Images
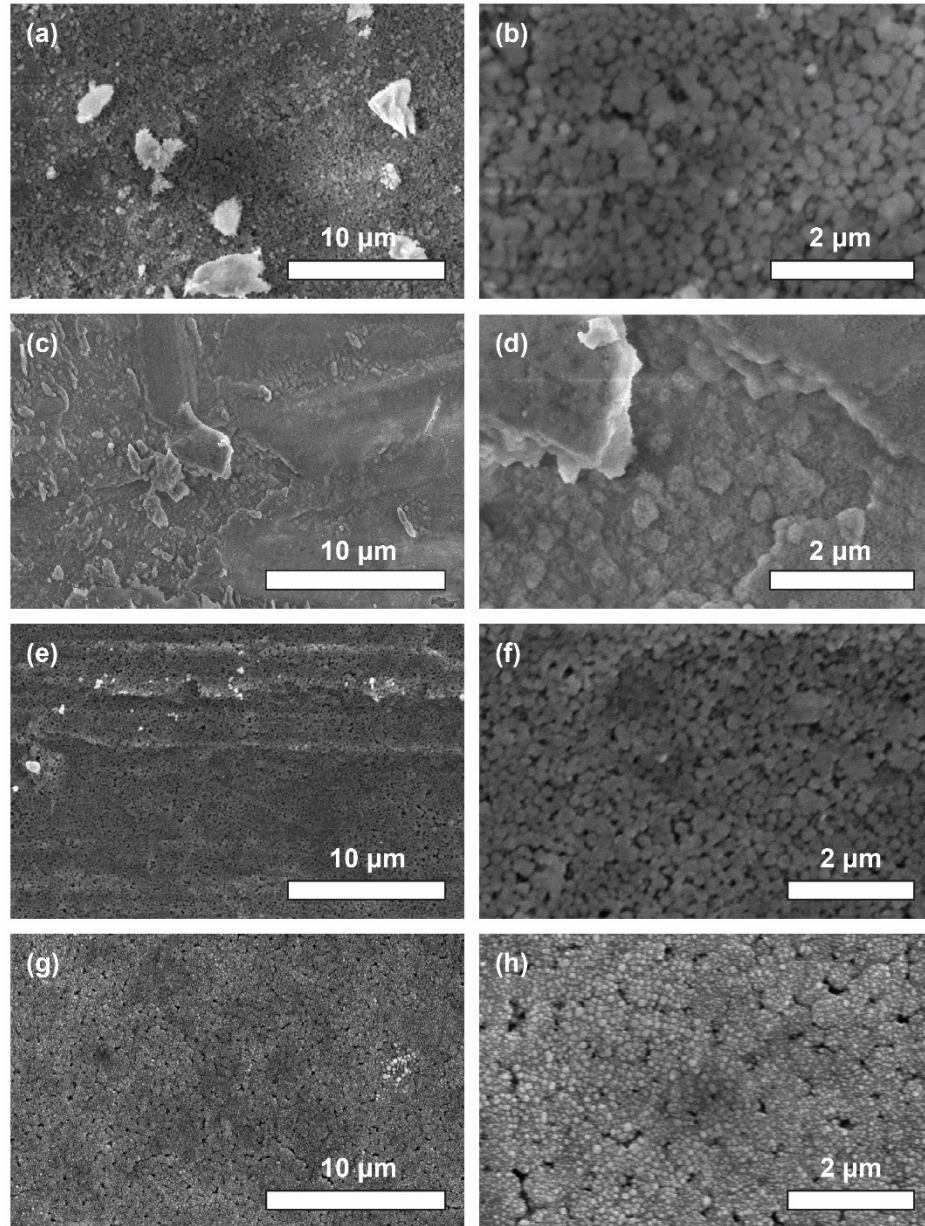
Figure S4.3 SEM of NaYF$_4$:Yb/Er pellets annealed at 200 °C (a-b), 400 °C (c-d), 600 °C (e-f), and 800 °C (g-h). The pellets show no differences in the microstructure with the various annealing temperatures.

4.5.3.3 Elemental ratios from EDS
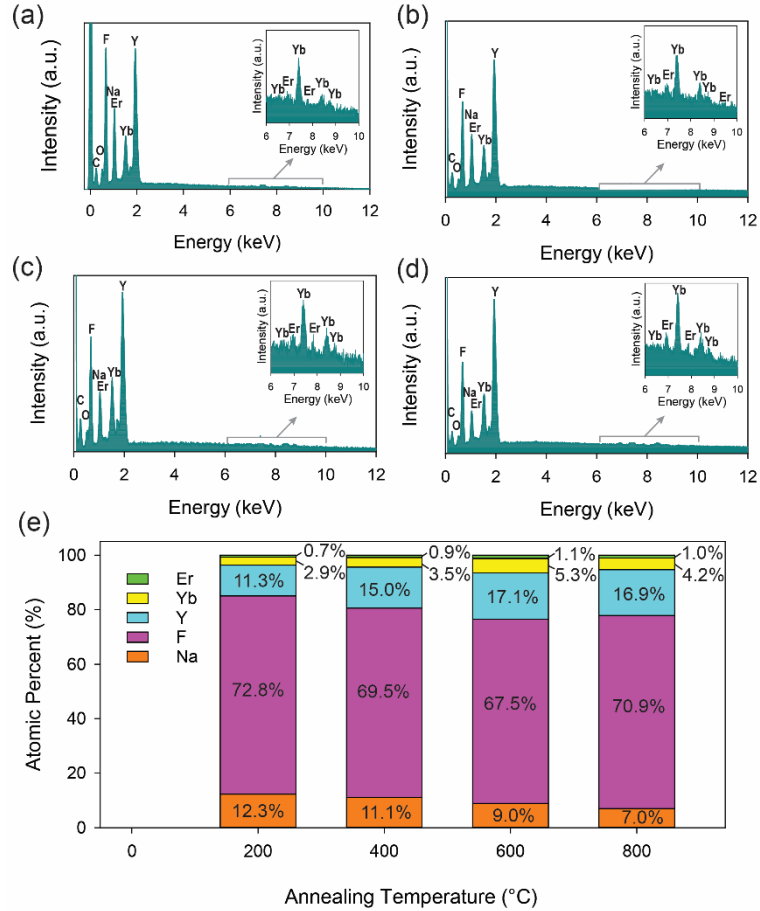
Figure S4.4 EDS of NaYF₄:Yb/Er pellets annealed at 200 °C (a), 400 °C (b) 600 °C (c) and 800 °C (d) and a graph of the atomic percentages for various NaYF4:Yb/Er pellets. Annealing temperature resulted in a slight decrease in Na content and increase in the total rare earth metal content in the pellet.

4.5.3.4 Annealing time dependence XRD
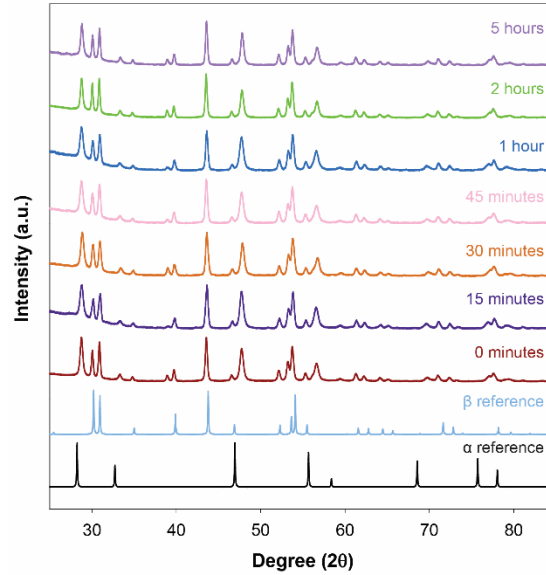
Figure S4.5 XRD of NaYF$_4$:Yb/Er pellets annealed at 400 °C for various amounts of time. The annealing time had minimal influence over the ratio of β and α phases. Reference XRD for α-phase (black) and β-phase (light blue) were obtained from the Crystallography Open Database.[234-235]

4.5.4 LAL Samples

4.5.4.1 FT-IR of capping agents and solvent
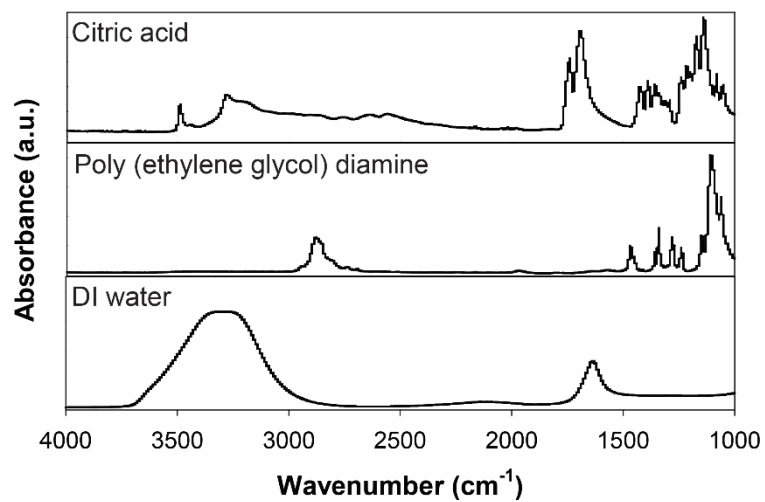
Figure S4.6 FT-IR of citric acid (top), poly (ethylene glycol) diamine (center) and deionized water (bottom). Citric acid shows absorbance peaks at 3000 cm^{-1} while poly (ethylene glycol) diamine shows minimal absorbance at this energy.

4.5.4.2 Power Dependence TEM
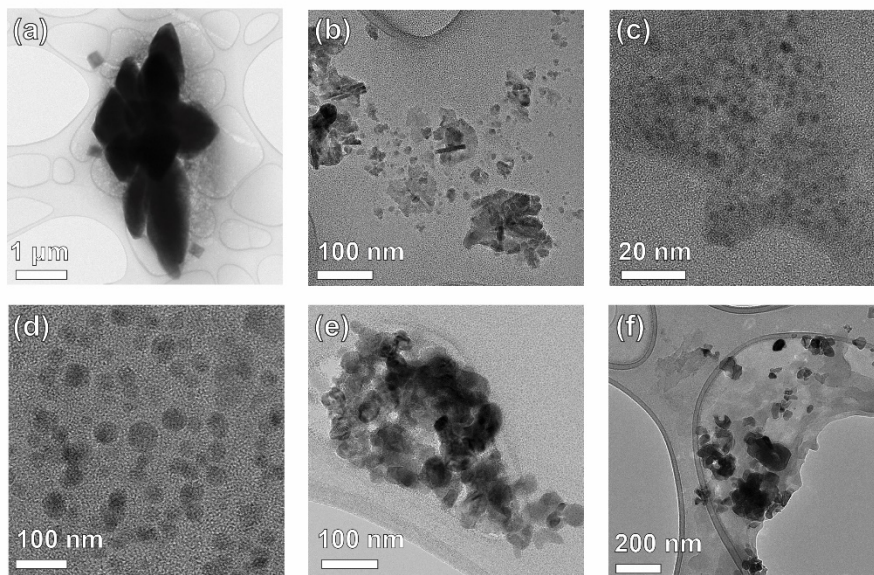
Figure S4.7 TEM of LAL-CA-20 samples prepared with 10 mJ/pulse (a), 30 mJ/pulse (b), 50 mJ/pulse (c), 70 mJ/pulse (d), 90 mJ/pulse (e), and 110 mJ/pulse (f). At low laser powers the size of the particles is large and non-uniform. As laser power increases, particles become smaller and more regular in size.

4.5.4.3 EDS Maps

Table S4.1 Elemental ratios acquired from STEM-EDS mapping of various LAL-CA-20 samples produced at different laser fluences

Laser energy/fluence (mJ pulse^{-1}/J cm^{-2})	10 / 0.57	30 / 1.7	50 / 2.83	70 / 3.96	90 / 5.09	110 / 6.22
C	4.7	82.4	90.6	65.8	75.2	59.3
O	5.7	5.8	5.9	16.1	5	7.8
Na	23.5	7.8	1.9	11.2	1.1	3.6
F	66.1	1.1	1.5	5.9	15.1	23.6
Y	0.1	0.5	0	0.2	2.9	4.6
Yb	0	0.3	0	0.1	0.5	0.8
Er	0	2.1	0.2	0.7	0.3	0.4
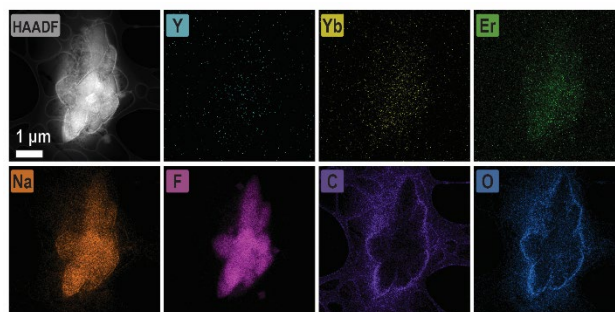
Figure S4.8 High-angle annular dark-field (HAADF) STEM image and EDS maps for LAL-CA-20 sample prepared with 10 mJ/pulse
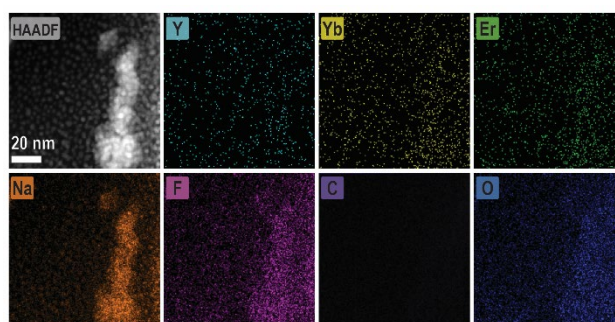
Figure S4.9 HAADF STEM image and EDS maps for LAL-CA-20 sample prepared with 30 mJ/pulse
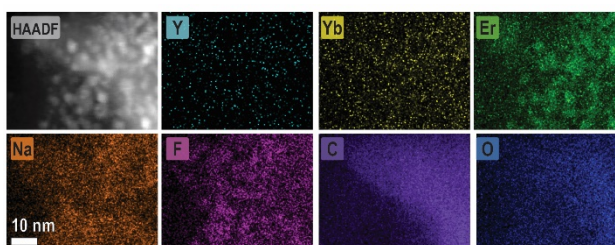
Figure S4.10 HAADF STEM image and EDS maps for LAL-CA-20 sample prepared with 50 mJ/pulse
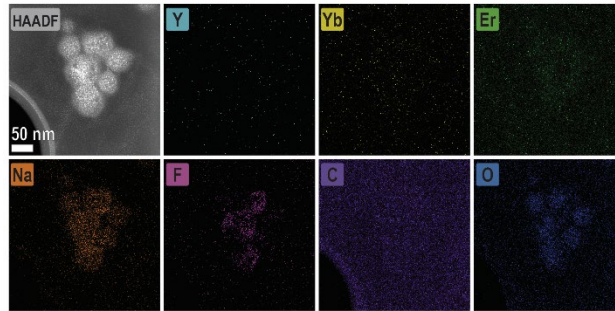
Figure S4.11 HAADF STEM image and EDS maps for LAL-CA-20sample prepared with 70 mJ/pulse
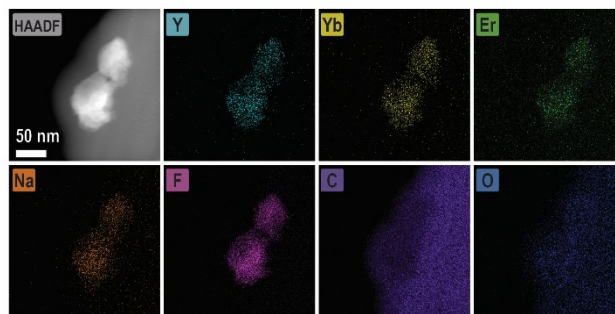
Figure S4.12 HAADF STEM image and EDS maps for LAL-CA-20 sample prepared with 110 mJ/pulse

4.5.4.4 Power dependence lifetime

Table S4.2 Upconversion rise and decay lifetimes for the LAL-CA-20 power dependent samples.

Laser energy/fluence (mJ pulse^{-1}/J cm^{-2})	$\lambda = 525$ nm		$\lambda = 545$ nm		$\lambda = 660$ nm	
	τ_{rise} (μs)	τ_{decay} (μs)	τ_{rise} (μs)	τ_{decay} (μs)	τ_{rise} (μs)	τ_{decay} (μs)
10 / 0.57	-	-	-	-	-	-
30 / 1.7	60.9(13)	471(3)	67(4)	441(5)	680(90)	700(200)
50 / 2.83	94.7(9)	396.6(12)	100.0(10)	389.2(12)	467(5)	470(20)
70 / 3.96	101.4(11)	405(13)	103.16(10)	401.4(13)	460(3)	483.4(11)
90 / 5.09	124(2)	350.51(10)	85.5(8)	424.8(8)	442(2)	445(9)
110 / 6.22	112(2)	359.6(1)	117(2)	352.78(10)	432(4)	430(20)

4.5.4.5 Thermodynamics values

Table S4.3 Melting points, boiling points, enthalpies of fusion and vaporization for the various of the atoms in LAL target according to the CRC handbook[237] and Zhang et al.[238]

Element	Melting Point (°C)	Boiling Point (°C)	$\Delta_{fus}H$ (kJ mol^{-1})	$\Delta_{vap}H$(kJ mol^{-1})
Na	97.794	882.940	2.60	97.4
F	-219.67	-188.11	0.51	6.32
Y	1522	3345	11.4	390
Yb	824	1196	7.66	159
Er	1529	2868	19.9	280

4.5.4.6 Absorbance of the rare earth metals
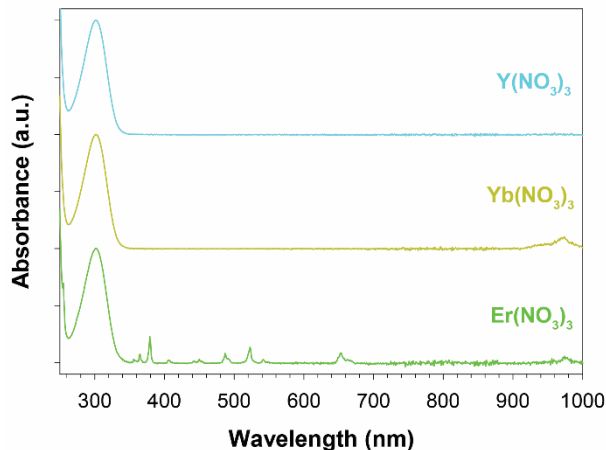
Figure S4.13 Absorbance spectra of precursor metals sources. The peak at 300 nm is due to the NO_3^- counterion. Y^{3+} shows no absorbance in the spectra region of interest. Yb^{3+} only shows absorbance at 980 nm. Er^{3+} has well defined absorbance in the visible and near-infrared including around 532 nm.

4.5.5 Solvothermal samples

4.5.5.1 Elemental composition from EDS
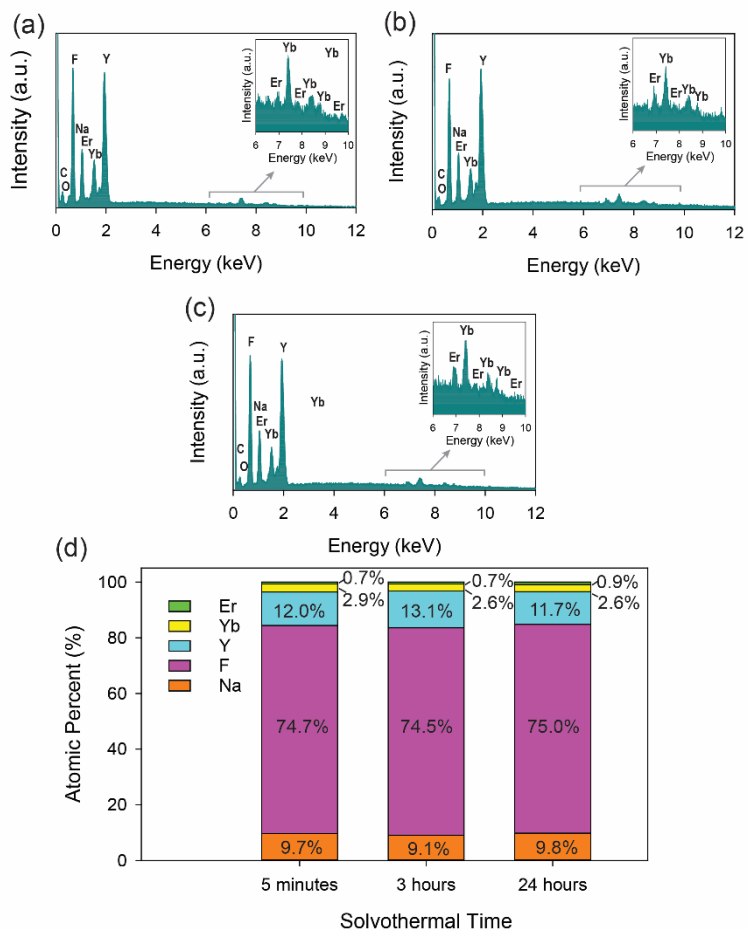
Figure S4.14 EDS of solvothermal samples heated at 200°C for 5 minutes (a), 3 hours (b), and 24 hours (c) and a graph showing their atomic percentages (d). The solvothermal heating parameters had minimal influence on the elemental ratios.

4.5.5.2 PL characterization
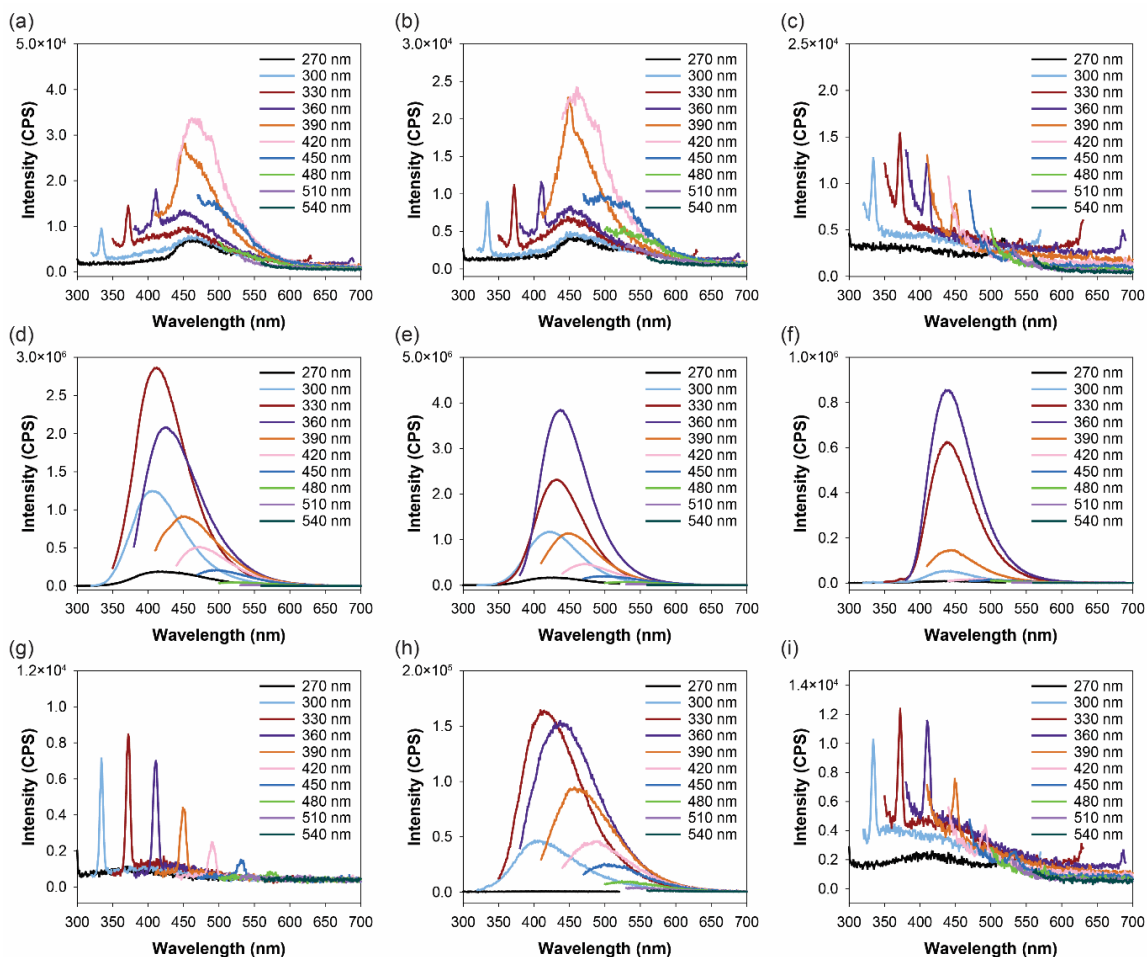
Figure S4.15 PL spectra collected at various excitation wavelengths for the hydrothermally prepared NaYF$_4$:Yb/Er samples heated for 24 hours (a), 3 hours (b), and 5 minutes (c), for the supernatants of the hydrothermally prepared samples heated for 24 hours (d), 3 hours (e), and 5 minutes (f), and for a citric acid solution (g), hydrothermally treated citric acid (h), and for the LA-NaYF$_4$:Yb/Er sample prepared with 90 mJ/pulse (i). The legend indicates the excitation wavelength used.

Laser ablation in liquid has been proven as a fast, clean, and efficient alternative method to produce interesting photoluminescent nanomaterials including graphene quantum dots and upconverting nanoparticles. A systematic comparison of GQDs produced through both a traditional chemical oxidation method and LAL using CNOs as a precursor showed that the samples produced by LAL had a blue shifted PL which is attributed to the effects of both particle sizes and surface functional groups. The GQDs produced from LAL were smaller in size and more uniform with an average diameter of 1.8(6) nm and a thickness comparable to a single layer of graphene, while the GQDs produced by the chemical oxidation method resulted in particles that had an average diameter of 4.1(8) nm and a thickness corresponding to two or three graphene layers. The LAL prepared samples favored the presence of hydroxyl groups and had a higher fraction of sp^3 carbon which implied less ordered intrinsic states. The chemical oxidation samples favored the presence of carboxylic groups and had a higher fraction of sp^2 carbon domains, implying that GQDs maintained the ordered graphitic structure of the CNO precursor. While previous studies to produce chemically reduced GQDs required additional steps after the initial chemical oxidation which was both costly in time, materials, and overall product yield, the LAL method allowed direct formation of reduced GQDs. TCSPC measurements showed that the particles had three emissive pathways as shown by their tri-exponential fits. The fastest lifetime component was attributed to intrinsic, bandgap states while the intermediate and slowest components were attributed to molecule-like states from the surface functional groups. Comparisons of the samples prepared by the two methods gave evidence that the longer lifetime component was associated with the more oxidized, carboxylic groups and green emission while the intermediate component was more closely related to the hydroxyl groups and blue emission. This was consistent with previous reports that suggested that higher degrees of oxidation resulted in red shifted emission and longer

lifetimes. The TCPSC data also suggested that the surface functional groups are the main source of radiative deactivation and the sp^2 carbon domains are mainly responsible for non-radiative decay. The large fraction of sp^3 carbon and high percentage of hydroxyl groups gave evidence that the thermal decomposition mechanism was the method of GQD formation during LAL. This systematic comparison with the GQDs produced through chemical oxidation proved that LAL is a faster and cleaner, single-step method to produce GQDs that used fewer starting chemicals, produced fewer byproducts, and required only simple purification steps.

This work was expanded to explore the possibility of heteroatom doping using the LAL method. Nitrogen doped GQDs were prepared from CNOs using aqueous solutions of ammonia, ethylenediamine, and pyridine as dopants. The choice of these dopants allowed for tuning of the overall nitrogen content and the distribution of functional groups which allowed control over the photoluminescence emission wavelengths and lifetimes. High concentrations of amine groups tended to favor a red shifted emission with shorter PL lifetimes ranging from 3-4 ns, whereas pyridinic groups favored a blue shifted emission that had longer lifetimes ranging from 9-13 ns. These samples were also tested for catalytic activity for the oxygen reduction reaction and showed promising performance as electrocatalysts for the 2-electorn reduction of oxygen to form peroxide, an important chemical in many industrial, medicinal, and chemical applications. However, one limitation of these GQDs for catalysis applications was their high degree of water solubility which required a binder to attach them to the electrode during electrocatalysis which increased the electrical resistance.

The versatility of the LAL method to form many types of nanomaterials was then demonstrated by exploring it as an alternative method to produce $NaYF_4$:Yb/Er based UCNPs. A bulk precursor was produced through coprecipitation and was annealed under argon flow to improve both the crystallinity and upconversion efficiency. The precursor was then used as the target during LAL to convert it to UCNPs. The strategy of annealing

prior to nanoparticle formation avoided the commonly reported issue of particle agglomeration. Inclusion of capping agents such as CA and PEG in the liquid during LAL modified the surface of the UCNPs and influenced the PL lifetimes of the samples. This had the advantage of avoiding a post modification step to control the UCNP solubility.

Laser fluence had considerable influence on the final product and the UCNP formation mechanism. Low laser fluences produced polydisperse particles consisting of no photoactive species through a thermal evaporative mechanism, while high laser fluences generated UCNPs with more uniform shapes and sizes and compositions similar to the target material by an explosive ejection mechanism. These observations provided valuable insight into how the LAL parameters affect nanomaterial formation during LAL. The LAL-prepared samples were compared to those produced through a solvothermal method and showed improvements both in size control and avoidance of degradation of the capping agent. This study demonstrated that LAL in water is a novel approach to synthesize UCNPs with advantages including size tuning, in-situ coating with water soluble capping agents, no use of toxic or high boiling point solvent, and short reaction times.

These studies prove that LAL is a robust and reproducible method to produce interesting PL materials. In addition to providing a faster and cleaner strategy to produce GQDs and UCNPs, these studies provided valuable information into the formation mechanisms of the LAL process. While all of the studies used a nanosecond laser, the composition of the final product had a high dependence on the target material properties. For the carbon-based samples, low laser fluences resulted in poor production efficiency. Since the carbon atoms are covalently bound in the target, it makes sense that a large input of energy would be required to remove them to form a plasma. The high fraction of observed sp^3 carbon in the GQDs indicated that there was a loss of the sp^2 carbon of the CNO target. Additionally, there was a high percentage of oxygen functional groups present, mainly hydroxyl. These observations suggest that the thermal evaporation mechanism is dominant, and that the plasma formed during LAL consists of carbon atoms and could

recruit oxygen from the surrounding liquid. For the UCNPs, the laser fluence had a strong influence on the product formed. Low laser fluences produced particles that mainly consisted of Na and F, both of which were much easier to vaporize than Y, Yb, and Er. At high fluences, however, the final composition more closely resembled the bulk starting material. This suggests that the mechanism switches to explosive ejection as the laser fluence is increased. At intermediate fluences, a high percentage of Er was observed in the product, but Y and Yb were not. Since Er absorbs 532 nm more strongly than Y and Yb it is reasonable to assume that the heating rates were not the same for these metals. This highlights the importance of considering laser wavelength and the absorbance of the target when designing LAL experiments.

The findings in this dissertation can be used to design future experiments to explore other classes of materials. For instance, all of the GQDs reported in this work were prepared from CNOs. This starting material was selected due to its high purity and ordered sp^2 structure. CNOs had the additional advantage as a starting material because previous research had established that they were a suitable precursor to form GQDs, and their properties were well understood. However, CNOs suffer the drawback that they are formed from nanodiamonds and require a high temperature annealing step under helium to convert to CNOs. This makes them costly and impractical as a precursor on a larger scale. However, alternative precursors, such as carbon black, graphite, or petroleum coke (a byproduct of petroleum refining) can also be used.[179-180] These precursors are less costly and readily available. Figure 5.1 shows the PL and FT-IR of GQDs produced from petroleum coke using LAL. These GQDs have similar PL properties and functional group patterns to the GQDs produced from CNOs. Future directions could explore the GQDs produced from these materials in more detail to optimize them for practical implementation and scale up.
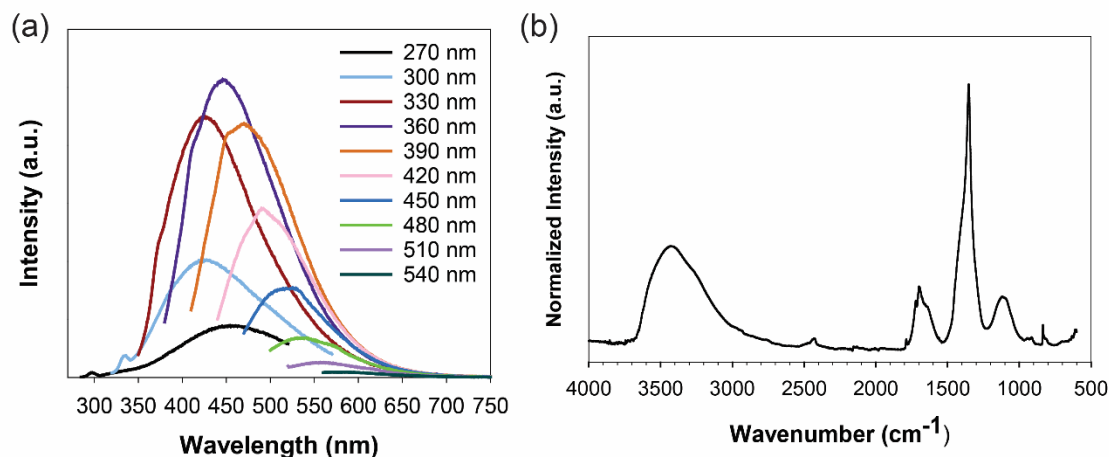
Figure 5.1 PL (a) and FT-IR (b) spectra of GQDs produced by LAL using petroleum coke as a precursor.

Other types of doping could also be considered. For instance, many heteroatoms such as boron, phosphorus, and sulfur, have been shown to have interesting applications in catalysis, sensing, and imaging.[78, 206, 239] The findings from the nitrogen doped GQD study show that LAL not only can be used to dope, but also control the functional groups simply by adding a small molecule precursor in the liquid, and the concentration of heteroatoms can also be controlled by controlling the concentration of the precursor in the liquid. Using LAL in water to form catalytic particles offers the added advantage of avoiding extra precursors or stabilizing agents that risk blocking the catalytic site. In addition to heteroatoms, doping with metal ions can also be explored.[240-241] As previously shown, the GQDs formed during LAL have a high-water solubility which was undesirable for the preparation of electrodes. LAL with lower laser fluence may allow for doping of a graphitic precursor without causing fragmentation. This could help the final product maintain the hydrophobicity of the precursor while still improving electrocatalytic activity. Since lower laser fluences would be required, larger laser spot sizes could be used to improve doping efficiency and scale up.

Finally, alternative strategies can be implemented to use LAL to produce upconverting nanomaterials. The solvothermal method was shown to quickly produce particles with only the desired β-phase present, however these samples were quite large and were not water soluble. Solvothermal methods could be used to replace the coprecipitation method to produce the target material for LAL. This would also improve the process by removing the annealing step. Finally, GQDs have been shown to be promising materials for PDT applications with low cytotoxicity.[80, 242] As previously discussed, UCNPs are desirable for PDT because the excitation wavelengths used have better penetration depths. GQDs could be coupled to UCNPs for PDT applications. GQDs could replace the CA and PEG capping agents during LAL. The GQDs not only would act as a stabilizing agent, but also would also absorb the emitted PL from the UCNPs and produce singlet oxygen. Singlet oxygen production could be directly measured because it has a strong emission band at 1275 nm. A major challenge to building this system will be producing UCNPs with high upconversion efficiency that also have strong FRET overlap with the GQDs, however I believe it is a promising direction to consider. GQDs coupled to UCNPs have also shown promise for other applications including security and metal ion sensing.[131, 243] Clearly, there are many potential directions for continuing work inspired by the studies presented in this dissertation.

REFERENCES

1. Skoog, D. A.; Skoog, D. A., *Fundamentals of analytical chemistry*. 8th ed.; Thomson-Brooks/Cole: Belmont, CA, 2004.
2. Dong, B.; Xu, S.; Sun, J.; Bi, S.; Li, D.; Bai, X.; Wang, Y.; Wang, L.; Song, H., Multifunctional NaYF4 : Yb3+,Er3+@Ag core/shell nanocomposites: integration of upconversion imaging and photothermal therapy. *J. Mater. Chem.* **2011,** *21* (17), 6193-6200.
3. Wegner, K. D.; Hildebrandt, N., Quantum dots: bright and versatile in vitro and in vivo fluorescence imaging biosensors. *Chem. Soc. Rev.* **2015,** *44* (14), 4792-4834.
4. Andresen, E.; Resch-Genger, U.; Schäferling, M., Surface Modifications for Photon-Upconversion-Based Energy-Transfer Nanoprobes. *Langmuir* **2019,** *35* (15), 5093-5113.
5. Gao, M.; Tang, B. Z., Fluorescent Sensors Based on Aggregation-Induced Emission: Recent Advances and Perspectives. *ACS Sensors* **2017,** *2* (10), 1382-1399.
6. Li, M.; Chen, T.; Gooding, J. J.; Liu, J., Review of Carbon and Graphene Quantum Dots for Sensing. *ACS Sensors* **2019,** *4* (7), 1732-1748.
7. Zhao, X.; Ng, J. D. A.; Friend, R. H.; Tan, Z.-K., Opportunities and Challenges in Perovskite Light-Emitting Devices. *ACS Photonics* **2018,** *5* (10), 3866-3875.
8. Kwon, W.; Do, S.; Lee, J.; Hwang, S.; Kim, J. K.; Rhee, S.-W., Freestanding Luminescent Films of Nitrogen-Rich Carbon Nanodots toward Large-Scale Phosphor-Based White-Light-Emitting Devices. *Chem. Mater.* **2013,** *25* (9), 1893-1899.
9. Kramer, I. J.; Sargent, E. H., Colloidal Quantum Dot Photovoltaics: A Path Forward. *ACS Nano* **2011,** *5* (11), 8506-8514.
10. Albero, J.; Clifford, J. N.; Palomares, E., Quantum dot based molecular solar cells. *Coord. Chem. Rev.* **2014,** *263-264*, 53-64.
11. Bajorowicz, B.; Kobylański, M. P.; Gołąbiewska, A.; Nadolna, J.; Zaleska-Medynska, A.; Malankowska, A., Quantum dot-decorated semiconductor micro- and nanoparticles: A review of their synthesis, characterization and application in photocatalysis. *Adv. Colloid Interface Sci.* **2018,** *256*, 352-372.
12. Cheng, L.; Xiang, Q.; Liao, Y.; Zhang, H., CdS-Based photocatalysts. *Energy & Environmental Science* **2018,** *11* (6), 1362-1391.
13. Fernando, K. A. S.; Sahu, S.; Liu, Y.; Lewis, W. K.; Guliants, E. A.; Jafariyan, A.; Wang, P.; Bunker, C. E.; Sun, Y.-P., Carbon Quantum Dots and Applications in Photocatalytic Energy Conversion. *ACS Appl. Mater. Interfaces* **2015,** *7* (16), 8363-8376.
14. Khan, S.; Gupta, A.; Verma, N. C.; Nandi, C. K., Time-Resolved Emission Reveals Ensemble of Emissive States as the Origin of Multicolor Fluorescence in Carbon Dots. *Nano Lett.* **2015,** *15* (12), 8300-8305.
15. Bernath, P. F., *Spectra of Atoms and Molecules*. 2nd ed.; Oxford University Press: 2005.
16. Lakowicz, J. R., *Principles of Fluorescence Spectroscopy*. 3rd ed.; Springer: 2006.
17. Berezin, M. Y.; Achilefu, S., Fluorescence Lifetime Measurements and Biological Imaging. *Chem. Rev.* **2010,** *110* (5), 2641-2684.

18. Röding, M.; Bradley, S. J.; Nydén, M.; Nann, T., Fluorescence Lifetime Analysis of Graphene Quantum Dots. *J. Phys. Chem. C* **2014,** *118* (51), 30282-30290.

19. Skoog, D. A.; Holler, F. J.; Crouch, S. R., *Principles of instrumental analysis*. 6th ed.; Thomson Brooks/Cole: Belmont, CA, 2007; p xv, 1039 p.

20. del Valle, J. C.; Catalán, J., Kasha's rule: a reappraisal. *PCCP* **2019,** *21* (19), 10061-10069.

21. Kim, M. R.; Ma, D., Quantum-Dot-Based Solar Cells: Recent Advances, Strategies, and Challenges. *J. Phys. Chem. Lett.* **2015,** *6* (1), 85-99.

22. Parak, W. J.; Manna, L.; Simmel, F. C.; Gerion, D.; Alivisatos, P., Quantum Dots. In *Nanoparticles*, Wiley-VCH Verlag GmbH & Co. KGaA: 2005; pp 4-49.

23. Tessitore, G.; Mandl, G. A.; Brik, M. G.; Park, W.; Capobianco, J. A., Recent insights into upconverting nanoparticles: spectroscopy, modeling, and routes to improved luminescence. *Nanoscale* **2019,** *11* (25), 12015-12029.

24. Na, H. B.; Palui, G.; Rosenberg, J. T.; Ji, X.; Grant, S. C.; Mattoussi, H., Multidentate Catechol-Based Polyethylene Glycol Oligomers Provide Enhanced Stability and Biocompatibility to Iron Oxide Nanoparticles. *ACS Nano* **2012,** *6* (1), 389-399.

25. Zhang, X.; Huang, P.-J. J.; Servos, M. R.; Liu, J., Effects of Polyethylene Glycol on DNA Adsorption and Hybridization on Gold Nanoparticles and Graphene Oxide. *Langmuir* **2012,** *28* (40), 14330-14337.

26. Wang, F.; Wang, J.; Liu, X., Direct Evidence of a Surface Quenching Effect on Size-Dependent Luminescence of Upconversion Nanoparticles. *Angew. Chem. Int. Ed.* **2010,** *49* (41), 7456-7460.

27. Uddin, M. A.; Calabro, R. L.; Kim, D.-Y.; Graham, K. R., Halide exchange and surface modification of metal halide perovskite nanocrystals with alkyltrichlorosilanes. *Nanoscale* **2018,** *10* (35), 16919-16927.

28. Mukherjee, S.; Prasad, E.; Chadha, A., H-Bonding controls the emission properties of functionalized carbon nano-dots. *PCCP* **2017,** *19* (10), 7288-7296.

29. Wen, X.; Yu, P.; Toh, Y.-R.; Hao, X.; Tang, J., Intrinsic and Extrinsic Fluorescence in Carbon Nanodots: Ultrafast Time-Resolved Fluorescence and Carrier Dynamics. *Adv. Opt. Mater.* **2013,** *1* (2), 173-178.

30. van Dam, B.; Nie, H.; Ju, B.; Marino, E.; Paulusse, J. M. J.; Schall, P.; Li, M.; Dohnalová, K., Excitation-Dependent Photoluminescence from Single-Carbon Dots. *Small* **2017,** *13* (48), 1702098.

31. Das, S. K.; Liu, Y.; Yeom, S.; Kim, D. Y.; Richards, C. I., Single-Particle Fluorescence Intensity Fluctuations of Carbon Nanodots. *Nano Lett.* **2014,** *14* (2), 620-625.

32. Bacon, M.; Bradley, S. J.; Nann, T., Graphene Quantum Dots. *Part. Part. Syst. Charact.* **2014,** *31* (4), 415-428.

33. Li, L.; Wu, G.; Yang, G.; Peng, J.; Zhao, J.; Zhu, J.-J., Focusing on luminescent graphene quantum dots: current status and future perspectives. *Nanoscale* **2013,** *5* (10), 4015-4039.

34. Zhong, Y.; Zhen, Z.; Zhu, H., Graphene: Fundamental research and potential applications. *FlatChem* **2017,** *4*, 20-32.

35. Avouris, P., Graphene: Electronic and Photonic Properties and Devices. *Nano Lett.* **2010,** *10* (11), 4285-4294.

36.	Wang, L.; Zhu, S.-J.; Wang, H.-Y.; Wang, Y.-F.; Hao, Y.-W.; Zhang, J.-H.; Chen, Q.-D.; Zhang, Y.-L.; Han, W.; Yang, B.; Sun, H.-B., Unraveling Bright Molecule-Like State and Dark Intrinsic State in Green-Fluorescence Graphene Quantum Dots via Ultrafast Spectroscopy. *Adv. Opt. Mater.* **2013,** *1* (3), 264-271.

37.	Tang, L.; Ji, R.; Cao, X.; Lin, J.; Jiang, H.; Li, X.; Teng, K. S.; Luk, C. M.; Zeng, S.; Hao, J.; Lau, S. P., Deep Ultraviolet Photoluminescence of Water-Soluble Self-Passivated Graphene Quantum Dots. *ACS Nano* **2012,** *6* (6), 5102-5110.

38.	Bao, X.; Yuan, Y.; Chen, J.; Zhang, B.; Li, D.; Zhou, D.; Jing, P.; Xu, G.; Wang, Y.; Holá, K.; Shen, D.; Wu, C.; Song, L.; Liu, C.; Zbořil, R.; Qu, S., In vivo theranostics with near-infrared-emitting carbon dots—highly efficient photothermal therapy based on passive targeting after intravenous administration. *Light: Science & Applications* **2018,** *7* (1), 91.

39.	Calabro, R. L.; Yang, D.-S.; Kim, D. Y., Single-Step Production and Controlled Nitrogen Doping of Graphene Quantum Dots through Laser Ablation in Liquid. *Submitted*.

40.	Wu, J.-B.; Lin, M.-L.; Cong, X.; Liu, H.-N.; Tan, P.-H., Raman spectroscopy of graphene-based materials and its applications in related devices. *Chem. Soc. Rev.* **2018,** *47* (5), 1822-1873.

41.	Wang, S.; Cole, I. S.; Zhao, D.; Li, Q., The dual roles of functional groups in the photoluminescence of graphene quantum dots. *Nanoscale* **2016,** *8* (14), 7449-7458.

42.	Fan, T.; Zeng, W.; Tang, W.; Yuan, C.; Tong, S.; Cai, K.; Liu, Y.; Huang, W.; Min, Y.; Epstein, A. J., Controllable size-selective method to prepare graphene quantum dots from graphene oxide. *Nanoscale Research Letters* **2015,** *10* (1), 55.

43.	Liu, Y.; Kim, D. Y., Ultraviolet and blue emitting graphene quantum dots synthesized from carbon nano-onions and their comparison for metal ion sensing. *Chem. Commun.* **2015,** *51* (20), 4176-4179.

44.	Pan, D.; Zhang, J.; Li, Z.; Wu, M., Hydrothermal Route for Cutting Graphene Sheets into Blue-Luminescent Graphene Quantum Dots. *Adv. Mater.* **2010,** *22* (6), 734-738.

45.	Pan, D.; Guo, L.; Zhang, J.; Xi, C.; Xue, Q.; Huang, H.; Li, J.; Zhang, Z.; Yu, W.; Chen, Z.; Li, Z.; Wu, M., Cutting sp2clusters in graphene sheets into colloidal graphene quantum dots with strong green fluorescence. *J. Mater. Chem.* **2012,** *22* (8), 3314-3318.

46.	Li, H.; Kang, Z.; Liu, Y.; Lee, S.-T., Carbon nanodots: synthesis, properties and applications. *J. Mater. Chem.* **2012,** *22* (46), 24230-24253.

47.	Sun, H.; Wu, L.; Wei, W.; Qu, X., Recent advances in graphene quantum dots for sensing. *Mater. Today* **2013,** *16* (11), 433-442.

48.	Yang, W.; Zhang, H.; Lai, J.; Peng, X.; Hu, Y.; Gu, W.; Ye, L., Carbon dots with red-shifted photoluminescence by fluorine doping for optical bio-imaging. *Carbon* **2018,** *128*, 78-85.

49.	Li, Y.; Zhao, Y.; Cheng, H.; Hu, Y.; Shi, G.; Dai, L.; Qu, L., Nitrogen-Doped Graphene Quantum Dots with Oxygen-Rich Functional Groups. *JACS* **2012,** *134* (1), 15-18.

50.	Tan, X.; Li, Y.; Li, X.; Zhou, S.; Fan, L.; Yang, S., Electrochemical synthesis of small-sized red fluorescent graphene quantum dots as a bioimaging platform. *Chem. Commun.* **2015,** *51* (13), 2544-2546.

51.   Kumar, S.; Aziz, S. K. T.; Girshevitz, O.; Nessim, G. D., One-Step Synthesis of N-Doped Graphene Quantum Dots from Chitosan as a Sole Precursor Using Chemical Vapor Deposition. *J. Phys. Chem. C* **2018,** *122* (4), 2343-2349.

52.   Cui, B.; Yan, L.; Gu, H.; Yang, Y.; Liu, X.; Ma, C.-Q.; Chen, Y.; Jia, H., Fluorescent carbon quantum dots synthesized by chemical vapor deposition: An alternative candidate for electron acceptor in polymer solar cells. *Opt. Mater.* **2018,** *75*, 166-173.

53.   Schneider, J.; Reckmeier, C. J.; Xiong, Y.; von Seckendorff, M.; Susha, A. S.; Kasák, P.; Rogach, A. L., Molecular Fluorescence in Citric Acid-Based Carbon Dots. *J. Phys. Chem. C* **2017,** *121* (3), 2014-2022.

54.   Essner, J. B.; Kist, J. A.; Polo-Parada, L.; Baker, G. A., Artifacts and Errors Associated with the Ubiquitous Presence of Fluorescent Impurities in Carbon Nanodots. *Chem. Mater.* **2018,** *30* (6), 1878-1887.

55.   Bao, L.; Zhang, Z.-L.; Tian, Z.-Q.; Zhang, L.; Liu, C.; Lin, Y.; Qi, B.; Pang, D.-W., Electrochemical Tuning of Luminescent Carbon Nanodots: From Preparation to Luminescence Mechanism. *Adv. Mater.* **2011,** *23* (48), 5801-5806.

56.   Santiago, S. R. M.; Lin, T. N.; Yuan, C. T.; Shen, J. L.; Huang, H. Y.; Lin, C. A. J., Origin of tunable photoluminescence from graphene quantum dots synthesized via pulsed laser ablation. *PCCP* **2016,** *18* (32), 22599-22605.

57.   Xiao, L.; Sun, H., Novel properties and applications of carbon nanodots. *Nanoscale Horizons* **2018,** *3* (6), 565-597.

58.   Lim, S. Y.; Shen, W.; Gao, Z., Carbon quantum dots and their applications. *Chem. Soc. Rev.* **2015,** *44* (1), 362-381.

59.   Sun, Y.-P.; Zhou, B.; Lin, Y.; Wang, W.; Fernando, K. A. S.; Pathak, P.; Meziani, M. J.; Harruff, B. A.; Wang, X.; Wang, H.; Luo, P. G.; Yang, H.; Kose, M. E.; Chen, B.; Veca, L. M.; Xie, S.-Y., Quantum-Sized Carbon Dots for Bright and Colorful Photoluminescence. *JACS* **2006,** *128* (24), 7756-7757.

60.   Huang, P.; Shi, J.-j.; Zhang, M.; Jiang, X.-h.; Zhong, H.-x.; Ding, Y.-m.; Cao, X.; Wu, M.; Lu, J., Anomalous Light Emission and Wide Photoluminescence Spectra in Graphene Quantum Dot: Quantum Confinement from Edge Microstructure. *J. Phys. Chem. Lett.* **2016,** *7* (15), 2888-2892.

61.   Wang, L.; Zhu, S.-J.; Wang, H.-Y.; Qu, S.-N.; Zhang, Y.-L.; Zhang, J.-H.; Chen, Q.-D.; Xu, H.-L.; Han, W.; Yang, B.; Sun, H.-B., Common Origin of Green Luminescence in Carbon Nanodots and Graphene Quantum Dots. *ACS Nano* **2014,** *8* (3), 2541-2547.

62.   Holá, K.; Sudolská, M.; Kalytchuk, S.; Nachtigallová, D.; Rogach, A. L.; Otyepka, M.; Zbořil, R., Graphitic Nitrogen Triggers Red Fluorescence in Carbon Dots. *ACS Nano* **2017,** *11* (12), 12402-12410.

63.   Zhao, M.; Yang, F.; Xue, Y.; Xiao, D.; Guo, Y., A Time-Dependent DFT Study of the Absorption and Fluorescence Properties of Graphene Quantum Dots. *ChemPhysChem* **2014,** *15* (5), 950-957.

64.   Geethalakshmi, K. R.; Ng, T. Y.; Crespo-Otero, R., Tunable optical properties of OH-functionalised graphene quantum dots. *J. Mater. Chem. C* **2016,** *4* (36), 8429-8438.

65. Xu, Q.; Zhou, Q.; Hua, Z.; Xue, Q.; Zhang, C.; Wang, X.; Pan, D.; Xiao, M., Single-Particle Spectroscopic Measurements of Fluorescent Graphene Quantum Dots. *ACS Nano* **2013,** *7* (12), 10654-10661.

66. Das, S. K.; Luk, C. M.; Martin, W. E.; Tang, L.; Kim, D. Y.; Lau, S. P.; Richards, C. I., Size and Dopant Dependent Single Particle Fluorescence Properties of Graphene Quantum Dots. *J. Phys. Chem. C* **2015,** *119* (31), 17988-17994.

67. Zhao, S.; Lavie, J.; Rondin, L.; Orcin-Chaix, L.; Diederichs, C.; Roussignol, P.; Chassagneux, Y.; Voisin, C.; Müllen, K.; Narita, A.; Campidelli, S.; Lauret, J.-S., Single photon emission from graphene quantum dots at room temperature. *Nature Communications* **2018,** *9* (1), 3470.

68. Yeh, T.-F.; Huang, W.-L.; Chung, C.-J.; Chiang, I. T.; Chen, L.-C.; Chang, H.-Y.; Su, W.-C.; Cheng, C.; Chen, S.-J.; Teng, H., Elucidating Quantum Confinement in Graphene Oxide Dots Based On Excitation-Wavelength-Independent Photoluminescence. *J. Phys. Chem. Lett.* **2016,** *7* (11), 2087-2092.

69. Kwon, W.; Kim, Y.-H.; Lee, C.-L.; Lee, M.; Choi, H. C.; Lee, T.-W.; Rhee, S.-W., Electroluminescence from Graphene Quantum Dots Prepared by Amidative Cutting of Tattered Graphite. *Nano Lett.* **2014,** *14* (3), 1306-1311.

70. Kyu Kim, J.; Bae, S.; Yi, Y.; Jin Park, M.; Jin Kim, S.; Myoung, N.; Lee, C.-L.; Hee Hong, B.; Hyeok Park, J., Origin of White Electroluminescence in Graphene Quantum Dots Embedded Host/Guest Polymer Light Emitting Diodes. *Sci. Rep.* **2015,** *5* (1), 11032.

71. Wang, G.; He, P.; Xu, A.; Guo, Q.; Li, J.; Wang, Z.; Liu, Z.; Chen, D.; Yang, S.; Ding, G., Promising Fast Energy Transfer System Between Graphene Quantum Dots and the Application in Fluorescent Bioimaging. *Langmuir* **2019,** *35* (3), 760-766.

72. Chandra, A.; Singh, N., Cell Microenvironment pH Sensing in 3D Microgels Using Fluorescent Carbon Dots. *ACS Biomaterials Science & Engineering* **2017,** *3* (12), 3620-3627.

73. Edwards, J. K.; Thomas, A.; Carley, A. F.; Herzing, A. A.; Kiely, C. J.; Hutchings, G. J., Au–Pd supported nanocrystals as catalysts for the direct synthesis of hydrogen peroxide from H2 and O2. *Green Chemistry* **2008,** *10* (4), 388-394.

74. Wang, J.; Zhang, P.; Huang, C.; Liu, G.; Leung, K. C.-F.; Wáng, Y. X. J., High Performance Photoluminescent Carbon Dots for In Vitro and In Vivo Bioimaging: Effect of Nitrogen Doping Ratios. *Langmuir* **2015,** *31* (29), 8063-8073.

75. Wu, J.; Ma, S.; Sun, J.; Gold, J. I.; Tiwary, C.; Kim, B.; Zhu, L.; Chopra, N.; Odeh, I. N.; Vajtai, R.; Yu, A. Z.; Luo, R.; Lou, J.; Ding, G.; Kenis, P. J. A.; Ajayan, P. M., A metal-free electrocatalyst for carbon dioxide reduction to multi-carbon hydrocarbons and oxygenates. *Nature Communications* **2016,** *7* (1), 13869.

76. Wang, R.; Li, G.; Dong, Y.; Chi, Y.; Chen, G., Carbon Quantum Dot-Functionalized Aerogels for NO2 Gas Sensing. *Anal. Chem.* **2013,** *85* (17), 8065-8069.

77. Meng, A.; Xu, Q.; Zhao, K.; Li, Z.; Liang, J.; Li, Q., A highly selective and sensitive "on-off-on" fluorescent probe for detecting Hg(II) based on Au/N-doped carbon quantum dots. *Sensors and Actuators B: Chemical* **2018,** *255*, 657-665.

78. Liu, Y.; Gong, X.; Dong, W.; Zhou, R.; Shuang, S.; Dong, C., Nitrogen and phosphorus dual-doped carbon dots as a label-free sensor for Curcumin determination in real sample and cellular imaging. *Talanta* **2018,** *183*, 61-69.

79. Cho, H.-H.; Yang, H.; Kang, D. J.; Kim, B. J., Surface Engineering of Graphene Quantum Dots and Their Applications as Efficient Surfactants. *ACS Appl. Mater. Interfaces* **2015,** *7* (16), 8615-8621.

80. Pillar-Little, T. J.; Wanninayake, N.; Nease, L.; Heidary, D. K.; Glazer, E. C.; Kim, D. Y., Superior photodynamic effect of carbon quantum dots through both type I and type II pathways: Detailed comparison study of top-down-synthesized and bottom-up-synthesized carbon quantum dots. *Carbon* **2018,** *140*, 616-623.

81. Kim, J.; Lee, B.; Kim, Y. J.; Hwang, S. W., Enhancement of Dye-sensitized Solar Cells Efficiency Using Graphene Quantum Dots as Photoanode. *Bull. Korean Chem. Soc.* **2019,** *40* (1), 56-61.

82. Nadort, A.; Zhao, J.; Goldys, E. M., Lanthanide upconversion luminescence at the nanoscale: fundamentals and optical properties. *Nanoscale* **2016,** *8* (27), 13099-13130.

83. Zhou, B.; Shi, B.; Jin, D.; Liu, X., Controlling upconversion nanocrystals for emerging applications. *Nature Nanotechnology* **2015,** *10* (11), 924-936.

84. Dong, H.; Sun, L.-D.; Yan, C.-H., Basic understanding of the lanthanide related upconversion emissions. *Nanoscale* **2013,** *5* (13), 5703-5714.

85. Auzel, F., Upconversion and Anti-Stokes Processes with f and d Ions in Solids. *Chem. Rev.* **2004,** *104* (1), 139-174.

86. Wang, M.; Abbineni, G.; Clevenger, A.; Mao, C.; Xu, S., Upconversion nanoparticles: synthesis, surface modification and biological applications. *Nanomedicine: Nanotechnology, Biology and Medicine* **2011,** *7* (6), 710-729.

87. Wang, F.; Liu, X., Recent advances in the chemistry of lanthanide-doped upconversion nanocrystals. *Chem. Soc. Rev.* **2009,** *38* (4), 976-989.

88. Babu, P.; Martín, I. R.; Venkata Krishnaiah, K.; Seo, H. J.; Venkatramu, V.; Jayasankar, C. K.; Lavín, V., Photon avalanche upconversion in Ho3+–Yb3+ co-doped transparent oxyfluoride glass–ceramics. *Chem. Phys. Lett.* **2014,** *600*, 34-37.

89. Weingarten, D. H.; LaCount, M. D.; van de Lagemaat, J.; Rumbles, G.; Lusk, M. T.; Shaheen, S. E., Experimental demonstration of photon upconversion via cooperative energy pooling. *Nature Communications* **2017,** *8* (1), 14808.

90. LaCount, M. D.; Weingarten, D.; Hu, N.; Shaheen, S. E.; van de Lagemaat, J.; Rumbles, G.; Walba, D. M.; Lusk, M. T., Energy Pooling Upconversion in Organic Molecular Systems. *J. Phys. Chem. A* **2015,** *119* (17), 4009-4016.

91. Askes, S. H. C.; Kloz, M.; Bruylants, G.; Kennis, J. T. M.; Bonnet, S., Triplet-triplet annihilation upconversion followed by FRET for the red light activation of a photodissociative ruthenium complex in liposomes. *PCCP* **2015,** *17* (41), 27380-27390.

92. Zhou, J.; Liu, Q.; Feng, W.; Sun, Y.; Li, F., Upconversion Luminescent Materials: Advances and Applications. *Chem. Rev.* **2015,** *115* (1), 395-465.

93. Gholizadeh, E. M.; Frazer, L.; MacQueen, R. W.; Gallaher, J. K.; Schmidt, T. W., Photochemical upconversion is suppressed by high concentrations of molecular sensitizers. *PCCP* **2018,** *20* (29), 19500-19506.

94. Wang, W.; Liu, Q.; Zhan, C.; Barhoumi, A.; Yang, T.; Wylie, R. G.; Armstrong, P. A.; Kohane, D. S., Efficient Triplet–Triplet Annihilation-Based Upconversion for Nanoparticle Phototargeting. *Nano Lett.* **2015,** *15* (10), 6332-6338.

95. Bunzli, J.-C. G.; Piguet, C., Taking advantage of luminescent lanthanide ions. *Chem. Soc. Rev.* **2005,** *34* (12), 1048-1077.

96. Sedlmeier, A.; Gorris, H. H., Surface modification and characterization of photon-upconverting nanoparticles for bioanalytical applications. *Chem. Soc. Rev.* **2015,** *44* (6), 1526-1560.

97. Moore, E. G.; Samuel, A. P. S.; Raymond, K. N., From Antenna to Assay: Lessons Learned in Lanthanide Luminescence. *Acc. Chem. Res.* **2009,** *42* (4), 542-552.

98. Weller, M.; Overton, T.; Rourke, J.; Armstrong, F. A., *Inorganic chemistry*. Sixth edition. ed.; Oxford University Press: Oxford, 2014; p xx, 875 pages.

99. DaCosta, M. V.; Doughan, S.; Han, Y.; Krull, U. J., Lanthanide upconversion nanoparticles and applications in bioassays and bioimaging: A review. *Anal. Chim. Acta* **2014,** *832*, 1-33.

100. Gainer, C. F.; Romanowski, M., A review of synthetic methods for the production of upconverting lanthanide nanoparticles. *Journal of Innovative Optical Health Sciences* **2014,** *07* (02), 1330007.

101. Krämer, K. W.; Biner, D.; Frei, G.; Güdel, H. U.; Hehlen, M. P.; Lüthi, S. R., Hexagonal Sodium Yttrium Fluoride Based Green and Blue Emitting Upconversion Phosphors. *Chem. Mater.* **2004,** *16* (7), 1244-1251.

102. Damasco, J. A.; Chen, G.; Shao, W.; Ågren, H.; Huang, H.; Song, W.; Lovell, J. F.; Prasad, P. N., Size-Tunable and Monodisperse Tm3+/Gd3+-Doped Hexagonal NaYbF4 Nanoparticles with Engineered Efficient Near Infrared-to-Near Infrared Upconversion for In Vivo Imaging. *ACS Appl. Mater. Interfaces* **2014,** *6* (16), 13884-13893.

103. Lay, A.; Siefe, C.; Fischer, S.; Mehlenbacher, R. D.; Ke, F.; Mao, W. L.; Alivisatos, A. P.; Goodman, M. B.; Dionne, J. A., Bright, Mechanosensitive Upconversion with Cubic-Phase Heteroepitaxial Core–Shell Nanoparticles. *Nano Lett.* **2018,** *18* (7), 4454-4459.

104. Sudheendra, L.; Ortalan, V.; Dey, S.; Browning, N. D.; Kennedy, I. M., Plasmonic Enhanced Emissions from Cubic NaYF4:Yb:Er/Tm Nanophosphors. *Chem. Mater.* **2011,** *23* (11), 2987-2993.

105. Yang, D.; Chen, D.; He, H.; Pan, Q.; Xiao, Q.; Qiu, J.; Dong, G., Controllable Phase Transformation and Mid-infrared Emission from Er3+-Doped Hexagonal-/Cubic-NaYF4 Nanocrystals. *Sci. Rep.* **2016,** *6*, 29871.

106. Klier, D. T.; Kumke, M. U., Analysing the effect of the crystal structure on upconversion luminescence in Yb3+,Er3+-co-doped NaYF4 nanomaterials. *J. Mater. Chem. C* **2015,** *3* (42), 11228-11238.

107. Dyck, N. C.; van Veggel, F. C. J. M.; Demopoulos, G. P., Size-Dependent Maximization of Upconversion Efficiency of Citrate-Stabilized β-phase NaYF4:Yb3+,Er3+ Crystals via Annealing. *ACS Appl. Mater. Interfaces* **2013,** *5* (22), 11661-11667.

108. Wei, Y.; Lu, F.; Zhang, X.; Chen, D., Synthesis and characterization of efficient near-infrared upconversion Yb and Tm codoped NaYF4 nanocrystal reporter. *J. Alloys Compd.* **2007,** *427* (1), 333-340.

109. Berry, M. T.; May, P. S., Disputed Mechanism for NIR-to-Red Upconversion Luminescence in NaYF4:Yb3+,Er3+. *J. Phys. Chem. A* **2015,** *119* (38), 9805-9811.

110. Rabouw, F. T.; Prins, P. T.; Villanueva-Delgado, P.; Castelijns, M.; Geitenbeek, R. G.; Meijerink, A., Quenching Pathways in NaYF4:Er3+,Yb3+ Upconversion Nanocrystals. *ACS Nano* **2018,** *12* (5), 4812-4823.

111. Anderson, R. B.; Smith, S. J.; May, P. S.; Berry, M. T., Revisiting the NIR-to-Visible Upconversion Mechanism in β-NaYF4:Yb3+,Er3+. *J. Phys. Chem. Lett.* **2014,** *5* (1), 36-42.

112. Layne, C. B.; Lowdermilk, W. H.; Weber, M. J., Multiphonon relaxation of rare-earth ions in oxide glasses. *Physical Review B* **1977,** *16* (1), 10-20.

113. Hu, Y.; Shao, Q.; Dong, Y.; Jiang, J., Energy Loss Mechanism of Upconversion Core/Shell Nanocrystals. *J. Phys. Chem. C* **2019,** *123* (36), 22674-22679.

114. Chen, G.; Shen, J.; Ohulchanskyy, T. Y.; Patel, N. J.; Kutikov, A.; Li, Z.; Song, J.; Pandey, R. K.; Ågren, H.; Prasad, P. N.; Han, G., (α-NaYbF4:Tm3+)/CaF2 Core/Shell Nanoparticles with Efficient Near-Infrared to Near-Infrared Upconversion for High-Contrast Deep Tissue Bioimaging. *ACS Nano* **2012,** *6* (9), 8280-8287.

115. Wilhelm, S.; Kaiser, M.; Würth, C.; Heiland, J.; Carrillo-Carrion, C.; Muhr, V.; Wolfbeis, O. S.; Parak, W. J.; Resch-Genger, U.; Hirsch, T., Water dispersible upconverting nanoparticles: effects of surface modification on their luminescence and colloidal stability. *Nanoscale* **2015,** *7* (4), 1403-1410.

116. Liu, Q.; Feng, W.; Yang, T.; Yi, T.; Li, F., Upconversion luminescence imaging of cells and small animals. *Nat. Protocols* **2013,** *8* (10), 2033-2044.

117. Zhang, J.; Zhao, H.; Zhang, X.; Wang, X.; Gao, H.; Zhang, Z.; Cao, W., Monochromatic Near-Infrared to Near-Infrared Upconversion Nanoparticles for High-Contrast Fluorescence Imaging. *J. Phys. Chem. C* **2014,** *118* (5), 2820-2825.

118. Liu, Y.; Tu, D.; Zhu, H.; Ma, E.; Chen, X., Lanthanide-doped luminescent nano-bioprobes: from fundamentals to biodetection. *Nanoscale* **2013,** *5* (4), 1369-1384.

119. Zhou, J.-C.; Yang, Z.-L.; Dong, W.; Tang, R.-J.; Sun, L.-D.; Yan, C.-H., Bioimaging and toxicity assessments of near-infrared upconversion luminescent NaYF4:Yb,Tm nanocrystals. *Biomaterials* **2011,** *32* (34), 9059-9067.

120. Wu, S.; Han, G.; Milliron, D. J.; Aloni, S.; Altoe, V.; Talapin, D. V.; Cohen, B. E.; Schuck, P. J., Non-blinking and photostable upconverted luminescence from single lanthanide-doped nanocrystals. *Proceedings of the National Academy of Sciences* **2009,** *106* (27), 10917-10921.

121. Buchner, M.; García Calavia, P.; Muhr, V.; Kröninger, A.; Baeumner, A. J.; Hirsch, T.; Russell, D. A.; Marín, M. J., Photosensitiser functionalised luminescent upconverting nanoparticles for efficient photodynamic therapy of breast cancer cells. *Photochemical & Photobiological Sciences* **2019,** *18* (1), 98-109.

122. Lay, A.; Wang, D. S.; Wisser, M. D.; Mehlenbacher, R. D.; Lin, Y.; Goodman, M. B.; Mao, W. L.; Dionne, J. A., Upconverting Nanoparticles as Optical Sensors of Nano- to Micro-Newton Forces. *Nano Lett.* **2017,** *17* (7), 4172-4177.

123. Baride, A.; Meruga, J. M.; Douma, C.; Langerman, D.; Crawford, G.; Kellar, J. J.; Cross, W. M.; May, P. S., A NIR-to-NIR upconversion luminescence system for security printing applications. *RSC Advances* **2015,** *5* (123), 101338-101346.

124. Sun, Y.; Zhu, X.; Peng, J.; Li, F., Core–Shell Lanthanide Upconversion Nanophosphors as Four-Modal Probes for Tumor Angiogenesis Imaging. *ACS Nano* **2013,** *7* (12), 11290-11300.

125. Michael Dcona, M.; Yu, Q.; Capobianco, J. A.; Hartman, M. C. T., Near infrared light mediated release of doxorubicin using upconversion nanoparticles. *Chem. Commun.* **2015,** *51* (40), 8477-8479.

126. Wang, H.; Han, R.-l.; Yang, L.-m.; Shi, J.-h.; Liu, Z.-j.; Hu, Y.; Wang, Y.; Liu, S.-j.; Gan, Y., Design and Synthesis of Core–Shell–Shell Upconversion Nanoparticles for NIR-Induced Drug Release, Photodynamic Therapy, and Cell Imaging. *ACS Appl. Mater. Interfaces* **2016,** *8* (7), 4416-4423.

127. Hamblin, M. R., Fullerenes as photosensitizers in photodynamic therapy: pros and cons. *Photochemical & Photobiological Sciences* **2018,** *17* (11), 1515-1533.

128. Muhr, V.; Würth, C.; Kraft, M.; Buchner, M.; Baeumner, A. J.; Resch-Genger, U.; Hirsch, T., Particle-Size-Dependent Förster Resonance Energy Transfer from Upconversion Nanoparticles to Organic Dyes. *Anal. Chem.* **2017,** *89* (9), 4868-4874.

129. Meruga, J. M.; Cross, W. M.; Petersen, J. B.; May, P. S.; Baride, A.; Cessac, K.; Kellar, J. J., Stable Inks Containing Upconverting Nanoparticles Based on an Oil-in-Water Nanoemulsion. *Langmuir* **2018,** *34* (4), 1535-1541.

130. Wen, S.; Zhou, J.; Zheng, K.; Bednarkiewicz, A.; Liu, X.; Jin, D., Advances in highly doped upconversion nanoparticles. *Nature Communications* **2018,** *9* (1), 2415.

131. Tan, H.; Gong, G.; Xie, S.; Song, Y.; Zhang, C.; Li, N.; Zhang, D.; Xu, L.; Xu, J.; Zheng, J., Upconversion Nanoparticles@Carbon Dots@Meso-SiO2 Sandwiched Core–Shell Nanohybrids with Tunable Dual-Mode Luminescence for 3D Anti-Counterfeiting Barcodes. *Langmuir* **2019,** *35* (35), 11503-11511.

132. Zhan, Q.; Qian, J.; Liang, H.; Somesfalean, G.; Wang, D.; He, S.; Zhang, Z.; Andersson-Engels, S., Using 915 nm Laser Excited Tm3+/Er3+/Ho3+-Doped NaYbF4 Upconversion Nanoparticles for in Vitro and Deeper in Vivo Bioimaging without Overheating Irradiation. *ACS Nano* **2011,** *5* (5), 3744-3757.

133. Tian, Q.; Tao, K.; Li, W.; Sun, K., Hot-Injection Approach for Two-Stage Formed Hexagonal NaYF4:Yb,Er Nanocrystals. *J. Phys. Chem. C* **2011,** *115* (46), 22886-22892.

134. Heuer-Jungemann, A.; Feliu, N.; Bakaimi, I.; Hamaly, M.; Alkilany, A.; Chakraborty, I.; Masood, A.; Casula, M. F.; Kostopoulou, A.; Oh, E.; Susumu, K.; Stewart, M. H.; Medintz, I. L.; Stratakis, E.; Parak, W. J.; Kanaras, A. G., The Role of Ligands in the Chemical Synthesis and Applications of Inorganic Nanoparticles. *Chem. Rev.* **2019,** *119* (8), 4819-4880.

135. Meijer, M. S.; Talens, V. S.; Hilbers, M. F.; Kieltyka, R. E.; Brouwer, A. M.; Natile, M. M.; Bonnet, S., NIR-Light-Driven Generation of Reactive Oxygen Species Using Ru(II)-Decorated Lipid-Encapsulated Upconverting Nanoparticles. *Langmuir* **2019,** *35* (37), 12079-12090.

136. May, P. B.; Suter, J. D.; May, P. S.; Berry, M. T., The Dynamics of Nanoparticle Growth and Phase Change During Synthesis of β-NaYF4. *J. Phys. Chem. C* **2016,** *120* (17), 9482-9489.

137.	Muhr, V.; Wilhelm, S.; Hirsch, T.; Wolfbeis, O. S., Upconversion Nanoparticles: From Hydrophobic to Hydrophilic Surfaces. *Acc. Chem. Res.* **2014,** *47* (12), 3481-3493.

138.	Lin, M.; Zhao, Y.; Wang, S.; Liu, M.; Duan, Z.; Chen, Y.; Li, F.; Xu, F.; Lu, T., Recent advances in synthesis and surface modification of lanthanide-doped upconversion nanoparticles for biomedical applications. *Biotechnol. Adv.* **2012,** *30* (6), 1551-1561.

139.	Shan, G.-B.; Assaaoudi, H.; Demopoulos, G. P., Enhanced Performance of Dye-Sensitized Solar Cells by Utilization of an External, Bifunctional Layer Consisting of Uniform β-NaYF4:Er3+/Yb3+ Nanoplatelets. *ACS Appl. Mater. Interfaces* **2011,** *3* (9), 3239-3243.

140.	Gao, G.; Zhang, C.; Zhou, Z.; Zhang, X.; Ma, J.; Li, C.; Jin, W.; Cui, D., One-pot hydrothermal synthesis of lanthanide ions doped one-dimensional upconversion submicrocrystals and their potential application in vivo CT imaging. *Nanoscale* **2013,** *5* (1), 351-362.

141.	Ding, M.; Lu, C.; Song, Y.; Ni, Y.; Xu, Z., Hydrothermal synthesis of ordered β-NaYF4 nanorod self-assemblies with multicolor up- and down-conversions. *CrystEngComm* **2014,** *16* (6), 1163-1173.

142.	Passuello, T.; Pedroni, M.; Piccinelli, F.; Polizzi, S.; Marzola, P.; Tambalo, S.; Conti, G.; Benati, D.; Vetrone, F.; Bettinelli, M.; Speghini, A., PEG-capped, lanthanide doped GdF3 nanoparticles: luminescent and T2 contrast agents for optical and MRI multimodal imaging. *Nanoscale* **2012,** *4* (24), 7682-7689.

143.	Yi, G.; Lu, H.; Zhao, S.; Ge, Y.; Yang, W.; Chen, D.; Guo, L.-H., Synthesis, Characterization, and Biological Application of Size-Controlled Nanocrystalline NaYF4:Yb,Er Infrared-to-Visible Up-Conversion Phosphors. *Nano Lett.* **2004,** *4* (11), 2191-2196.

144.	Li, Z.; Zhang, Y., Monodisperse Silica-Coated Polyvinylpyrrolidone/NaYF4 Nanocrystals with Multicolor Upconversion Fluorescence Emission. *Angew. Chem. Int. Ed.* **2006,** *45* (46), 7732-7735.

145.	Yi, G.-S.; Chow, G.-M., Colloidal LaF3:Yb,Er, LaF3:Yb,Ho and LaF3:Yb,Tm nanocrystals with multicolor upconversion fluorescence. *J. Mater. Chem.* **2005,** *15* (41), 4460-4464.

146.	Bogdan, N.; Vetrone, F.; Ozin, G. A.; Capobianco, J. A., Synthesis of Ligand-Free Colloidally Stable Water Dispersible Brightly Luminescent Lanthanide-Doped Upconverting Nanoparticles. *Nano Lett.* **2011,** *11* (2), 835-840.

147.	Lay, A.; Sheppard, O. H.; Siefe, C.; McLellan, C. A.; Mehlenbacher, R. D.; Fischer, S.; Goodman, M. B.; Dionne, J. A., Optically Robust and Biocompatible Mechanosensitive Upconverting Nanoparticles. *ACS Central Science* **2019,** *5* (7), 1211-1222.

148.	Guller, A. E.; Generalova, A. N.; Petersen, E. V.; Nechaev, A. V.; Trusova, I. A.; Landyshev, N. N.; Nadort, A.; Grebenik, E. A.; Deyev, S. M.; Shekhter, A. B.; Zvyagin, A. V., Cytotoxicity and non-specific cellular uptake of bare and surface-modified upconversion nanoparticles in human skin cells. *Nano Research* **2015,** *8* (5), 1546-1562.

149.	Rojas-Gutierrez, P. A.; Bekah, D.; Seuntjens, J.; DeWolf, C.; Capobianco, J. A., Cellular Uptake, Cytotoxicity and Trafficking of Supported Lipid-Bilayer-Coated

Lanthanide Upconverting Nanoparticles in Alveolar Lung Cancer Cells. *ACS Applied Bio Materials* **2019,** *2* (10), 4527-4536.

150. Gnach, A.; Lipinski, T.; Bednarkiewicz, A.; Rybka, J.; Capobianco, J. A., Upconverting nanoparticles: assessing the toxicity. *Chem. Soc. Rev.* **2015,** *44* (6), 1561-1584.

151. Vedunova, M. V.; Mishchenko, T. A.; Mitroshina, E. V.; Ponomareva, N. V.; Yudintsev, A. V.; Generalova, A. N.; Deyev, S. M.; Mukhina, I. V.; Semyanov, A. V.; Zvyagin, A. V., Cytotoxic effects of upconversion nanoparticles in primary hippocampal cultures. *RSC Advances* **2016,** *6* (40), 33656-33665.

152. Santiago, S. R. M.; Lin, T. N.; Chang, C. H.; Wong, Y. A.; Lin, C. A. J.; Yuan, C. T.; Shen, J. L., Synthesis of N-doped graphene quantum dots by pulsed laser ablation with diethylenetriamine (DETA) and their photoluminescence. *PCCP* **2017,** *19* (33), 22395-22400.

153. Novodchuk, I.; Irannejad, M.; Wales, B.; Ibrahim, K.; Sanderson, J.; Bajcsy, M.; Yavuz, M., Controlled volume production of simultaneously B/N co-doped reduced graphene oxide nanoflakes using femtosecond laser ablation. *Mater. Res. Bull.* **2019,** *111*, 80-86.

154. Lin, T. N.; Chih, K. H.; Yuan, C. T.; Shen, J. L.; Lin, C. A. J.; Liu, W. R., Laser-ablation production of graphene oxide nanostructures: from ribbons to quantum dots. *Nanoscale* **2015,** *7* (6), 2708-2715.

155. Zheng, C.; Yang, G.; Zhang, K.; Wang, C.; Wang, H.; Chen, F.; He, Y., Femtosecond-pulse laser-ablation-induced synthesis and improved emission properties of ultrafine Y2O3:Er3+, Yb3+ nanoparticles with reduced nonradiative relaxation. *J. Alloys Compd.* **2015,** *648*, 838-844.

156. Reza, Z.; Hamid-Reza, B.-P.; Azmi, Z.; Raheleh, J.; Golnoush, Z.; Avito, R.; Akrajas Ali, O., Upconversion Properties of the Er-Doped Y 2 O 3 , Bi 2 O 3 and Sb 2 O 3 Nanoparticles Fabricated by Pulsed Laser Ablation in Liquid Media. *Chinese Physics Letters* **2013,** *30* (11), 118103.

157. Anjana, R.; Kurias, K. M.; Jayaraj, M. K., Clean synthesis of YOF:Er3+, Yb3+ upconversion colloidal nanoparticles in water through liquid phase pulsed laser ablation for imaging applications. *Opt. Mater.* **2017,** *72*, 730-736.

158. Gemini, L.; Schmitz, T.; Kling, R.; Barcikowski, S.; Gökce, B., Upconversion Nanoparticles Synthesized by Ultrashort Pulsed Laser Ablation in Liquid: Effect of the Stabilizing Environment. *ChemPhysChem* **2017,** *18* (9), 1210-1216.

159. Singh, S. K.; Kumar, K.; Rai, S. B., Synthesis and spectroscopy of transparent colloidal solution of Gd2O3: Er3+, Yb3+ spherical nanocrystals by pulsed laser ablation. *Materials Science and Engineering: B* **2010,** *166* (2), 180-184.

160. Sajti, C. L.; Sattari, R.; Chichkov, B. N.; Barcikowski, S., Gram Scale Synthesis of Pure Ceramic Nanoparticles by Laser Ablation in Liquid. *The Journal of Physical Chemistry C* **2010,** *114* (6), 2421-2427.

161. Zhang, D.; Gökce, B.; Barcikowski, S., Laser Synthesis and Processing of Colloids: Fundamentals and Applications. *Chem. Rev.* **2017,** *117* (5), 3990-4103.

162. Cristoforetti, G.; Pitzalis, E.; Spiniello, R.; Ishak, R.; Muniz-Miranda, M., Production of Palladium Nanoparticles by Pulsed Laser Ablation in Water and Their Characterization. *J. Phys. Chem. C* **2011,** *115* (12), 5073-5083.

163. Goncharova, D. A.; Kharlamova, T. S.; Lapin, I. N.; Svetlichnyi, V. A., Chemical and Morphological Evolution of Copper Nanoparticles Obtained by Pulsed Laser Ablation in Liquid. *J. Phys. Chem. C* **2019,** *123* (35), 21731-21742.

164. Amendola, V.; Meneghetti, M., What controls the composition and the structure of nanomaterials generated by laser ablation in liquid solution? *PCCP* **2013,** *15* (9), 3027-3046.

165. Zeng, H.; Du, X.-W.; Singh, S. C.; Kulinich, S. A.; Yang, S.; He, J.; Cai, W., Nanomaterials via Laser Ablation/Irradiation in Liquid: A Review. *Adv. Funct. Mater.* **2012,** *22* (7), 1333-1353.

166. Reich, S.; Schönfeld, P.; Wagener, P.; Letzel, A.; Ibrahimkutty, S.; Gökce, B.; Barcikowski, S.; Menzel, A.; dos Santos Rolo, T.; Plech, A., Pulsed laser ablation in liquids: Impact of the bubble dynamics on particle formation. *J. Colloid Interface Sci.* **2017,** *489*, 106-113.

167. Kang, K.-T.; Rho, Y.; Park, H. K.; Hwang, D. J., Investigation of Elemental Composition Change by Laser Ablation of a Rare-Earth Containing Material. *physica status solidi (a)* **2018,** *215* (20), 1700947.

168. Dizajghorbani Aghdam, H.; Azadi, H.; Esmaeilzadeh, M.; Moemen Bellah, S.; Malekfar, R., Ablation time and laser fluence impacts on the composition, morphology and optical properties of copper oxide nanoparticles. *Opt. Mater.* **2019,** *91*, 433-438.

169. Liu, P.; Cui, H.; Wang, C. X.; Yang, G. W., From nanocrystal synthesis to functional nanostructure fabrication: laser ablation in liquid. *PCCP* **2010,** *12* (16), 3942-3952.

170. Novoselov, K. S.; Geim, A. K.; Morozov, S. V.; Jiang, D.; Zhang, Y.; Dubonos, S. V.; Grigorieva, I. V.; Firsov, A. A., Electric Field Effect in Atomically Thin Carbon Films. *Science* **2004,** *306* (5696), 666-669.

171. Zhang, Y.; Zhang, L.; Zhou, C., Review of Chemical Vapor Deposition of Graphene and Related Applications. *Acc. Chem. Res.* **2013,** *46* (10), 2329-2339.

172. Justino, C. I. L.; Gomes, A. R.; Freitas, A. C.; Duarte, A. C.; Rocha-Santos, T. A. P., Graphene based sensors and biosensors. *TrAC, Trends Anal. Chem.* **2017,** *91*, 53-66.

173. Chung, C.; Kim, Y.-K.; Shin, D.; Ryoo, S.-R.; Hong, B. H.; Min, D.-H., Biomedical Applications of Graphene and Graphene Oxide. *Acc. Chem. Res.* **2013,** *46* (10), 2211-2224.

174. Inagaki, M.; Kang, F., Graphene derivatives: graphane, fluorographene, graphene oxide, graphyne and graphdiyne. *J. Mater. Chem. A* **2014,** *2* (33), 13193-13206.

175. Markovic, Z. M.; Ristic, B. Z.; Arsikin, K. M.; Klisic, D. G.; Harhaji-Trajkovic, L. M.; Todorovic-Markovic, B. M.; Kepic, D. P.; Kravic-Stevovic, T. K.; Jovanovic, S. P.; Milenkovic, M. M.; Milivojevic, D. D.; Bumbasirevic, V. Z.; Dramicanin, M. D.; Trajkovic, V. S., Graphene quantum dots as autophagy-inducing photodynamic agents. *Biomaterials* **2012,** *33* (29), 7084-7092.

176. Niu, K. Y.; Yang, J.; Kulinich, S. A.; Sun, J.; Li, H.; Du, X. W., Morphology Control of Nanostructures via Surface Reaction of Metal Nanodroplets. *JACS* **2010,** *132* (28), 9814-9819.

177. Yu, H.; Li, X.; Zeng, X.; Lu, Y., Preparation of carbon dots by non-focusing pulsed laser irradiation in toluene. *Chem. Commun.* **2016,** *52* (4), 819-822.

178. Gokhale, R. R.; Thakare, V. P.; Warule, S.; Lefez, B.; Hannoyer, B.; Jog, J. P.; Ogale, S. B., From small aromatic molecules to functional nanostructured carbon by pulsed laser-induced photochemical stitching. *AIP Adv.* **2012,** *2* (2), 022130.

179. Hu, S.; Liu, J.; Yang, J.; Wang, Y.; Cao, S., Laser synthesis and size tailor of carbon quantum dots. *J. Nanopart. Res.* **2011,** *13* (12), 7247-7252.

180. Russo, P.; Hu, A.; Compagnini, G.; Duley, W. W.; Zhou, N. Y., Femtosecond laser ablation of highly oriented pyrolytic graphite: a green route for large-scale production of porous graphene and graphene quantum dots. *Nanoscale* **2014,** *6* (4), 2381-2389.

181. Kang, S. H.; Mhin, S.; Han, H.; Kim, K. M.; Jones, J. L.; Ryu, J. H.; Kang, J. S.; Kim, S. H.; Shim, K. B., Ultrafast Method for Selective Design of Graphene Quantum Dots with Highly Efficient Blue Emission. *Sci. Rep.* **2016,** *6*, 38423.

182. Narasimhan, A. K.; Lakshmi B, S.; Santra, T. S.; Rao, M. S. R.; Krishnamurthi, G., Oxygenated graphene quantum dots (GQDs) synthesized using laser ablation for long-term real-time tracking and imaging. *RSC Advances* **2017,** *7* (85), 53822-53829.

183. Russo, P.; Liang, R.; Jabari, E.; Marzbanrad, E.; Toyserkani, E.; Zhou, Y. N., Single-step synthesis of graphene quantum dots by femtosecond laser ablation of graphene oxide dispersions. *Nanoscale* **2016,** *8* (16), 8863-8877.

184. Atienzar, P.; Primo, A.; Lavorato, C.; Molinari, R.; García, H., Preparation of Graphene Quantum Dots from Pyrolyzed Alginate. *Langmuir* **2013,** *29* (20), 6141-6146.

185. Castro, H. P. S.; Souza, V. S.; Scholten, J. D.; Dias, J. H.; Fernandes, J. A.; Rodembusch, F. S.; dos Reis, R.; Dupont, J.; Teixeira, S. R.; Correia, R. R. B., Synthesis and Characterisation of Fluorescent Carbon Nanodots Produced in Ionic Liquids by Laser Ablation. *Chem. Eur. J.* **2016,** *22* (1), 138-143.

186. Nguyen, V.; Yan, L.; Si, J.; Hou, X., Femtosecond laser-induced size reduction of carbon nanodots in solution: Effect of laser fluence, spot size, and irradiation time. *J. Appl. Phys.* **2015,** *117* (8), 084304.

187. Lehtonen, O.; Sundholm, D., Bright luminescence from silane substituted and bridged silicon nanoclusters. *PCCP* **2006,** *8* (36), 4228-4232.

188. Lai, S. K.; Luk, C. M.; Tang, L.; Teng, K. S.; Lau, S. P., Photoresponse of polyaniline-functionalized graphene quantum dots. *Nanoscale* **2015,** *7* (12), 5338-5343.

189. Gupta, B.; Kumar, N.; Panda, K.; Kanan, V.; Joshi, S.; Visoly-Fisher, I., Role of oxygen functional groups in reduced graphene oxide for lubrication. *Sci. Rep.* **2017,** *7*, 45030.

190. Pavia, D. L.; Lampman, G. M.; Kriz, G. S.; Vyvyan, J. R., *Introduction to spectroscopy*. 4th ed.; Brooks/Cole, Cengage Learning: Belmont, CA, 2009; p xv, 656, 48, 8, 15 p.

191. Zheng, H.; Wang, Q.; Long, Y.; Zhang, H.; Huang, X.; Zhu, R., Enhancing the luminescence of carbon dots with a reduction pathway. *Chem. Commun.* **2011,** *47* (38), 10650-10652.

192. Liu, Y. Photoluminescence Mechanism and Applications of Graphene Quantum Dots. Doctoral Thesis, University of Kentucky, 2017.

193. Feng, J.; Dong, H.; Yu, L.; Dong, L., The optical and electronic properties of graphene quantum dots with oxygen-containing groups: a density functional theory study. *J. Mater. Chem. C* **2017,** *5* (24), 5984-5993.

194. Qian, Z. S.; Shan, X. Y.; Chai, L. J.; Ma, J. J.; Chen, J. R.; Feng, H., A universal fluorescence sensing strategy based on biocompatible graphene quantum dots and graphene oxide for the detection of DNA. *Nanoscale* **2014,** *6* (11), 5671-5674.

195. Cui, B.; Feng, X.-t.; Zhang, F.; Wang, Y.-l.; Liu, X.-g.; Yang, Y.-z.; Jia, H.-s., The use of carbon quantum dots as fluorescent materials in white LEDs. *New Carbon Materials* **2017,** *32* (5), 385-401.

196. Jovanović, S. P.; Syrgiannis, Z.; Marković, Z. M.; Bonasera, A.; Kepić, D. P.; Budimir, M. D.; Milivojević, D. D.; Spasojević, V. D.; Dramićanin, M. D.; Pavlović, V. B.; Todorović Marković, B. M., Modification of Structural and Luminescence Properties of Graphene Quantum Dots by Gamma Irradiation and Their Application in a Photodynamic Therapy. *ACS Appl. Mater. Interfaces* **2015,** *7* (46), 25865-25874.

197. Zou, X.; Liu, M.; Wu, J.; Ajayan, P. M.; Li, J.; Liu, B.; Yakobson, B. I., How Nitrogen-Doped Graphene Quantum Dots Catalyze Electroreduction of CO2 to Hydrocarbons and Oxygenates. *ACS Catalysis* **2017,** *7* (9), 6245-6250.

198. Li, Q.; Zhang, S.; Dai, L.; Li, L.-s., Nitrogen-Doped Colloidal Graphene Quantum Dots and Their Size-Dependent Electrocatalytic Activity for the Oxygen Reduction Reaction. *JACS* **2012,** *134* (46), 18932-18935.

199. Zhu, S.; Shao, J.; Song, Y.; Zhao, X.; Du, J.; Wang, L.; Wang, H.; Zhang, K.; Zhang, J.; Yang, B., Investigating the surface state of graphene quantum dots. *Nanoscale* **2015,** *7* (17), 7927-7933.

200. Permatasari, F. A.; Aimon, A. H.; Iskandar, F.; Ogi, T.; Okuyama, K., Role of C–N Configurations in the Photoluminescence of Graphene Quantum Dots Synthesized by a Hydrothermal Route. *Sci. Rep.* **2016,** *6,* 21042.

201. Sarkar, S.; Sudolská, M.; Dubecký, M.; Reckmeier, C. J.; Rogach, A. L.; Zbořil, R.; Otyepka, M., Graphitic Nitrogen Doping in Carbon Dots Causes Red-Shifted Absorption. *J. Phys. Chem. C* **2016,** *120* (2), 1303-1308.

202. Wang, K.; Dong, J.; Sun, L.; Chen, H.; Wang, Y.; Wang, C.; Dong, L., Effects of elemental doping on the photoluminescence properties of graphene quantum dots. *RSC Advances* **2016,** *6* (94), 91225-91232.

203. Tetsuka, H.; Asahi, R.; Nagoya, A.; Okamoto, K.; Tajima, I.; Ohta, R.; Okamoto, A., Optically Tunable Amino-Functionalized Graphene Quantum Dots. **2012,** *24* (39), 5333-5338.

204. Qu, D.; Zheng, M.; Zhang, L.; Zhao, H.; Xie, Z.; Jing, X.; Haddad, R. E.; Fan, H.; Sun, Z., Formation mechanism and optimization of highly luminescent N-doped graphene quantum dots. *Sci. Rep.* **2014,** *4,* 5294.

205. Wang, W.; Wang, Z.; Liu, J.; Peng, Y.; Yu, X.; Wang, W.; Zhang, Z.; Sun, L., One-Pot Facile Synthesis of Graphene Quantum Dots from Rice Husks for Fe3+ Sensing. *Industrial & Engineering Chemistry Research* **2018,** *57* (28), 9144-9150.

206. Wang, G.; Guo, Q.; Chen, D.; Liu, Z.; Zheng, X.; Xu, A.; Yang, S.; Ding, G., Facile and Highly Effective Synthesis of Controllable Lattice Sulfur-Doped Graphene Quantum Dots via Hydrothermal Treatment of Durian. *ACS Appl. Mater. Interfaces* **2018,** *10* (6), 5750-5759.

207. Calabro, R. L.; Yang, D.-S.; Kim, D. Y., Liquid-phase laser ablation synthesis of graphene quantum dots from carbon nano-onions: Comparison with chemical oxidation. *J. Colloid Interface Sci.* **2018,** *527*, 132-140.

208. Zuo, P.; Lu, X.; Sun, Z.; Guo, Y.; He, H., A review on syntheses, properties, characterization and bioanalytical applications of fluorescent carbon dots. *Microchimica Acta* **2016,** *183* (2), 519-542.

209. Xu, H.; Yan, L.; Nguyen, V.; Yu, Y.; Xu, Y., One-step synthesis of nitrogen-doped carbon nanodots for ratiometric pH sensing by femtosecond laser ablation method. *Appl. Surf. Sci.* **2017,** *414*, 238-243.

210. Santiago, S. R. M.; Wong, Y. A.; Lin, T. N.; Chang, C. H.; Yuan, C. T.; Shen, J. L., Effect of nitrogen doping on the photoluminescence intensity of graphene quantum dots. *Opt. Lett.* **2017,** *42* (18), 3642-3645.

211. Gong, K.; Du, F.; Xia, Z.; Durstock, M.; Dai, L., Nitrogen-Doped Carbon Nanotube Arrays with High Electrocatalytic Activity for Oxygen Reduction. *Science* **2009,** *323* (5915), 760-764.

212. Yang, S.; Verdaguer-Casadevall, A.; Arnarson, L.; Silvioli, L.; Čolić, V.; Frydendal, R.; Rossmeisl, J.; Chorkendorff, I.; Stephens, I. E. L., Toward the Decentralized Electrochemical Production of H2O2: A Focus on the Catalysis. *ACS Catalysis* **2018,** *8* (5), 4064-4081.

213. Choi, C. H.; Kwon, H. C.; Yook, S.; Shin, H.; Kim, H.; Choi, M., Hydrogen Peroxide Synthesis via Enhanced Two-Electron Oxygen Reduction Pathway on Carbon-Coated Pt Surface. *J. Phys. Chem. C* **2014,** *118* (51), 30063-30070.

214. Kim, H. W.; Ross, M. B.; Kornienko, N.; Zhang, L.; Guo, J.; Yang, P.; McCloskey, B. D., Efficient hydrogen peroxide generation using reduced graphene oxide-based oxygen reduction electrocatalysts. *Nature Catalysis* **2018,** *1* (4), 282-290.

215. Lin, L.; Song, X.; Chen, Y.; Rong, M.; Zhao, T.; Jiang, Y.; Wang, Y.; Chen, X., One-pot synthesis of highly greenish-yellow fluorescent nitrogen-doped graphene quantum dots for pyrophosphate sensing via competitive coordination with Eu3+ ions. *Nanoscale* **2015,** *7* (37), 15427-15433.

216. Chua, C. K.; Sofer, Z.; Šimek, P.; Jankovský, O.; Klímová, K.; Bakardjieva, S.; Hrdličková Kučková, Š.; Pumera, M., Synthesis of Strongly Fluorescent Graphene Quantum Dots by Cage-Opening Buckminsterfullerene. *ACS Nano* **2015,** *9* (3), 2548-2555.

217. Chua, C. K.; Pumera, M., Selective Removal of Hydroxyl Groups from Graphene Oxide. *Chem. Eur. J.* **2013,** *19* (6), 2005-2011.

218. Tang, L.; Ji, R.; Li, X.; Teng, K. S.; Lau, S. P., Energy-level structure of nitrogen-doped graphene quantum dots. *J. Mater. Chem. C* **2013,** *1* (32), 4908-4915.

219. Thornburg, D. M.; Madix, R. J., Cleavage of NH bonds by active oxygen on Ag(110): II. Selective oxidation of ethylamine to acetonitrile. *Surf. Sci.* **1990,** *226* (1), 61-76.

220. Hu, S.; Tian, R.; Dong, Y.; Yang, J.; Liu, J.; Chang, Q., Modulation and effects of surface groups on photoluminescence and photocatalytic activity of carbon dots. *Nanoscale* **2013,** *5* (23), 11665-11671.

221. Niu, X.; Li, Y.; Shu, H.; Wang, J., Revealing the underlying absorption and emission mechanism of nitrogen doped graphene quantum dots. *Nanoscale* **2016,** *8* (46), 19376-19382.

222. Chaojie Song, J. Z., Electrocatalytic Oxygen Reduction Reaction. In *PEM Fuel Cell Electrocatalysts and Catalyst Layers*, Springer: London, 2008; pp 89-134.

223. Lv, Q.; Si, W.; He, J.; Sun, L.; Zhang, C.; Wang, N.; Yang, Z.; Li, X.; Wang, X.; Deng, W.; Long, Y.; Huang, C.; Li, Y., Selectively nitrogen-doped carbon materials as superior metal-free catalysts for oxygen reduction. *Nature Communications* **2018,** *9* (1), 3376.

224. Liu, Y.; Kim, D. Y., Enhancement of Capacitance by Electrochemical Oxidation of Nanodiamond Derived Carbon Nano-Onions. *Electrochim. Acta* **2014,** *139*, 82-87.

225. Britz, D., iR elimination in electrochemical cells. *Journal of Electroanalytical Chemistry and Interfacial Electrochemistry* **1978,** *88* (3), 309-352.

226. Souto, R. M., Electronic configurations in potentiostats for the correction of ohmic losses. **1994,** *6* (7), 531-542.

227. Hoang, S.; Guo, S.; Hahn, N. T.; Bard, A. J.; Mullins, C. B., Visible Light Driven Photoelectrochemical Water Oxidation on Nitrogen-Modified TiO2 Nanowires. *Nano Lett.* **2012,** *12* (1), 26-32.

228. Zhang, Y.; Kim, D. Y., Electrochemical Treatment of Glassy Carbon for Label-Free Detection of DNA Bases and Neurotransmitters. **2015,** *27* (11), 2581-2587.

229. Zhou, R.; Zheng, Y.; Jaroniec, M.; Qiao, S.-Z., Determination of the Electron Transfer Number for the Oxygen Reduction Reaction: From Theory to Experiment. *ACS Catalysis* **2016,** *6* (7), 4720-4728.

230. Kramida, A., Ralchenko, Yu., Reader, J., and NIST ASD Team, NIST Atomic Spectra Database. 2019 ed.; 2019; Vol. ver. 5.7.1.

231. Dong, C.; Liu, Z.; Wang, S.; Zheng, B.; Guo, W.; Yang, W.; Gong, X.; Wu, X.; Wang, H.; Chang, J., A Protein–Polymer Bioconjugate-Coated Upconversion Nanosystem for Simultaneous Tumor Cell Imaging, Photodynamic Therapy, and Chemotherapy. *ACS Appl. Mater. Interfaces* **2016,** *8* (48), 32688-32698.

232. Wawrzyńczyk, D.; Cichy, B.; Zaręba, J. K.; Bazylińska, U., On the interaction between up-converting NaYF4:Er3+,Yb3+ nanoparticles and Rose Bengal molecules constrained within the double core of multifunctional nanocarriers. *J. Mater. Chem. C* **2019,** *7* (47), 15021-15034.

233. Nunokawa, T.; Odawara, O.; Wada, H., Optical properties of highly crystalline Y2O3:Er,Yb nanoparticles prepared by laser ablation in water. *Materials Research Express* **2014,** *1* (3), 035043.

234. Grazulis, S.; Chateigner, D.; Downs, R. T.; Yokochi, A. F. T.; Quiros, M.; Lutterotti, L.; Manakova, E.; Butkus, J.; Moeck, P.; Le Bail, A., Crystallography Open Database - an open-access collection of crystal structures. *J. Appl. Crystallogr.* **2009,** *42* (4), 726-729.

235. Gražulis, S.; Daškevič, A.; Merkys, A.; Chateigner, D.; Lutterotti, L.; Quirós, M.; Serebryanaya, N. R.; Moeck, P.; Downs, R. T.; Le Bail, A., Crystallography Open Database (COD): an open-access collection of crystal structures and platform for world-wide collaboration. *Nucleic Acids Res.* **2011,** *40* (D1), D420-D427.

236. Thoma, R. E.; Insley, H.; Hebert, G. M., The Sodium Fluoride-Lanthanide Trifluoride Systems. *Inorg. Chem.* **1966,** *5* (7), 1222-1229.

237. Rumble, J. R., ed., *CRC Handbook of Chemistry and Physics*. 100th (Internet Version 2019) ed.; CRC Press/Taylor & Francis: Boca Raton, FL.

238. Zhang, Y.; Evans, J. R. G.; Yang, S., Corrected Values for Boiling Points and Enthalpies of Vaporization of Elements in Handbooks. *J. Chem. Eng. Data* **2011,** *56* (2), 328-337.

239. Fei, H.; Ye, R.; Ye, G.; Gong, Y.; Peng, Z.; Fan, X.; Samuel, E. L. G.; Ajayan, P. M.; Tour, J. M., Boron- and Nitrogen-Doped Graphene Quantum Dots/Graphene Hybrid Nanoplatelets as Efficient Electrocatalysts for Oxygen Reduction. *ACS Nano* **2014,** *8* (10), 10837-10843.

240. Rub Pakkath, S. A.; Chetty, S. S.; Selvarasu, P.; Vadivel Murugan, A.; Kumar, Y.; Periyasamy, L.; Santhakumar, M.; Sadras, S. R.; Santhakumar, K., Transition Metal Ion (Mn2+, Fe2+, Co2+, and Ni2+)-Doped Carbon Dots Synthesized via Microwave-Assisted Pyrolysis: A Potential Nanoprobe for Magneto-fluorescent Dual-Modality Bioimaging. *ACS Biomaterials Science & Engineering* **2018,** *4* (7), 2582-2596.

241. Kumar, V. B.; Kumar, R.; Gedanken, A.; Shefi, O., Fluorescent metal-doped carbon dots for neuronal manipulations. *Ultrason. Sonochem.* **2019,** *52*, 205-213.

242. Gao, J.; Zhu, M.; Huang, H.; Liu, Y.; Kang, Z., Advances, challenges and promises of carbon dots. *Inorganic Chemistry Frontiers* **2017,** *4* (12), 1963-1986.

243. He, L.; Yang, L.; Zhu, H.; Dong, W.; Ding, Y.; Zhu, J.-J., A highly sensitive biosensing platform based on upconversion nanoparticles and graphene quantum dots for the detection of Ag+. *Methods and Applications in Fluorescence* **2017,** *5* (2), 024010.

VITA

Education:

Bachelor of Science, Chemistry | Indiana University | Bloomington, IN
Research Advisor: Dr. Lyudmila Bronstein
August 2010-May 2014

Doctor of Philosophy, Chemistry | University of Kentucky |Lexington, KY
Research Advisors: Dr. Doo Young Kim and Dr. Dong-Sheng Yang
August 2014-Present

Awards:

- Research Challenge Trust Fund (2016, 2017, 2018, 2019)
- University of Kentucky College of Arts and Sciences Certificate for Outstanding Teaching (2018)
- Kentucky Academy of Science Research Competition, Chemistry: Analytical/Physical, Oral Presentation-Graduate, 1st Place (2017)
- Departmental Honors in Chemistry for Graduate Student Recruitment (2017)
- 100% Plus Award, University of Kentucky Chemistry Departmental Award (2016)
- Wimberly C Royster Graduate Excellence Award (2014, 2015, 2016)
- Southern Indiana Local Section ACS Undergraduate Travel Award (2013)
- Harry G Day Summer Research Scholarship (2013)
- IU Excellence Scholarship (2010)

Publications:

1. **Calabro, R. L.** ; Yang, D. -Y.; Kim, D. Y. "*Controlled Nitrogen Doping of Graphene Quantum Dots through Laser Ablation in Aqueous Solutions for Photoluminescence and Electrocatalytic Applications*" ACS Appl. Nano Mater. (2019), 2, 11, 6948-6959.

2. Uddin, M. A.; Mobley, J.; Masud, A.; Tiu, T.; **Calabro, R.**; Kim, D. Y.; Richards, C.; Graham, K. "*Mechanistic Exploration of Dodecanethiol Treated Colloidal CsPbBr3 Nanocrystals with Photoluminescence Quantum Yields Reaching Near 100%*". J. Phys. Chem. C, (2019), 123, 29, 18103-18112.

3. Uddin, M. A.; **Calabro, R. L.**; Kim, D. -Y.; Graham, K. R. "*Halide exchange and surface modification of metal halide perovskite nanocrystals with alkyltrichlorosilanes.*" Nanoscale (2018), *10, (35),* 16919-16927.

4. **Calabro, R.**; Yang, D. -Y.; Kim, D. Y. "*Liquid-phase laser ablation synthesis of graphene quantum dots from carbon nano-onions: Comparison with chemical oxidation.*" J. Colloid Interface Sci. (2018), 527, 132-140.

5. **Easterday, R.**; Sanchez-Felix, O.; Losovyj, Y.; Pink, M.; Stein, B.D.; Morgan, D.G.; Rakitin, M.; Doluda, V. Y.; Sulman, M.; Mahmoud, W. E.; Al-Ghamdi, A. A.; Bronstein, L.M. "*Design of Ruthenium/Iron Oxide Nanoparticle Mixtures for Hydrogenation of Nitrobenzene to Aniline: Catalytic Behaviour Influenced by Iron Oxide Nanoparticles.*" Catal. Sci. Technol. (2015), 5, *1902*-1910.

6. Malyutin, A. G.; **Easterday, R.**; Lozovyy, Y.; Spilotros, A.; Cheng, H.; Sanchez-Felix, O. R.; Stein, B. D.; Morgan, D. G.; Svergun, D. I.; Dragnea, B.; Bronstein, L.M. "*Viruslike Nanoparticles with Maghemite Cores Allow for Enhanced MRI Contrast Agents.*" Chem. Mater. (2015), 27(1), 327-335.

7. **Easterday, R.**; Leonard, C.; Sanchez-Felix, O.; Losovyj, Y. B.; Pink, M.; Stein, B. D.; Morgan, D. G.; Lyubimova, N. A.; Nikoshvili, L. Zh.; Sulman, E. M.; Mahmoud, W. E.; Al-Ghamdi, A. A.; Bronstein, L. M. "*Fabrication of Magnetically Recoverable Catalysts Based on Mixtures of Pd and Iron Oxide Nanoparticles for Hydrogenation of Alkyne Alcohols.*" ACS Appl. Mater. & Interfaces (2014), 6(23), 21652-21660.

8. **Easterday, R.**; Sanchez-Felix, O.; Stein, B. D.; Morgan, D. G.; Pink, M.; Losovyj, Y.; Bronstein, L. M. "*Structural Study of Pt-Fe Nanoparticles: New Insights into Pt Bimetallic Nanoparticle Formation with Oxidized Fe Species.*" J. Phys. Chem. C (2014), 118(42), 24769-24775.

9. Gumina, G.; **Easterday, R.**; Malyutin, A.G.; Budgin, A.M.; Stein, B.D.; Nikoshvili, L. Zh.; Matveeva, V.G.; Sulman, E.M.; Morgan, D.G.; Bronstein, L.M. "*gamma-Fe2O3 Nanoparticle Surface Controls PtFe Nanoparticle Growth and Catalytic Properties*". Nanoscale (2013), 5, 2921-2927.